DAMAGE EVOLUTION IN UNIAXIAL SiC FIBER REINFORCED Ti MATRIX COMPOSITES

Thesis by

Jay Clarke Hanan

In Partial Fulfillment of the Requirements

for the Degree of

Doctor of Philosophy

California Institute of Technology

Pasadena, California

2002

(Defended June 18, 2002)

Acknowledgments

Several people have been helpful in bringing me to this point. The top of my list is clearly occupied by Robin. She is much more than my wife exemplifying the noble character many others never achieve. Of course, when considering family, I must be grateful to my parents Russ and Jan who continually encouraged creativity.

It was my undergraduate physics professor and academic advisor, Dr. Lynn Feuerhelm, who encouraged me to consider graduate school. I would not be here without him or the fateful meeting of John Rousseau who like so many other members of the Caltech community represented it favorably to a receptive undergrad looking for the right opportunity.

Dr. Ersan Üstündag has been extremely helpful as my academic and research advisor. He took a chance with me as I did with him, being his first student. Even though we have not agreed on everything, we would agree the chance was worth it. He always considered my opinion and was so instrumental in getting us to this point, which when I started down this path five years ago seemed far away. Looking back through this now seemingly short time, we have both grown first in science and never least in friendship. It was Dr. Üstündag's contacts, including

> Bjørn Clausen of LANSCE at Los Alamos National Lab who was extremely helpful with the FEM work; irreplaceable Dr. I. Cev Noyan of the IBM Watson Research Center who was such an inspiration contributing valuable advice and resources (including his load frame); Jon Almer and Ulrich Linert of the APS who helped facilitate the majority of

the relevant data collection and analysis; and Irene Beyerlein, also from Los Alamos, providing support with the micromechanical modeling, which helped make up the army of people necessary to complete this work. There were also several graduate students who were helpful during the experiments where we not only tested materials, but ourselves (especially after sleep deprivation), namely: Geoff Swift, Stefen Kaldor, and Can Aydiner. I also have to thank Kevin Foltz who along with my sister Rae and daughter Raevan unknowingly challenged me to finish sooner rather than later.

I am also grateful to Dr. H. Deve at 3M Corp. for providing the specimens and helpful discussions about the properties of Ti-SiC composites. This study was supported by the National Science Foundation (CAREER grant no. DMR-9985264) at Caltech and a Laboratory-Directed Research and Development Project (no. 2000043) at Los Alamos. The work at the Advanced Photon Source was supported by the U.S. Department of Energy, Office of Basic Energy Sciences (contract no. W-31-109-ENG-38).

Abstract

Damage Evolution in Uniaxial SiC Fiber Reinforced Ti Matrix Composites

by Jay Clarke Hanan

Fiber fractures initiate damage zones ultimately determining the strength and lifetime of metal matrix composites (MMCs). The evolution of damage in a MMC comprising a row of unidirectional SiC fibers (32 vol.%) surrounded by a Ti matrix was examined using X-ray microdiffraction (μm beam size) and macrodiffraction (mm beam size). A comparison of high-energy X-ray diffraction (XRD) techniques including a powerful two-dimensional XRD method capable of obtaining powder averaged strains from a small number of grains is presented (HEμXRD^2).

Using macrodiffraction, the bulk residual strain in the composite was determined against a true strain-free reference. In addition, the bulk *in situ* response of both the fiber reinforcement and the matrix to tensile stress was observed and compared to a three-dimensional finite element model. Using microdiffraction, multiple strain maps including both phases were collected *in situ* before, during, and after the application of tensile stress, providing an unprecedented detailed picture of the micromechanical behavior in the laminate metal matrix composite.

Finally, the elastic axial strains were compared to predictions from a modified shear lag model, which unlike other shear lag models, considers the elastic response of both constituents. The strains showed excellent correlation with the model. The results confirmed, for the first time, both the need and validity of this new model specifically

developed for large scale multifracture and damage evolution simulations of metal matrix composites. The results also provided unprecedented insight for the model, revealing the necessity of incorporating such factors as plasticity of the matrix, residual stress in the composite, and selection of the load sharing parameter.

The irradiation of a small number of grains provided strain measurements comparable to a continuum mechanical state in the material. Along the fiber axes, thermal residual stresses of 740 MPa (fibers) and +350 MPa (matrix) were found. Local yielding was observed by 500 MPa in the bulk matrix of the composite. Plastic anisotropy was observed in the matrix. The intergranular strains in the Ti matrix varied as much as 50%. In spite of this variation, the HEμXRD^2 technique powerfully provided reliable information from the matrix as well as the fibers.

Table of Contents

List of Illustrations and Tables

Figures

Number *Page*

Tables

1. Introduction

1-1. *Background and Motivation*

Metal matrix composites (MMCs) were introduced as structural materials in the early 1970s. Nearly a decade later, with improvements in processing, applications in aeronautics and the automotive industry began demanding materials with the specific strength and modulus, controlled toughness and thermal expansion coefficient, hardness, and an improved fatigue response only available from MMCs. Better understanding of their mechanical behavior fueled improvement of the reinforcements which in turn improved the composite properties. Consequently, MMCs have found a number of applications which now vary from sporting goods to thermal and wear-resistant parts [1, 2].

Of the various types of MMCs (short fiber, particle, or continuous fiber reinforced), the continuous fiber reinforced variety provides the highest structural performance. These MMCs, usually reinforced with high modulus ceramic fibers, rely on the continuous fibers for their strength using the matrix primarily for protection and support of the fibers (see, for example, Figure 1-1). The matrix is also the key player for local stress transfer between fibers. The other types of MMCs typically depend on the weaker matrix to act also as a primary load bearing agent.

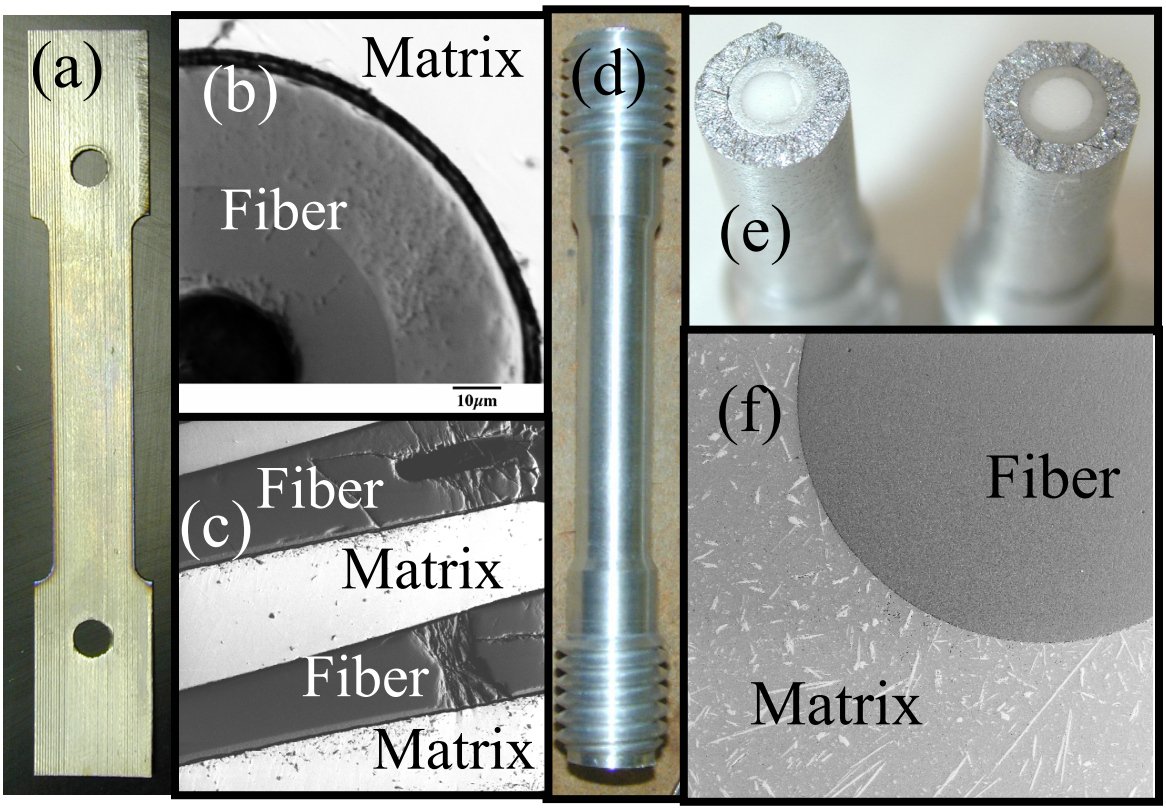

Figure 1-1 Some example views of continuous fiber metal matrix composites.

(a) Photograph of a two-dimensional continuous fiber metal matrix laminate composite tensile test specimen (Ti matrix/SiC fibers).

(b) Scanning electron micrograph (SEM) of the polished end of the same composite.

(c) Side view of a polished face of the laminar composite similar to that found in (a) here also using SEM.

(d) Photograph of a single fiber metal matrix composite (Al matrix/Al_2O_3 fiber).

(e) Fracture surface of a similar composite to (d) exposing the fiber.

(f) An SEM of the polished end of (d).

The transfer of load from a broken fiber to the rest of a composite as it is deformed is one of the fundamental micromechanical processes determining composite strength, lifetime and fracture toughness. It is a complex process that depends on fiber/matrix interface properties, the constitutive behavior of matrix and fibers, the geometric arrangement of fibers, fiber volume fraction, and fiber strength distribution. The

prediction of this process is further complicated since the *in situ* mechanical properties of the constituents are significantly different than the properties in the monolithic form [3, 4, 5]. These differences stem from (i) constraints imposed by neighboring phases; (ii) changes in microstructure due to altered processing conditions required for composite manufacturing; (iii) thermal residual stresses due to coefficient of thermal expansion (CTE) mismatch between different phases; and in some cases, (iv) high dislocation densities near the fiber/matrix interface [6].

Conventional stress analysis of fiber composites employs the use of strain gage rosettes on the surface of the matrix. Test methods such as the ASTM specification D3039-76 (1989) provide a detailed example of the traditional analysis which provides information on the longitudinal and transverse tensile strength, Young's moduli, tensile strain, and major (longitudinal) and minor (transverse) Poisson's ratios [7]. However, the macroscopic stress-strain curves obtained by these conventional means result from the co-deformation of the individual phases making it impossible to determine the phase-specific *in situ* constitutive behavior. Typical composite deformation includes collective nucleation and evolution of damage, fiber fractures, matrix fractures and plasticity, as well as interface separation and sliding.

Several mechanical models have been proposed to describe the behavior of MMCs. The simpler models such as the concentric cylinder or the Eshelby model point to the fiber fraction as the more sensitive parameter determining a composites properties. Bulk properties have also been predicted with relative success using finite element modeling (FEM). Several efforts to improve computational speed over FEM have been proposed. One of these, which uses the "shear lag" concept, will be examined in more detail in

Section 3-2. Reliable micromechanical models, particularly models that correctly predict ductility in MMCs, require further development [8].

Whatever model is employed to understand an MMC, there still remains an overwhelming need to validate or refute the predictions with relevant mechanical data. Such data are in short supply. Modeling studies are often compared to predictions from Monte Carlo simulations [9, 10] or incomplete subsets of data [8 (p. 241)], limiting the ultimate relevance to the engineer who must deal with the real composite. In the Ti-SiC composite system, micromechanical studies applying acoustic methods have been used to identify *in situ* fiber breaks. But these studies do not provide the phase-specific strains in the matrix and fibers, and only hint to the mechanism of load transfer in the composite [11].

In order to predict the strength and lifetime of a fiber composite, the load transfer from broken fibers to the surrounding intact material must be understood. This requires accurate determination of stress-strain evolution at the scale of microstructure—usually on the order of the fiber diameter. *In situ* measurements of stress/strain can then be used to validate and refine predictive micromechanics models. In special cases, this has been achieved using optical methods such as micro-Raman and piezospectroscopy [for example: 6, 12, 13, 14, 15]. These studies provided valuable insight about fiber strains in damaged composites at length scales approaching several μm. However, in most of these studies either the matrix could not be characterized, or only shallow surface regions were investigated.

More general probes that measure both the matrix strain and the reinforcement strain are necessary to truly understand composite deformation. One such tool historically

useful in measuring stress is X-ray diffraction. Low-energy X-ray diffraction, on the order of 8 keV,* has long been used to measure stress in single phase materials and, through several technological improvements, has become a standard method for measurements of residual stress in many materials [16, 17]. However, for most materials, low-energy X-ray diffraction provides information specific to the material surface. This is particularly true for MMCs where, beyond aluminum, the penetration depth of low-energy X-rays is on the order of micrometers (e.g., 30 μm for Ti at 9 keV) and rarely provides information on more than one layer of matrix grains. Destructive methods such as layer removal employed low energy X-rays for depth-resolved residual strain measurements [18, 19], but with the exception of diffraction via neutrons, observation of continuous fiber strains under applied stress was relegated to the abovementioned specialized cases where the matrix was optically transparent.

Neutron diffraction also remains a valuable tool in the investigation of MMC mechanical behavior. In-depth studies of the bulk composite response to applied stress coupled with phase-specific fiber and matrix strains have provided significant insight to the peculiar behavior of these materials [20, 21, 22, 23, 24, 25, 26, 27, 28]. Though one of these studies [28] does provide single fiber specific strains coupled with the elastic portion of the matrix response, the inherent advantage of the neutron's penetrating depth through week nuclear interactions also limits the probe's spatial resolution. In [28] the researchers compensate for this drawback by increasing the fiber diameter substantially beyond the realm of a typical MMC. The result is a measurement which is applicable to continuum mechanics models, but entirely avoids the role of fiber matrix interactions on

*Such as X rays available from a typical Cu tube.

the order of the microscale [29, 30]. Other more recent investigations have shown that, for a more traditional MMC even of the same material system, the fiber matrix interface is characterized primarily by abrupt variations in stress never considered by continuum mechanical models [31, 32]. Thus a general lack of information concerning MMC deformation mechanisms at the scale of the microstructure persists.

1-2. *Approach*

It naturally follows that a study on a practical high-performance MMC would be of significant value to the modeling and eventually engineering community. One such composite is the Ti-matrix/SiC-fiber laminate composite (Figure 1-1 (a)-(c)). Both Ti and SiC are well known as high-temperature structural materials [33]. Naturally, the Ti-SiC composite itself has received considerable attention from other researchers simply due to the performance characteristics of its constituents [8, 11, 19, 21, 23, 24, 25, 26]. However the fundamental lack of phase-specific micromechanical data remains.

The following describes the use of X-ray diffraction to determine the phase-specific *in situ* load transfer and damage evolution under applied tensile stress in a Ti-SiC composite. Synchrotron X rays were required to obtain the necessary intensity to reduce the beam size below the fiber diameter while maintaining sufficient diffraction statistics and strain resolution over reasonable count times. The technique described may be tailored to glean the specific mechanical information needed and is applicable to a variety of composites beyond the Ti-SiC system. Multiple scales from the micro (several μm) to macro (several mm) are simultaneously available with this method. No other technique, including neutron diffraction, could provide the spatially resolved strain resolution from

multiple phases so crucial to understanding mechanical behavior of metal matrix composites.

In this thesis, the Ti matrix and SiC fiber strains were compared to predictions from a general micromechanics model [34]. This "matrix stiffness shear lag" (MSSL) model accounts for the linear elastic co-deformation of fiber and matrix in a wide variety of unidirectional fiber composites containing any configuration of multiple fractures. This is the first damage evolution study tailored for application to a micromechanics model conducted on a continuous fiber MMC where both matrix and fibers were investigated simultaneously at the scale of the microstructure.

2. Diffraction Techniques to Study Composites

The following briefly introduces the use of X-ray diffraction to measure strain. Some issues concerning the application of stress to a diffracting body are also presented. The final section outlines the two primary analysis methods used to measure the strains in the Ti-SiC composite. The specifics of each experimental procedure are presented within the respective chapters regarding the experiments.

2-1. *Strain and X-Ray Diffraction*

Strain measurement with "traditional" X-ray diffraction (XRD) is a well-established technique [16, 17]. Measurements of strain using X rays were performed as early as 1925 [35]. Recent advances include the use of high-energy X rays (with more penetrating power) and microdiffraction with sampling volumes of several μm^3. Both of these are best performed at synchrotron facilities, and a combination of which was used for this study.

Microdiffraction experiments such as [36] by Noyan and co-workers at the National Synchrotron Light Source (NSLS) achieved a spatial resolution of a few μm. Their systematic investigations of the instrument improved its accuracy and identified potential sources of error such as beam divergence and the sphere of confusion [37, 38]. They provided a portion of the substantial groundwork establishing microdiffraction as a viable XRD method.

The use of high-energy X rays to sample regions deep in materials has been demonstrated by a number of pioneering studies [examples: 39, 40, 41, 42, 43]. High-energy synchrotron XRD provides the ability to probe buried regions in materials. The

high intensity of synchrotron X rays also provides excellent time and spatial resolution. The abovementioned synchrotron XRD studies employed both monochromatic [39, 41, 42], and polychromatic [40] beams with the former yielding higher strain sensitivity (10^{-5} vs. 10^{-3}). They also sampled volumes as small as several hundred μm^3. Although a few studies are noted on strain distributions around fibers in composites [39, 40, 41], none are known that investigated the *in situ* mechanical behavior of phases on multiple scales.

In general, direct XRD strain measurements under kinematic diffraction conditions are limited to crystalline phases of materials which deform elastically.* Polycrystalline bodies deform when subjected to external or internal stress. As long as the stress is small, the deformation is reversible. This reversible deformation is elastic strain. The X-ray strain method requires a measurement of the lattice parameters, using a least-squares refinement of several peaks, or lattice spacings, specific to a single peak position, in the material.

According to Bragg's Law, $\lambda = 2\,d \sin\theta$, diffraction peaks arise at a particular Bragg angle, θ, determined by the lattice spacing, d, of the atoms of a lattice in a grain (or crystallite) which is oriented for the diffraction condition at a particular wavelength, λ. Peak shifts determined as a difference in initial and final angles $\Delta(2\theta)$ are proportional to changes in the average distance between lattice planes, Δd [16]. It is this change in lattice spacing which provides the diffraction elastic lattice strain in a diffracting material:

$$\varepsilon = \frac{d - d_0}{d_0} \tag{2-1}$$

* It is possible to deduce plastic strain information using diffraction in a crystalline body or elastic strain information from an amorphous body (as a second phase), but here these are considered indirect strain measurements.

where d_0 is the reference lattice spacing. When d_0 is from a stress-free material, the resulting strain measured includes residual strain. Measuring residual strain using diffraction is well developed [17]. The choice of a strain-free reference and measurements of d_0 will be presented in Section 5-2.

Although the procedure is simple to describe and understand, its appropriate application requires extreme care, especially when considering the level of accuracy required to measure strains.* Errors can be intrinsic to the technique (and the instrument used) or they can result from the inhomogeneous nature of materials studied. In the general case when stress is applied to a polycrystalline material or composite, the total strain measured with diffraction at any point includes three terms [44]:

$$\varepsilon_{ij}^{total} = \varepsilon_{ij}^{o} + \varepsilon_{ij}^{inter.} + \varepsilon_{ij}^{res.} \tag{2-2}$$

where, ε_{ij}^{o} is the homogeneous elastic strain due to applied stress σ^{o} (if the material were a homogeneous isotropic body), $\varepsilon_{ij}^{inter.}$ is the interaction (or coupling) strain due to elastic incompatibility or inhomogeneous plastic yielding, and $\varepsilon_{ij}^{res.}$ is residual strain. Each of these terms is an average value over the sampling volume. Since not all the grains within that volume contribute to the diffraction pattern, effects from heterogeneity can become critical when sampling small volumes.

The measurement of a peak position to assign lattice spacing possesses an inherent error associated with fitting the peak. Depending on the source of the radiation and the conditions of the optics and specimen sampled, the peak width and profile will change. While sensitive to lattice spacing, the peak position is also sensitive to the optical and sample geometric configuration. Each component possesses its own contribution to the

*Many materials yield or fracture before the elastic strain reaches 1% (typically 0.2% to 0.5%).

error in the final peak position. A good review of errors in strain measurements is presented in [17]. In summary, the best practice to minimize error in a diffraction experiment is to maximize the exposure time, minimize inadvertent sample translation from the center of diffraction, and use an internal standard. An internal standard may be composed of any suitable diffracting material not expected to change its lattice spacing over the course of the experiment. If systematic errors from sample displacement or other minor misalignments occur, a strain-free standard will show a peak shift which may then be used to correct for erroneous shifts in the strained sample [45]. Internal standards also allow samples scanned between alignments to be compared, a necessary option for reliable residual strain measurements.

Selection of an internal standard can be difficult. Consideration must be made for overlap in the peaks from the standard with the peaks from the specimen. There may also be problems with exposure times, as the peak intensity from a strain-free standard is usually much greater than a strained material due to texture, grain size effects, or strain broadening. The best standards are available from the National Institute of Standards and Technology (NIST); however, a well-characterized powder which provides peaks that do not appreciably overlap will generally suffice. Several common standard powders include: Al_2O_3, CeO_2, LaB_6, NaCl, and Si.

2-1.1. Strain Measurements with *In Situ* Mechanical Loading

With X-ray diffraction's ability to measure strain, it follows to apply the analysis to a body under applied stress. Mechanical loading is not new to XRD. However, in spite of the considerable number of mechanical loading experiments performed using diffraction to measure strain, advances in optics and peripheral equipment have maintained a realm of continuous flux and renewal on the cutting edge of modern science. One significant new instrument planned for the Advanced Photon Source (APS) at Argonne National Lab, HEX-CAT (High Energy X-ray Collaborative Access Team) will dedicate much of its time to strain measurements using high energy X-ray diffraction. New instruments are also planned at other advanced facilities relying on neutron and X-ray diffraction (JEEP at Diamond/ISIS, ENGIN X at ISIS, VULCAN at SNS, SMARTS at LANSCE, a parallel optics μbeam line upgrade at X-20 (NSLS), and a 3-D spatially resolved sub-μm polychromatic beam line replacing 7.3.3 at ALS, to name a few).

The first mechanical loading experiments on unidirectional MMC composites performed by Caltech researchers using diffraction took advantage of the custom load frame based on an Instron hydraulic press at the Los Alamos Neutron Science Center. Further experiments using a small custom load frame designed by I. C. Noyan (IBM) were performed using synchrotron XRD at APS. Modifications to the Noyan load frame and adaptation of an Scanning Electron Microscope (SEM) load frame designed by Fullam,[*] have continued to improve the capability to mechanically load composites at Caltech while performing XRD measurements (see Figure 2-1, see also Figure 4-3, Figure 4-5, and Figure 5-14).

---

[*]Ernest Fullam Inc., 900 Albany Shaker Rd., Latham, NY 12110-1491.

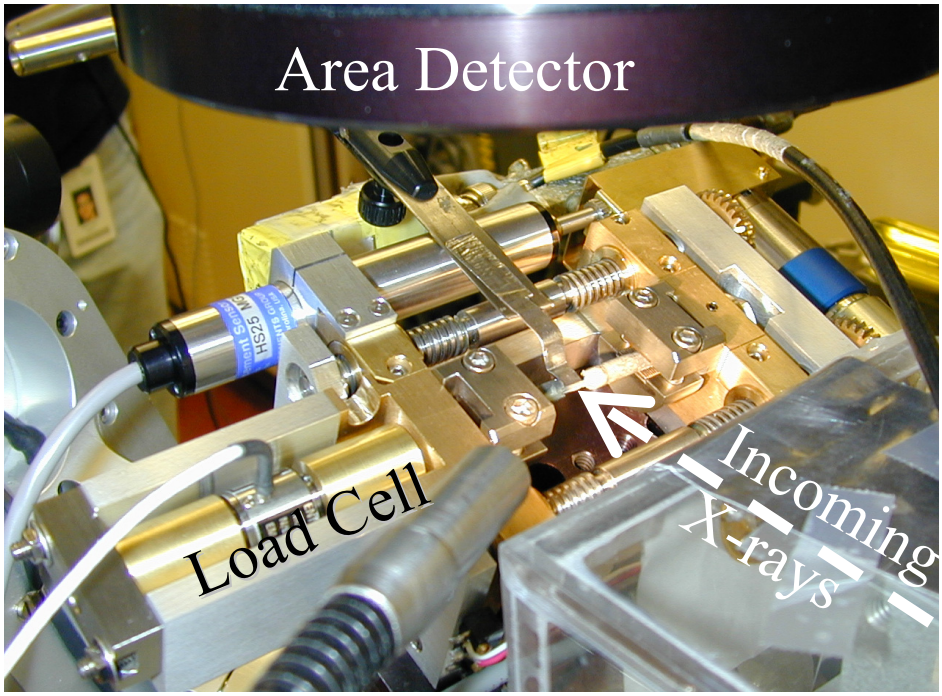

Figure 2-1 Photograph of adapted Fullam load frame on the goniometer at the 7.3.3 microdiffraction beam line at the Advanced Light Source. In this orientation, the open face of the load frame allows X rays to reflect from the surface of the sample.

As with any mechanical loading experiment, many factors including accurate load cells, a stiff frame, and stable strain increments are important in providing a good experimental tool. However, a load frame intended for use with diffraction also requires an open or transparent beam path exposing the sample to as wide a range of visibility as possible. Shadowing the beam by the load frame or grips limits the length of potential specimens, and since the diffracted beam averages strain over the irradiated area of the sample, edge effects and non-uniformities in the grip region should also be avoided. The weight of a load frame is often critical since, in general, it should be free to rotate when mounted on a traditional goniometer. For some special cases, very large goniometers or other robotic platforms are available to translate a massive load frame in the beam [28]. Finally, a constant stress mode as opposed to a constant strain or displacement

operational mode is preferred since diffraction measurements are associated with an exposure time sometimes approaching many hours.

When a constant load cannot be maintained, it is necessary to track the load over time and assign the appropriate load to each scan. Here "scan" refers to the measurement of one or more peak positions from a diffraction experiment as described below. In order to track the load on a sample mounted in an X-ray goniometer, a program was designed in LabVIEW* 6i (see Appendix A). The load cell used was an Entran† ELHS-T1M-1KL which requires a 10 to 15 V excitation to measure forces up to 6500 N. The output voltage from the load cell is proportional to the applied load on the sample.

Using digitization hardware, the output voltage can be read by a computer using the LabVIEW program. The time corresponding to the load cell reading by the computer is correlated with the start and end time of the scan. For a typical constant displacement experiment on metal matrix composites, the load does not change more than 0.1 MPa during short scans. However over the course of several scans the change can become significant enough to effect the strain measurements. Without appropriate accounting for this change in applied stress, strain results would be misinterpreted. A secondary link, assuring the scan times and load cell logged times are synchronized is also recommended. When a scan starts, a digital pulse may be sent to the LabVIEW computer and logged on the data file with the applied stress values. The pulse is particularly useful for tracking the load during manual scans which may not be recorded at regular time intervals.

---

*The LabVIEW software is commercially available from National Instruments, 11500 N Mopac Expwy, Austin, TX 78759-3504.

†Entran Devices, Inc. 10 Washington Ave., Fairfield, NJ 07004-3877.

In summary, even over the last three years, significant improvements to mechanical loading methods coupled with diffraction strain measurements have occurred [29, 30, 31, 32]. The driving force for such improvements is difficult to define. One important factor is the investment in advanced diffraction facilities. SMARTS is a good example of recent improvements which were particularly clear as it stood next to a previous generation workhorse for neutron diffraction strain measurements, NPD [28].* Similar advances such as the high-energy beam line at APS, have reduced the constraints on the application of mechanical load frames. Such synergistic combinations allow for high resolution X-ray strain measurements. A methodology for these experiments is presented in the following section.

*The Neutron Powder Diffractometer (NPD) was, as its name implies, originally dedicated to structure determination through powder diffraction. However it also, like many of its sisters, became a tool of the materials scientist.

2-2. *High-Resolution X-Ray Strain Measurements.*

High-resolution X-ray strain measurements require precise knowledge of the relative diffracted beam position (Figure 2-2). The *relative* as apposed to the *absolute* diffracted beam position is of interest since strain is calculated from a difference in lattice spacings, Eq. (2-1), which would be accurate even if the absolute lattice spacings are precise but inaccurate. For X-ray strain measurements, the overall objective is to obtain a high 2θ spatial resolution over the range of interest. Receiving slits are a very common tool used to improve the 2θ resolution of a diffraction measurement (Figure 2-2). Very narrow slits potentially increase resolution but significantly reduce the signal intensity.

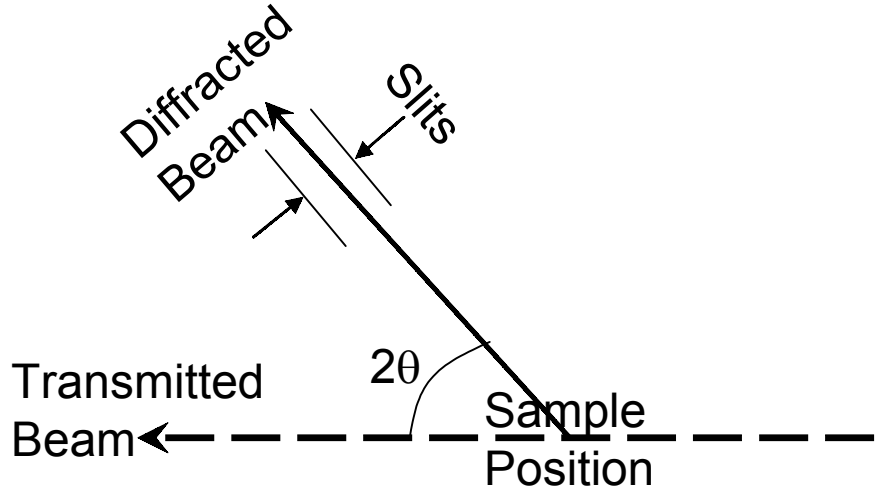

Figure 2-2 Schematic of the diffracted beam position and the position of receiving slits.

For most X-ray diffraction systems, assuming total mechanical freedom to reduce the slit size, consideration for the available time to measure the intensity at a particular 2θ typically fixes the lower limit of the slit width. For example, using a common Cu tube X-ray source on a standard Siemens diffractometer, reducing the receiving slits to 0.3^{o} from

3.0^{o} will extend an hour long scan into an overnight scan with similar peak intensity. However, with the large number of photons (or flux) available from a synchrotron X-ray source, difficulties in manufacturing reliable narrow slits can also provide a lower physical limit. Methods to reduce the receiving slit aperture have many forms. Slits range from stacked plates, called Soller slits, to reduce divergence to pinhole slits with very small apertures or with large aspect ratios maximizing the 2θ resolution at the expense of divergence in the direction perpendicular to θ for a gain in throughput. These slits may also be stacked to reduce divergence. A maximum angle of divergence can be readily realized with simple geometry: for two slits a distance, S, apart, and aperture A; the angle of maximum divergence, β, from a point source is $2\ A\ /\ S$. Since divergence broadens the peak in 2θ, the strain resolution will diminish with divergent beam optics.

However, particularly with synchrotron X radiation, the source may produce a highly parallel beam. For highly parallel optics, it is difficult and often unnecessary to mechanically construct slits which provide a significant reduction in divergence. In addition, parallel beam optics reduces the sensitivity to systematic errors. For parallel optics, the most effective "slit-like" tool to improve the 2θ spatial resolution is an analyzer crystal. Analyzer crystals consist of a single crystal which has rectangular trough or channel cut parallel to a diffracting plane through the length of the crystal. If properly aligned, the diffracted beam must diffract at least twice—once from each surface of the channel—to pass through the channel in the analyzer crystal before reaching the detector. Since it is a single crystal, the diffracted intensity is high, but only a narrow band—a subset of an incoming divergent beam—approximately the Darwin-Prins width [46], will diffract through the crystal for a given orientation. A peak position

measurement requires stepping the analyzer crystal attached to a photon counter across a diffracted ring in 2θ at a small angular step size.* Diffraction peaks measured in this way have a very low background and minimal detector broadening.

Fitting these peaks is typically done using a least squares technique. For synchrotron X rays collected through an analyzer crystal, the peak profile is primarily Lorentzian. A small Gaussian component may also be present such that a Voigt peak profile provides the best fit. However, in some cases the statistical improvement is negligible. Several computer programs such as PeakFit† exist for fitting typical diffraction patterns. The peak center is determined based on a least squares fit to the peak. Errors are also automatically calculated as a part of the peak fitting process. PeakFit reports errors as a 95% confidence limit to the peak center position which is equivalent to a 2σ level of confidence, where σ is the standard deviation for the fit to the peak.

When fitting peaks, the diffraction pattern is input to the software. First, the background function is subtracted. For a well-aligned synchrotron instrument, the background is typically, over small 2θ, a linear noise function close to zero intensity. Some detectors, such as the image plates described below, have exponential background patterns. Samples with amorphous phases may also contribute to a particular X-ray background. Second, the peaks are automatically or manually identified and indexed. If more than one phase is present, multiple peak profile functions may be necessary as each phase has its own peculiarities such as grain size that contribute to the peak shape. For

*0.005^{o} steps were required to define some of the narrow peaks in the experiments performed at APS (Section 4-2). Compare this to a typical setting of 0.02^{o} steps for standard measurements on a traditional Siemens D500 diffractometer.

†PeakFit© is commercially available through Jandel Scientific Software, SPSS Science, 233 S. Wacker Drive, 11th floor, Chicago, IL 60606-6307

example the (220) peak in the β-SiC SCS-6 fibers* is broad due to its small grain size. Including a Gaussian component in the fit to peaks from this phase improves the certainty in the peak center. Finally, for a strain analysis, the center of each peak is determined by minimizing the difference between the estimated peak profile function and the diffraction intensities. Centers reported from such a series of steps may then be immediately converted to lattice spacings. Corrections for inadvertent translation of an internal standard from the center of diffraction may also be performed and the resulting d is input into Eq. 2-1.

Another option for improving the 2θ resolution requires increasing the distance between the detector and the sample. As can be seen from Figure 2-3, when the diffracted beam path length increases, the radius of the diffracted ring increases. Thus, for the same Δd, $\Delta(2\theta)$ covers a longer portion of the detector. In practice, the diffracted beam path is limited by the physical space available to the detector. For low energy diffraction, the 2θ of interest may be large (such as 90^o) and increasing the diffracted beam path requires placing a detector in a space typically unavailable. However, at higher energies 2θ becomes small even for high-order reflections (such as 10^o) and increasing the diffracted beam path simply requires moving the detector away from the sample along the path of the incoming beam, z direction (Figure 2-3).

*The fibers from the composite which will be discussed in detail later (Sections 4 and 5).

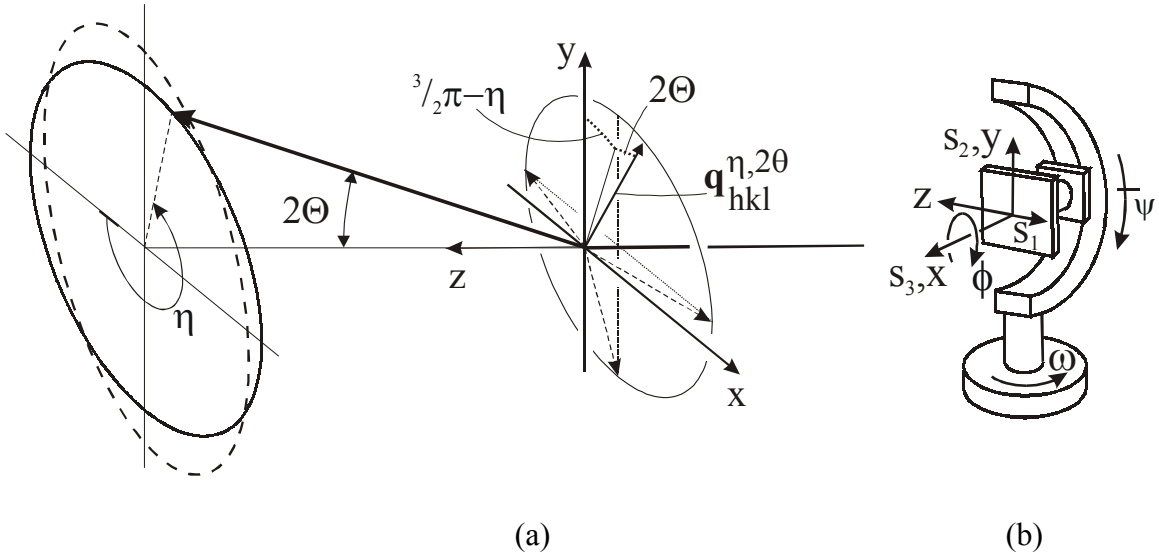

(a) (b)

Figure 2-3 (a) Scattering geometry of a synchrotron experimental setup. *x*, *y*, *z* define the laboratory coordinate system, *z* being parallel to the incident beam, *x* is in the horizontal plane pointing outwards from the storage ring, and *y* is perpendicular to both *z* and *x*. The scattering vector ***q*** and the diffracted beam for a diffracting grain are indicated by solid arrows. Note that all scattering vectors coinciding on a cone with large opening angle (indicated by the dashed scattering vectors) are detected simultaneously on an area detector.

(b) Sample coordinate system s_i. The orientation of the sample coordinate system with respect to the laboratory system is shown for $\omega = \psi = \phi = 0$. (Figure adapted from [47].)

Detectors such as the digital image plate are ideal for higher-energy work. Their maximum 2θ is limited by their diameter to a range suitable for high-energy diffraction. They also have a small pixel size necessary for a high 2θ resolution which may be maximized at large camera lengths (1-3 meters). The imaging plate is based on the delayed luminescence of the alkali-earth halide $BaFBr:Eu^{2+}$ as a result of excitation from X-ray irradiation. The X-ray intensity information stored in the image plate can be recovered by optical stimulation. The mechanism of this system is described in [48].

Once exposed, using a Mar Digital Image Plate* 3450, a read step takes 108 seconds to complete. It contains 1725 pixels across the radius of an image with each pixel covering 100 x 100 μm^2. From an image plate readout, scans simulating the typical 2θ scan may be constructed by plotting the intensity given by pixels at constant η. An example of a scan constructed in this way compared to a scan using an analyzer crystal is shown in Figure 2-4. The scans appear comparable, but for a given energy and alignment, the step size in 2θ may be reduced when using an analyzer crystal. In comparison, the step size across any given peak in the digital image plate is limited by the number of pixels on the image plate.

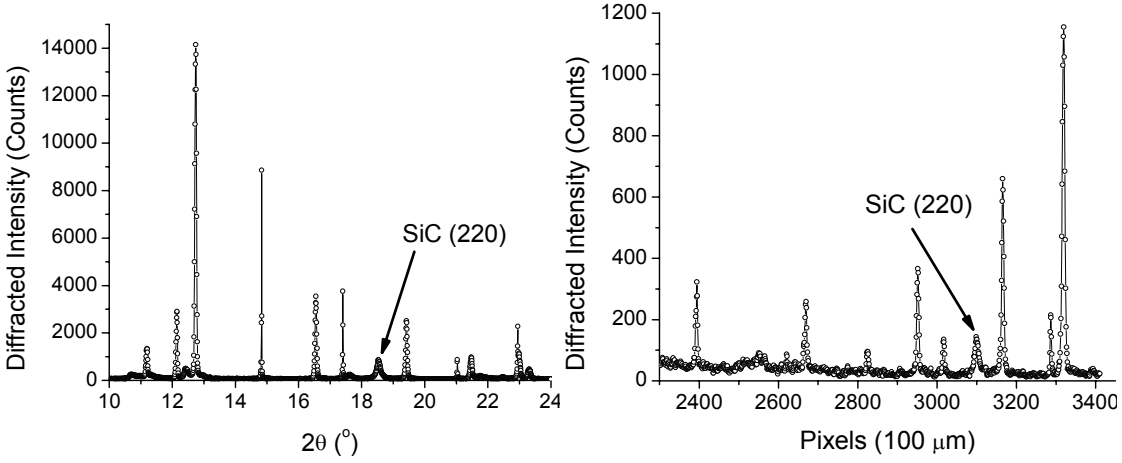

Figure 2-4 Diffraction patterns constructed from a $\theta/2\theta$ scan with an analyzer crystal at 25 keV (left) and using a strip of pixels along $\eta = 0$ from an image plate exposure at 65 keV (right). Notice the peaks are much narrower with fewer data points, marked by an "o," in a peak using the analyzer crystal, but the image plate scan takes less than $1/8^{th}$ the time and includes information from all η. (See Section 4-2 for a fully indexed pattern.)

Similar but more sensitive for digitizing X rays than film [49], the advantage of the image plate is the additional information obtained for all η (Figure 2-3). With the image

*Commercially available from marUSA Inc., 1840 Oak Ave., Evanston, IL 60201, USA

plate, entire Debye-Scherrer rings are captured at multiple *2*θ simultaneously. Using slits and a point detector, the equivalent amount of information could be obtained at the expense of a factor of 10^4 in data collection time [50].

The new technology requires a new method of analysis. Recently, He and Smith published the fundamental strain equation for two-dimensional X-ray diffraction (XRD^2) [51]. They define ln(sin θ_0 / sin θ) as the diffraction cone distortion at a particular (*2*θ, η). Their general XRD^2 equation:

$$f_{11}\cdot\varepsilon_{11} + f_{12}\cdot\varepsilon_{12} + f_{22}\cdot\varepsilon_{22} + f_{13}\cdot\varepsilon_{13} + f_{23}\cdot\varepsilon_{23} + f_{33}\cdot\varepsilon_{33} = \ln\left(\frac{\sin(\theta_0)}{\sin(\theta)}\right)$$

with:

$$f_{11} = A^2 \quad f_{12} = 2\cdot A\cdot B \quad f_{22} = B^2 \quad f_{13} = 2\cdot A\cdot C \quad f_{23} = 2\cdot B\cdot C \quad f_{33} = C^2$$

$$a = \sin(\theta)\cdot\cos(\omega) + \sin(\eta)\cdot\cos(\theta)\cdot\sin(\omega)$$
$$b = -\cos(\gamma)\cos(\theta)$$
$$c = \sin(\theta)\cdot\sin(\omega) - \sin(\eta)\cdot\cos(\theta)\cdot\cos(\omega)$$
$$A = a\cdot\cos(\phi) - b\cdot\cos(\psi)\cdot\sin(\phi) + c\cdot\sin(\psi)\cdot\sin(\phi)$$
$$B = a\cdot\sin(\phi) + b\cdot\cos(\psi)\cdot\cos(\phi) - c\cdot\sin(\psi)\cdot\cos(\phi)$$
$$C = b\cdot\sin(\psi) + c\cdot\cos(\psi)$$

provides the strain tensor for an arbitrary position of the sample and detector. For transmission with ψ = φ = ω = 0, their strain equation reduces to

$$a^2\cdot\varepsilon_{11} + 2\cdot a\cdot b\cdot\varepsilon_{12} + b^2\cdot\varepsilon_{22} + 2\cdot a\cdot c\cdot\varepsilon_{13} + 2\cdot b\cdot c\cdot\varepsilon_{23} + c^2\cdot\varepsilon_{33} = \ln\left(\frac{\sin(\theta_0)}{\sin(\theta)}\right) \qquad (2\text{-}3)$$

with a simplification of the coefficients to

$a = \sin\theta$

$b = -\cos\eta \cos\theta$

$c = -\sin\eta \cos\theta$

A computer program was written which is capable of performing a least squares fit of the strain equation to the diffraction data (see Step 3 below). The software solves for the full tensor given in (2-3). In the case of the composite studied, a two-dimensional strain state was measured; so the calculated ε_{33} was averaged with the calculated ε_{11} giving the true ε_{11} (see Appendix C for calculation details). In general, this does not have to be the case. The advantage of the two-dimensional method used here is the reduction of error by including the redundant information. For a biaxial strain state, the strain measured at $\eta = 0^o$ should also be measured at $\eta = 180^o$. Furthermore the strain measured at $\eta = 0^o +/- \Delta\eta$ provides the same information as that measured at $\eta = 180^o +/- \Delta\eta$. Thus, half the information in each exposure is not unique (assuming a continuum mechanical state*) and serves to reduce the error in the analysis.

The analysis was developed for determining the *hkl* specific two-dimensional strain tensor of multiple diffracting phases. Automation of the analysis enabled practical implementation of spatially resolved measurements. The digital image plate can scan, readout, and prepare for a new scan in 2 minutes. Without automation, analysis of the same scan could take hours. Automation reduced the analysis time per scan to about 5 minutes depending on the computer power and number of phases present.

---

*A state in which local strain gradients must be continuous. A state that may not exist if, for example, too few grains are sampled by the beam.

The automated analysis, adapted from [47], consists of three main steps:

1) Convert the image plate data into a calibrated file useful for further analysis.
2) Fit the peak in 2θ at each η for all rings of interest.
3) Solve the strain tensor for each ring of interest using all peak positions from Step 2.

The analysis program was written in MatLab* using separate MatLab code specific files as modules for each substantial step in the analysis. Initial calibration and conversion of the image plate files was performed using macros running on a software package called, Fit2D†, developed by Andy Hammersley at the European Synchrotron Radiation Facility (ESRF) [52] (see Appendix B for the necessary Fit2D macro).

Calibration of images for accurate displacement measurements is common practice for industrial machine vision applications. Proper calibration requires imaging an object of known dimensions using identical optics as will be used for the test measurements. An array of objects filling the aperture at known spacing allows for nonlinear corrections or unwarping of the entire face of the imager. In the case of strain measurements using XRD^2, a strain-free reference powder may be used to calibrate the image plate [52]. Using the same optics as will be used for the strain measurements, the diffraction rings of the reference powder are fit to an ellipse (or series of ellipses if more than one ring is available). Tilt misalignment may then be compensated for by digitally correcting for the eccentricity of the standard ellipse. This eccentricity would be interpreted as deviatoric

*MatLab© is commercially available from The MathWorks, Inc., 3 Apple Hill Drive, Natick, MA 01760-2098.
†Fit2D is freely distributed software available from: http://www.esrf.fr/computing/scientific/FIT2D/index.html.

strain if the image is not calibrated. Fit2D provides a function for this calibration step including built-in tools for common standard powders such as Si or CeO_2.

Step 1:

Once the image plate is calibrated, the automated procedure may begin. First, the images are converted from radial coordinates to rectangular coordinates. Performed using Fit2D, this conversion is based on the results of the initial calibration. For conversion, the image is cut into radially symmetric 2θ bins of constant arc length along η. This arc length may vary from sub-degree values to a maximum integration around the full 360^o available. Smaller values improve the potential to observe deviatoric strain, but they also increase the time required for the analysis. A larger value of arc length serves to improve the number of grains contributing to each arc length similar to the effect rocking along ψ would have in a more traditional experiment. The resulting rectangular image has 2θ as its x-axis and η as its y-axis (Figure 2-5). This step provides an opportunity to check the calibration, for if properly calibrated, in this rectangular form rings from a phase with no deviatoric strain give a constant 2θ for all η and appear straight in the converted image (vertical lines in Figure 2-5). All rings from the strain-free powder should become strait in the converted image. If the strain-free powder does not result in straight lines in the converted image, the powder is not strain-free or the calibration of the image plate is incorrect. Once the calibration is verified, the image is saved in Tagged Image File Format (tiff) and is ready for strain analysis.

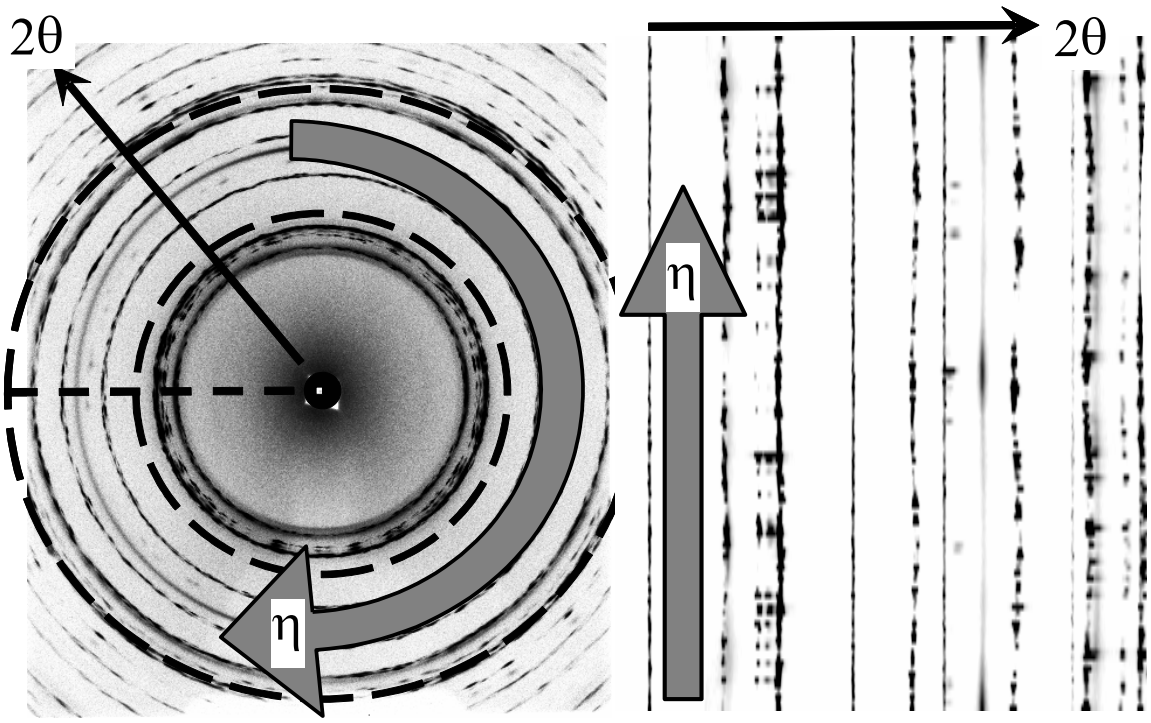

Figure 2-5 The image plate, initially exposed with rings in a radial format (left), is converted to a Cartesian format (right) for analysis.

Step 2:

MatLab reads the 16 bit tiff files as a matrix with the intensity of each pixel in the tiff file assigned a column and row position based on its pixel position in the image. After reading the image into MatLab, a peak fitting routine is used to determine the *peak center* position as a function of pixels along the *x*-axis (originally the *2*θ direction).* This peak fitting routine is repeated for each row of pixels. The rows are associated with a range in η determined by the image conversion in Fit2D described above (in this analysis η was broken up into 120 3° segments by the macro in Appendix B). The peak center, full width at half maximum intensity (FWHM) and total integrated intensity are recorded for

*See above to Figure 2-4 for a comparison between pixels and 2θ.

each peak. Error in the peak position which improves as the inverse root of the relative peak intensity is calculated assuming a Gaussian error distribution as standard in least squares fitting—a built-in function of the MatLab least squares fitting routine. This second step of the analysis is the most processor intensive and is typically repeated for all images processed by Fit2D in the first step.

Step 3:

Lastly, the *peak centers* obtained in Step 2 are fit to the strain equation, Eq. (2-3) [47, 50, 51]. In Step 2 above, the fit was directly to the diffraction peak (at each η bin). Here, in Step 3, the least square fit is to the *peak centers* already solved in Step 2 at all η. The errors from the peak fits in Step 2 are propagated through to Step 3 where a total χ^2 and error in strain is calculated. The χ^2 represents the sum of the difference in the fit of strain equation to the weighted peak centers determined in Step 2. The weight of the peak position for each azimuthal row is determined by the error for the peak at that η diminishing the influence of low intensity regions of the ring, which becomes important for grainy or highly textured rings. As in Step 2, the error estimation—a built in function of MatLab—assumes a Gaussian error distribution as standard in least squares fitting. For example, a high-intensity portion of the ring at η_1 would have less error in the peak center along 2θ for the least squares fit to that peak than a low intensity portion of the same ring at η_2 where the peak center determined by the same least squares fitting procedure is less certain. By keeping track of these errors, the 2θ value (*peak center*) from η_1 has more influence than the 2θ value given by the lower intensity region at η_2 making the strongest reflections have the greatest weight in the strain calculation. The least squares fit to the strain equation, Eq. (2-3), is repeated for each ring of interest and

the resulting strain is tabulated in a text file for graphing and analysis of the mechanical properties of the diffracting phases. The MatLab scripts used for this analysis are found in Appendix C.

One drawback to this analysis is its sensitivity to outliers. A short range in 2θ is selected for each peak of interest. This predetermined $\Delta(2\theta)$ is used as a window for fitting the peak. If the peak resides outside the window, or a second peak enters the window, false peak positions may be recorded. This possibility limits which rings may be considered for analysis as they must be clear of neighboring rings and have sufficient intensity to provide a solution to the peak fitting routine. As the beam size is reduced, variations in intensity around the ring increase. This is due to a decrease in the number of grains diffracting for the reduced beam size. In the case of highly textured minority phases, the intensity may be restricted to a small region in η. While a narrow acceptance window or $\Delta(2\theta)$ may eliminate the majority of outliers, a $\Delta(2\theta)$ which is not a function of η is restricted by Poison's ratio to a value larger than otherwise necessary. In addition, using the current method, $\Delta(2\theta)$ must be large enough to accommodate the change in radius associated with the change in strain for the phase of interest. Both of these restrictions open up the analysis to accept potential outliers and restrict some rings from the analysis.

Resolving these restrictions requires an iterative approach to fitting the diffraction ring as a whole. Varying $\Delta(2\theta)$ appropriately as a function of η and ε improves the analysis method allowing the incorporation of more rings. Including more rings in the analysis is the first step to adopting a Rietveld approach to fitting the two-dimensional diffraction pattern. While software exists for analyzing image plate information with

Rietveld, these methods work best when a hydrostatic stress state is assumed for the phases—an oversimplification for a general XRD^2 strain analysis [53].

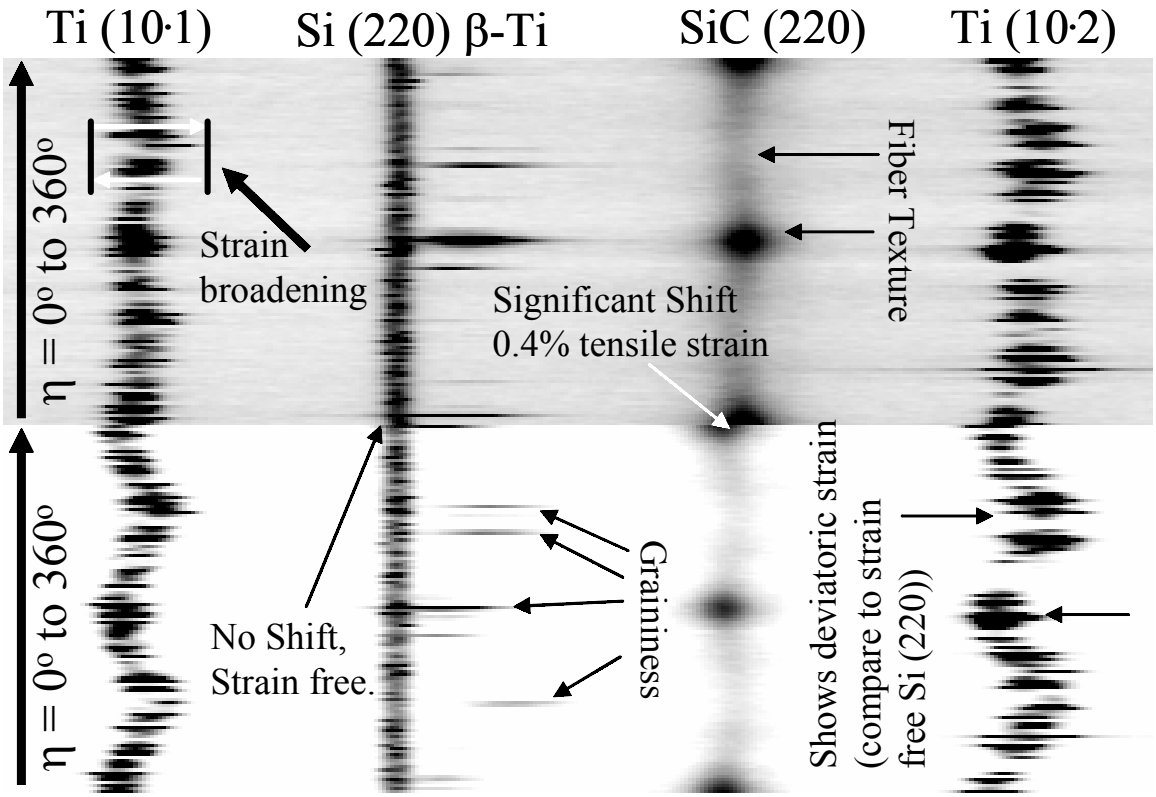

Figure 2-6 A zoomed-in view from two exposures of the image plate on the Ti-SiC laminar composite (see Figure 2-5 for coordinates). The first (top) is at 0 MPa applied stress, the second at 850 MPa. Axial strains appear as shifts between the two frames directly at $\eta = 0^o$, 180^o and 360^o. Transverse strains are visible at $\eta = 90^o$ and 270^o. For all other η the strain is a combination.

The above one- and two-dimensional analyses were used to measure the residual and applied strains in several Ti-SiC composites. Automation of the procedure and analysis enabled a detailed study of the micromechanics of the composite. As can be seen from Figure 2-6, a wealth of information specific to the composite is available from the two-dimensional analysis. Within certain limitations, the analysis may be extended to other composites with diffracting phases. Critical issues include the three-dimensional strain

state, suitable grain size, X-ray penetration, a mechanism for applying stress, available standards, and alignment of the sample plus goniometer. The expected strain state of the Ti-SiC composite will be discussed in the next section. The grain size limitation depends also on the beam size and will be dealt with in Section 5. Here the laminar composite was ideal since X-ray penetration becomes less of an issue as the X-ray energy increases, but for some other samples it is still an issue. Application of stress was dealt with above (2-1.1), but some detriments of weak grips will be seen in Section 4-5. Available standards and proper alignment of the sample cannot be over stated. For instance, the residual strains reported in Section 4-4 would have been subject to an average translation error of 60 x 10^{-6} strain without the use of an internal standard (Figure 2-7).

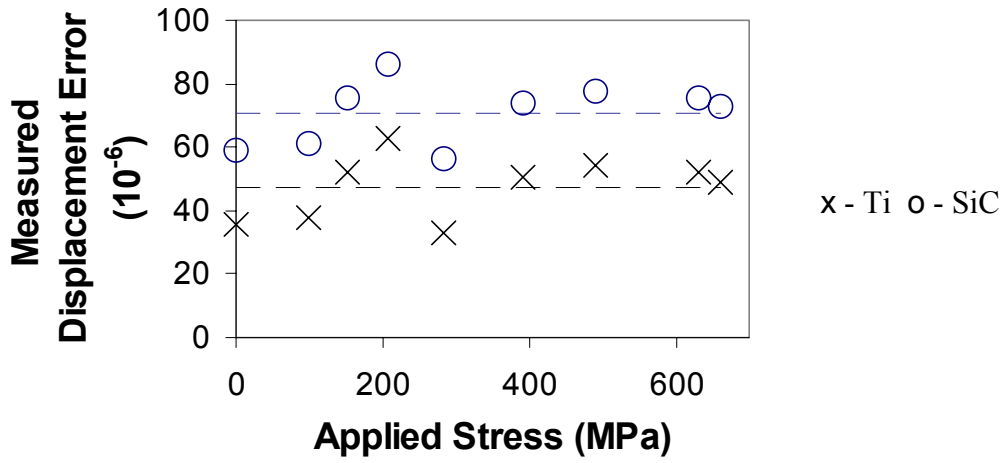

Figure 2-7 The translation error vs. applied load corrected for in the Ti-SiC composite. An internal Si standard powder on the composite surface provided this information.

3. Two-Dimensional Fiber Composite Models

This section describes two models which were used to interpret the strains measured in the Ti-SiC composite. As will be seen in Section 4-1, the Ti-SiC laminar composite possesses geometric, mechanical, and X-ray optical properties well suited to a mechanical study. It is both a practical composite and a model composite allowing the development of an analysis method which will be applicable to the study of MMCs in general while at the same time able to reveal specific behavior of academic and industrial value. The first model described here uses the commercially available finite element code ABAQUS* to predict the bulk properties of the composite. The second model, while also built on the finite element method, is based on the shear lag concept simplifying the calculations necessary to handle the strain fields resulting from damage in the composite.

3-1. *A Finite Element Model for Ti-SiC*

To better understand the bulk evolution of internal stresses/strains in the undamaged composite, a finite element model (FEM) was developed. This model assumes plane strain conditions because of the continuous fiber geometry. However, due to the mechanical loading along the fiber direction, it was necessary to use a full three-dimensional model. The plane strain assumption is then invoked by keeping the planes perpendicular to the fiber direction (z = constant) as planes (Figure 3-1 (a)). The plane parallel to the fiber where x is equal to half the fiber spacing is also kept planar to produce a continuous boundary condition for an infinite number of fibers. The surface of

*ABAQUS is available for an annual fee from Hibbitt, Karlsson & Sorensen, Inc., 1080 Main Street, Pawtucket, Rhode Island 02860-4847.

the composite (where $y = t/2$) is free to deform. The planes $x = 0$, $y = 0$, and $z = 0$ are general symmetry planes. The relative dimensions of the fiber and matrix regions in the model were adjusted to obtain a fiber area (and volume) fraction of 0.32 to correspond to the measured value.

The measured thermal residual strains (see ahead to Section 4-4, Table 4-1) were included in the calculation as they would be present in the initial state of the composite before tensile loading. The material parameters for the matrix and the fibers were taken from refs. [54, 55]. Specifically, the room temperature values of the elastic constants for the matrix were E_m = 125 GPa and ν_m = 0.31, whereas those for the fibers were E_f = 393 GPa and ν_f = 0.25 (both were assumed elastically isotropic as a first order approximation) [54]. The variation of these elastic constants with temperature was also included in the calculation in addition to the temperature-dependent values of CTEs given in [54]. The fibers were assumed linear elastic and intact throughout the loading. Note that the tensile strength of the SCS-6 fibers is known to exceed 3 GPa [56]. The Ti-6Al-4V matrix was modeled as an elastic-plastic material with a yield strength of 725 MPa (where first deviation from linear elasticity occurs), an engineering yield strength ($\sigma_{0.2}$) of 920 MPa and a linear strain-hardening coefficient of 1.63 GPa. These parameters were deduced from ref. [55] where the tensile behavior of a monolithic Ti-6Al-4V alloy was determined. A necessary starting point, since specific changes in the alloy's material properties as a part of the composite are unknown and hence a topic of this study. Finally, the fiber/matrix interface was assumed intact at all times.

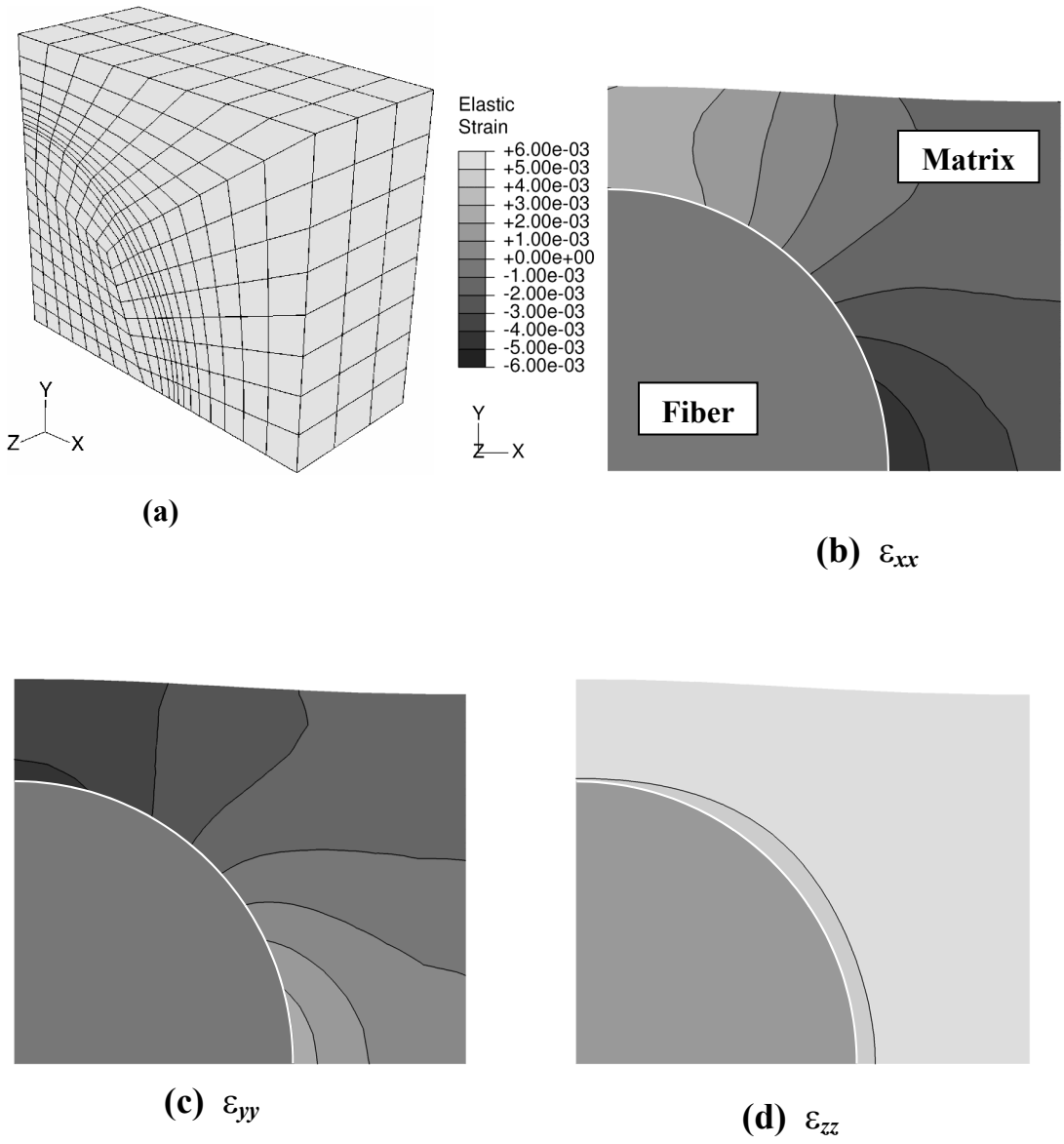

Figure 3-1 Finite element model (FEM) geometry and predictions of elastic strains at 650 MPa applied composite stress (along fiber axis, i.e., the *z* direction). (a) Mesh used in the FEM calculations. (b), (c) and (d) Normal strain distributions along the *x*, *y* and *z* directions, respectively. In (b) and (c), significant transverse strain gradients are observed across the specimen thickness. There is no variation in the longitudinal elastic strain in the fiber (d), but there is some variation in the matrix due to predicted plastic deformation around the fiber. Average longitudinal strains in the fibers due to the applied stress alone are around 3040 με while they are about 3110 με in the matrix. These numbers exclude the thermal residual strains and show that no significant plasticity occurs in the matrix at this applied stress.

Figure 3-1 shows the FEM geometry and the predicted elastic strains due to an applied tensile composite stress of 650 MPa. In Figure 3-1 (b) and (c), significant transverse strain gradients are observed across specimen thickness. As demonstrated in ref. [57], this heterogeneity in the transverse strains makes diffraction measurements in these directions highly dependent on positioning and prone to large errors (for example see Section 4-5). Fortunately, there is no appreciable variation predicted in the longitudinal elastic strain in either phase across the specimen thickness (Figure 3-1 (d)). This minimal variation of longitudinal strain aids in the interpretation of the diffraction strains, which represent the bulk average across the specimen thickness (Section 4).

Only a thin layer in the matrix around the fiber shows a decrease in elastic strain due to initiation of plastic deformation. The FEM predicts the plastic deformation in the matrix to start around 150 MPa applied composite stress. This occurs due to the three-dimensional stress state at the interface, i.e., the matrix has longitudinal and tangential tension and radial compression resulting in a large von Mises stress at the interface that exceeds the uniaxial yield strength (725 MPa). Note that the contour plots in Figure 3-1 are shown in the deformed geometry. The deformations have been multiplied by a factor of 20 for clarity. It is observed that there is a periodic variation in the thickness of the composite as the transverse contraction in the fiber under tension is much less than that in the matrix, rendering the estimated thickness at the positions of the fibers slightly larger than that in between the fibers. The three-dimensinal FEM provided a context to explore and understand the bulk properties of the composite as well as verifying the homogeneity of axial strains required for application of through thickness averages to the predicted

axial strains of both models. The predictions from this FEM are compared to the measured bulk composite strains in Section 4.

3-2. *A Micromechanics Model for Damaged Ti-SiC*

Several theoretical models have been developed to predict stress distributions in fibers and matrix near clusters of fiber breaks in unidirectional composites. Earlier work employed load sharing rules, such as local load sharing and global load sharing (GLS) to approximate such stress distributions generated by fiber breaks. Simple rules allowed analytical probability analyses of sequential fiber breaks and the prediction of strength for small composites, see for example [58, 59, 60, 61]. In general GLS, with no stress concentration and constant interfacial sliding, has been successfully applied to ceramic matrix composites, see for example [62, 63]. Another class of more physically based load-sharing models is composed of models utilizing shear lag assumptions; these essentially model the fibers as one-dimensional structures and the matrix in-between as deforming only in shear. Such a shear lag analysis was first applied to fiber composites by Hedgepeth [64]. In his original work, Hedgepeth obtained analytical solutions for the stress (or strain) concentration factors (SCFs) in intact fibers due to broken fibers in multifiber, two-dimensional, linear elastic composites. Since then, there have been numerous extensions of his model to consider other cases [65, 66, 67]. Considerable simplification usually accompanies such shear lag load transfer models. Characteristic assumptions are the tensile load is carried solely by the fibers and the load carried by a fiber prior to fracture is transferred to the neighboring fibers by simple shear deformation of the surrounding matrix. The Hedgepeth shear lag model is most accurate when the fiber volume fraction, f, and the fiber/matrix modulus ratio, E_f / E_m, are high, i.e., $E_f f >> E_m(1-f)$. This condition applies to most polymer matrix composites (PMCs), and to some MMCs with high f values, where E_f / E_m typically ranges from 4 to 6. However,

many composites of current interest, such as most MMCs and some PMCs with low f values, do not fall into this category. Several recent studies using micro-Raman and piezospectroscopic techniques have shown that as the interfiber spacing increases, the stress concentrations in the immediate neighboring fiber decreases [6, 12, 13, 14]. Shear lag models that do not consider longitudinal matrix stiffness have been unsuccessful in interpreting this trend.

In Hedgepeth's original analysis, the fibers and matrix were assumed intact and elastic. In addition, only the longitudinal stress in the fibers and shear stress in the matrix were predicted. Clearly, other stress components influence stress transfer, so their incorporation would make the model more realistic and potentially capable of interpreting experimental strain measurements. Therefore, several authors have extended the shear lag model of Hedgepeth for matrices that sustain a portion of the applied tensile stress [65, 66, 67]. In particular, an elastic model proposed by Fukuda and Kawata [65] included, for the first time, effects of f on the peak stress concentration factors, considering both the longitudinal and shear stiffness of the matrix carrying shear and tensile stresses. Their numerical results showed that the SCF on adjacent fibers increases with decreasing inter-fiber distance as well as with increasing elastic mismatch between the fibers and matrix. Others have also allowed the matrix to sustain tension, usually involving detailed three-dimensional finite element [68] or other numerical [66] calculations on a several fiber lamina containing a small cluster of fiber breaks. Comparing these with the original elastic shear lag model demonstrated that the differences diminish as the number of breaks in the cluster and f increase. In virtually all these model variations, relaxing the shear lag assumptions has led to formidable

analytical difficulties and a need for extensive numerical computation even for a composite with relatively few fibers. Moreover, the dependence of the numerical solutions on a majority of the fiber and matrix properties is not conveniently removed through normalizations; therefore, their calculations only apply for a given set of composite parameters.

3-2.1. Matrix Stiffness Shear-Lag (MSSL) Model

Beyerlein and Landis [34] developed the "matrix stiffness shear-lag" (MSSL) model to quickly compute the stresses and displacements of unidirectional fiber composites in response to multiple fiber and matrix breaks. It is intended to predict macroscopic material properties such as toughness and lifetime. Until this work, the model had not been applied to this composite system or tested against spatially resolved matrix strains from a metal matrix composite.

The MSSL model assumes a planar, two-dimensional composite with a single row of aligned, parallel and continuous fibers. The model analysis requires a finite element model of the composite system. Figure 3-2 shows a segment of the mesh, representing a repeating cell in the composite system which is infinite in both the transverse and axial directions. The fibers are represented by one-dimensional axial springs and the matrix region between any two consecutive fiber elements is represented by a pair of rectangular finite elements. Since the transverse displacements are neglected, each element has four degrees of freedom.

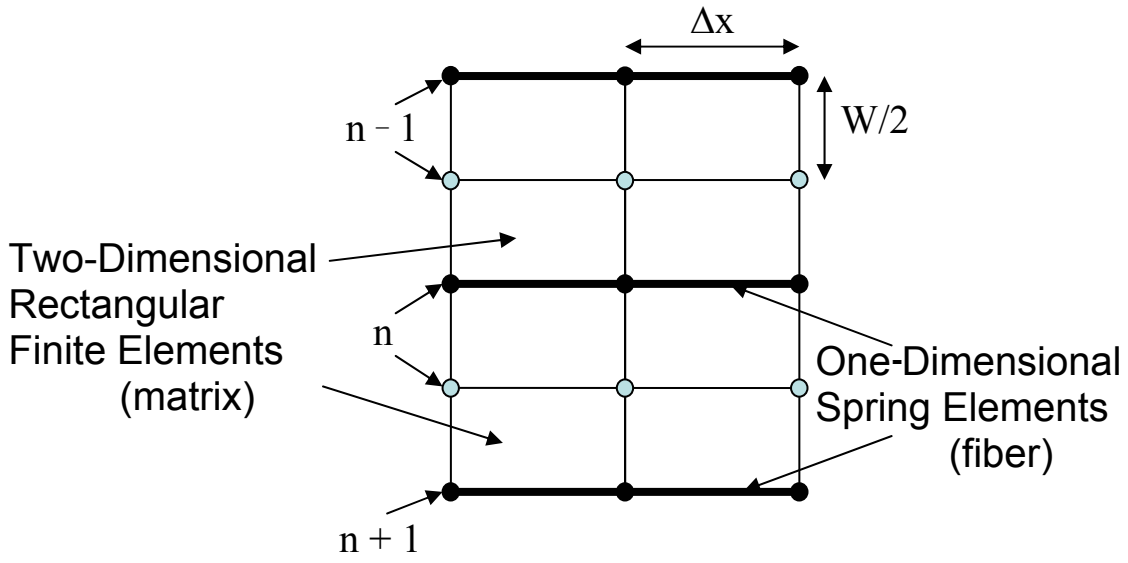

Figure 3-2 A representative finite element mesh from the MSSL model for a laminar fiber composite (adapted from [34]).

The index for the fiber and matrix regions is "*n*." The index *n* for a matrix region is adjacent to the fiber region *n* in the positive direction. The fiber longitudinal coordinate is *x*, and the crack lies along the $x = 0$ plane, centered at $x = 0$ and $n = 0$. The analysis assumes the thickness, *t*, in the out-of-plane direction is the same for the fibers and matrix. The width of each matrix column is *W*, and the width of the fibers is *D*. The transverse displacements of the system and the shear deformation of the fibers are neglected. Both the fiber and matrix are assumed linear elastic and well bonded. Therefore, the relevant material properties are the longitudinal Young's moduli of the fibers and matrix, E_f and E_m, respectively, and the longitudinal shear modulus of the matrix, G_m. As indicated in Figure 3-3, both the fiber and matrix are subjected to a uniform applied stress σ, and thus the same far-field strain ε. This model provides the

average longitudinal strain over the *n*th fiber cross section, $\varepsilon^f_n(x)$, and average matrix longitudinal strain $\varepsilon^m_n(x)$ across the *n*th matrix region *Wt*.

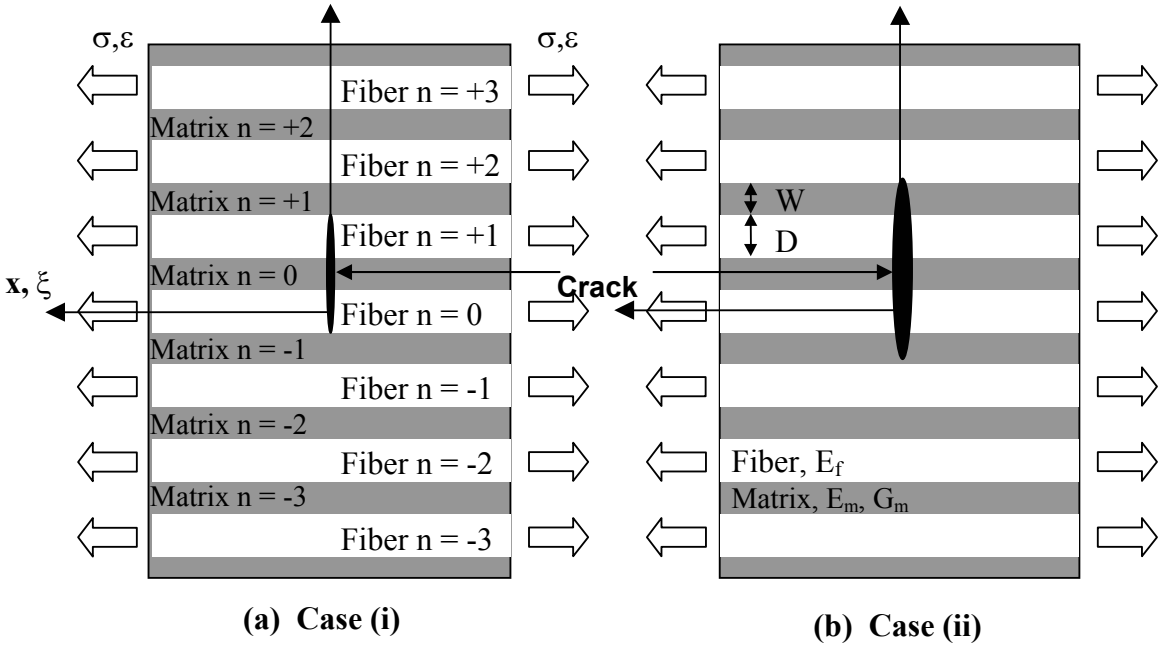

Figure 3-3 Schematic of crack geometries under consideration (adapted from ref. [34]). (a) Case (i): two fibers are broken but the crack-tip matrix regions are intact. (b) Case (ii): in addition to two broken fibers, the crack-tip matrix regions are also broken. Components are numbered with index *"n"*.

As in all shear lag analyses, this model provides the average axial stress over the fiber cross section and average shear stress between adjacent fiber and matrix nodes. For a full description of the governing equations in this model the reader is referred to [34]. The governing equations were derived from a treatment of the FEM in Figure 3-2. Solutions for intact and broken fiber and matrix regions were also found. For particular damage morphology (as in Figure 3-2), the influence superposition technique is used to solve the governing equations. Once the influence functions are determined for a given set of broken fiber and matrix sites, a solution is obtained for the proper weighting factors corresponding to the fiber breaks and matrix breaks such that there exists zero stress at all

broken sites. Practically the model requires a numerical code for its execution. The main advantage of this technique is the computation time involves solving for the weighting factors which only depend on the number of damaged elements in the lamina and calculating the fiber and matrix displacements.

In dimensionless form the strain field solutions depend only on the longitudinal stiffness ratio,

$$\rho = \frac{E_m A_m}{E_f A_f} \tag{3-1}$$

In Eq. (3-1), A_f is the cross sectional area of the fiber, and A_m is the cross sectional area of the matrix between two consecutive fibers. The ratio ρ can range from 0 to infinity, but it is usually between 0 and 1 for most MMCs. For ρ = 0, the model yields the original Hedgepeth solution [64].

The Ti-SiC composite (described in Section 4) was chosen as a model composite for comparison of the strains in each phase predicted by this MSSL model at applied stress. Based on the geometry of the Ti-SiC model composite, the stiffness ratio, ρ, was interpreted and calculated several different ways. For all cases, the elastic constants employed were E_m = 125 GPa, and E_f = 393 GPa [54]. The matrix shear modulus, G_m, was calculated, assuming elastic isotropy in the matrix, using $G_m = E_m / 2(1 + \nu_m)$, with the matrix Poisson's ratio of ν_m = 0.31 [54].

Several conditions for ρ and the number of breaks were characterized in [34]. While the model is intended for use with composites of the laminar variety, the definition of W allows some freedom within a given geometry. In addition, the critical length in the out

of plane direction may be assumed equal to the matrix thickness but is not clearly defined as such. Thus, for the etched Ti-SiC composite described in Section 5-1, ρ was interpreted and calculated in three different ways:

1. ρ_1: Using the full sample thickness (t = 200 μm), the minimum spacing *between* fiber surfaces (W = 100 μm) and a fiber radius of 70 μm;

2. ρ_2: Letting the thickness match the fiber diameter (t = 140 μm) and with the same W and A_f as in (1);

3. ρ_3: Letting the fiber volume fraction equal its area fraction (f = 0.32, the nominal value).

The resulting values for the stiffness ratio were $\rho_1 = 0.413$, $\rho_2 = 0.289$, and $\rho_3 = 0.591$ (see Table **3-1**). In the following analysis it is convenient to normalize the x coordinate along the fiber axis as

$$\xi = \frac{x}{\delta}, \qquad \text{where } \delta = \sqrt{\frac{E_f A_f W}{G_m t}} \tag{3-2}$$

Here, δ is the elastic characteristic shear lag decay length of the fiber stress (or strain) from the maximum to the far-field fiber value as defined in the original Hedgepeth model for ρ = 0 and one fiber break. When the matrix sustains axial load (ρ > 0), this characteristic decay length becomes greater than the value predicted by Eq. (3-2). In general, stress (or strain) decay lengths from fractures will increase beyond δ under matrix and interface plasticity or creep or when there is more than one fiber break.

Two initial cases of crack configuration were considered (Figure 3-3). Since the matrix is assumed to sustain longitudinal tensile forces, the MSSL model will

differentiate between a transverse matrix crack extending from the fiber break to the next fiber, case (ii), versus no crack extension from the fiber break into the matrix, case (i). For case (i) only the matrix regions between broken fibers are broken. For case (ii), in addition to those broken in case (i), the two 'crack-tip' matrix regions between the last broken fiber and first intact fiber are broken. The model assumes the matrix and fiber fractures are infinitely sharp.

At the crack plane, $\xi = 0$, the maximum strain divided by the far-field strain, or Strain Concentration Factor (SCF), of the first intact fiber provides an efficient test of the model's assumptions. For a given number of fiber breaks, the shape of the strain profile and the SCF significantly differ between the two cases, (i) and (ii). For an intact matrix at the crack tips, case (i), the SCF is 1.3 in the first intact fiber. This increases to 1.7 when the matrix is broken, case (ii). With an intact matrix, less load transfers to the fiber, but with a broken matrix, the load formerly carried by both the broken fiber and the broken matrix is shed to the surrounding intact fibers. The MSSL model predicts an intact matrix at the crack tips leads to a strain profile where the maximum SCF in the first intact fiber is slightly displaced from the crack plane (Figure 3-4 (c)). The fiber strain profile is governed by the difference between the decay of the shear strain and the axial displacement of the matrix. The axial displacement dominates near the crack plane giving a slight rise in fiber stress from the crack plane (see ref. [34] for more discussion). When more fibers are broken, the MSSL model also predicts an increase in the SCFs and a broadening of the strain profiles. This enlarges the area affected by the damage zone.

Table 3-1 MSSL model predictions of the axial strain concentration factors (SCFs) in the first intact fiber at the crack plane ($x = 0$) for the Ti-SiC composite.

Shear Lag Decay Length δ **[μm]**	**Stiffness Ratio** ρ	**1 Broken Fiber**		**2 Broken Fibers**	
		Case (i)*: Intact Matrix	**Case (ii): Broken Matrix**	**Case (i)*: Intact Matrix**	**Case (ii): Broken Matrix**
252	0.289	1.14 (1.15)	1.42	1.32 (1.33)	1.70
301	0.413	1.12 (1.14)	1.45	1.29 (1.31)	1.74
329	0.591	1.10 (1.12)	1.39	1.26 (1.28)	1.79

For either case (i) which considers intact matrix at the crack tip or (ii) which considers broken matrix at the crack tip, the SCF shows minimal sensitivity to changes in ρ from 0.289 to 0.591 (see Table 3-1). The more discriminating variable is δ, the shear lag characteristic decay length. This results from the dependence of δ on parameters affecting ρ: A_f, W and t (compare Eqs. (3-1) and (3-2)). Thus, the three available stiffness ratios expand or contract the strain profiles in ξ.

Figure 3-4 compares model predictions of normalized* longitudinal strains $\varepsilon_f/\varepsilon$ as a function of ξ. Figure 3-4(a) illustrates typical differences in the MSSL model predictions

*The numbers in parentheses for case (i) indicate the maximum values of strain concentrations for this case which occur at $x > 0$ slightly away from the crack plane.

of these strain concentration profiles for case (i) and (ii) for $\rho_2 = 0.289$. MSSL model predictions corresponding to the three choices of ρ are plotted in Figure 3-4(b) for case (ii) and two broken fibers. As can be seen from the graph, the choice of ρ affects the gradient of the fiber strain with respect to ξ as well as the magnitude of relative strain for a given ξ. The predicted maximum fiber strain concentrations adjacent to the break are 1.287, 1.316, and 1.258 for case (i); and 1.740, 1.703, and 1.786 for case (ii), for $\rho_{1\text{-}3}$ respectively.

---

*A subtlety within the definition of normalized longitudinal strain lies with the practical definition of the far-field strain which is the denominator in $\varepsilon_f/\varepsilon$ or $\varepsilon_m/\varepsilon$ (normalized fiber or matrix longitudinal strain respectively). Ideally the far-field strain is defined as the strain of the composite an infinite axial distance from the region or (gage section) of interest. Naturally this far-field strain would be equivalent for the matrix and the fibers. However, practically the far-field strain may not be reached within a particular gage section and more likely, even if the far-field strain is asymptotically approached within the gage section, it may not be conveniently measured.

For a particular data set, it may be easily verified that the fiber and matrix strains begin approaching a similar value, but to correctly normalize the strains to the (possibly fictitious) far-field strain, the strains must actually be "normalized" with the strains measured at large ξ. This strain is not necessarily constant from matrix to fiber (or broken matrix to broken fiber) region but should be similar, if ξ is sufficiently large. To correctly account for this practical "normalization" in the comparisons between the data and model, the resulting "normalized" strain at large ξ is not set equal to one, but equal to the strain predicted for that region at the equivalent ξ for which it was "normalized" (for example 0.98 or 1.02). This results in the same value as measuring the ideal far-field strain and normalizing conventionally.

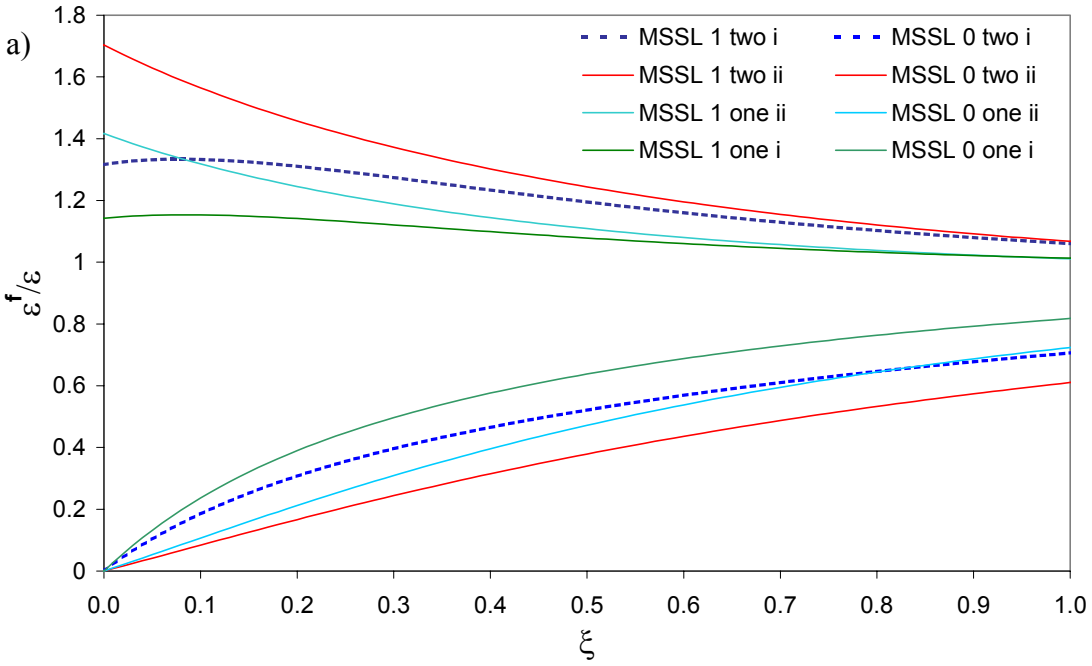
a)
MSSL 1 two i
MSSL 0 two i
MSSL 1 two ii
MSSL 0 two ii
MSSL 1 one ii
MSSL 0 one ii
MSSL 1 one i
MSSL 0 one i
$\varepsilon^f/\varepsilon$
ξ

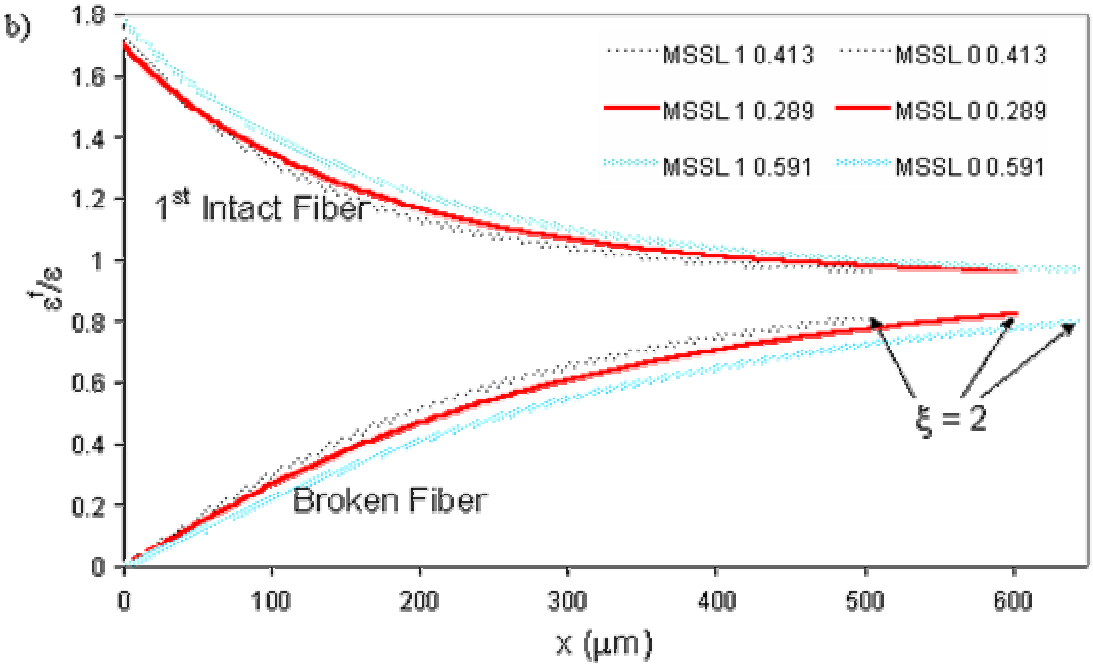
b)
MSSL 1 0.413
MSSL 0 0.413
MSSL 1 0.289
MSSL 0 0.289
MSSL 1 0.591
MSSL 0 0.591
1st Intact Fiber
Broken Fiber
ξ = 2
$\varepsilon^f/\varepsilon$
x (μm)

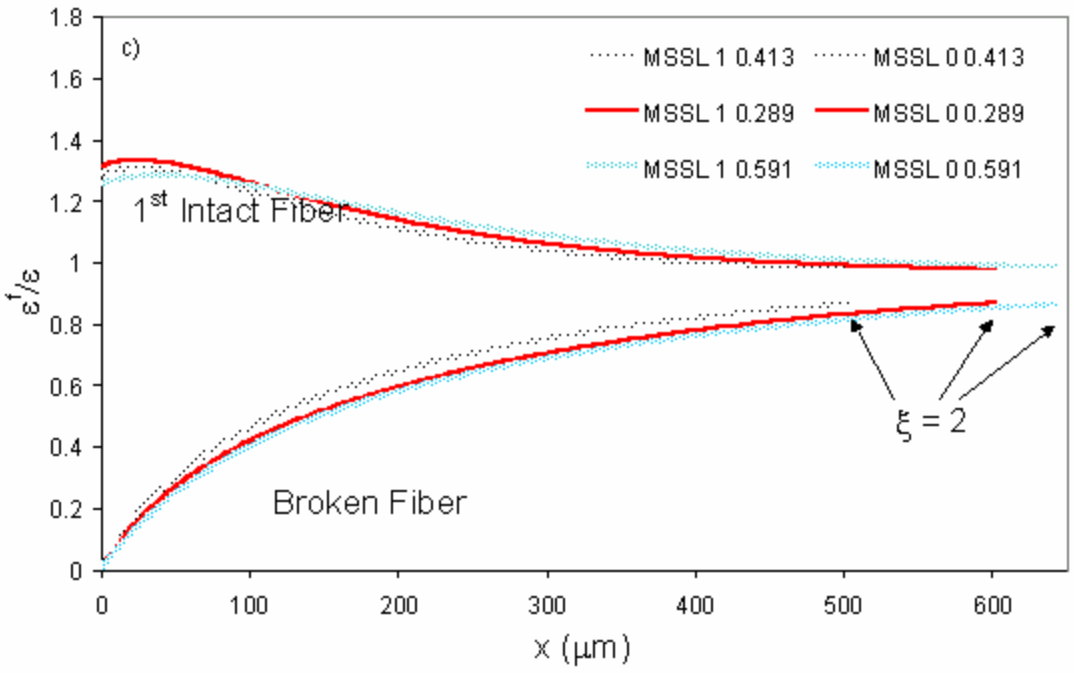

Figure 3-4 a) Case (i), and case (ii) with $\rho = 0.289$ for both one and two broken fibers. b) Comparison of each predicted relative strain value for each ρ value assuming two fiber breaks and case (ii). Under case (ii) for the first intact fiber next to the break $\varepsilon^f/\varepsilon$ is greatest for $\rho = 0.591$, while it is least for $\rho = 0.289$. c) Under case (i) for the first intact fiber next to the break $\varepsilon^f/\varepsilon$ is greatest for $\rho = 0.289$, while it is least for $\rho = 0.591$. Case (ii) and (i) refer to strain profiles for fibers with and without failure in the matrix adjacent to the fiber break respectively.

Clearly, the fiber most sensitive to initial assumptions in the model is the first intact fiber next to the break. Even for this fiber, the predicted difference for each value of ρ is small compared to the differences seen in the strains for case (i) or case (ii). In the MSSL model, unlike in typical shear lag analyses, the shear stresses and strains are not constant from fiber surface to fiber surface since the matrix sustains longitudinal load. For simplicity, the model divides each matrix region in half and calculates the shear strain, $\eta_{n,n}$, and stress, $\tau_{n,n}$, in the left half and right half of any matrix region n (Figure 3-2). At a fixed x, the gradients in shear stress between fiber surfaces increase with ρ. For case

(i), the shear stress near the break increases significantly with ρ. For case (ii), the shear stress along the nearest neighboring fiber increases with ρ. However, since primarily longitudinal rather than shear strains were measured,* the predicted longitudinal strains were used to verify the MSSL model.

Because of the MSSL model's earlier successes for polymer matrix composite systems with large ρ, its intended applicability to composites such as Ti-SiC with smaller ρ values, and its ability to track damage evolution, an investigation to its validity was warranted [34]. In addition, the advantages of the HEμXRD^2 method are particularly suited to comparisons with the MSSL model. Namely, the access to thickness-averaged, spatially resolved, phase-specific elastic strains provided the opportunity to check the MSSL model using a Ti-SiC composite.

*Shear strain was measured only with the image plate which was used for the second damaged composite (Section 4-2).

4. Bulk Deformation of Ti-SiC Composites

The following describes the experimental procedure and results obtained from a study of the phase-specific bulk deformation properties of the Ti-SiC composite. The bulk properties are defined as properties common to the composite as a whole. Rather than specific to a particular region (such as a particular fiber), they are averaged over many fibers and surrounding matrix. The phase-specific bulk properties provide insight on the general behavior of the fiber and matrix as they co-deform. For example, such understanding is necessary to identify to what load the matrix remains elastic or the presence and evolution of residual strains. Each phase's individual mechanical response typically contrasts with its monolithic behavior revealing material characteristics peculiar to the interactions between each phase in the composite. This sometimes complicated behavior is best understood in the context of a suitable model such as the FEM described in Section 3-1. The following includes such a comparison ultimately providing the background for the micromechanical study presented in Section 5.

4-1. *The Ti-SiC Composite*

In general, Ti-SiC composites are intended for moderately high-temperature structural applications and various versions of the composite have received interest in the literature due to its thermal residual strains [54, 69, 70, 71, 72]. The selected composite system consisted of a single row of unidirectional SiC fibers (Textron SCS-6, 140 μm in diameter) in a Ti-6Al-4V matrix, prepared by a proprietary technique at 3M Corp. (St. Paul, MN 55144). For the composite examined here, the fibers were uniformly spaced

with an average center-to-center distance of 240 μm. The fiber area fraction was 32%, in agreement with the value provided by the manufacturer [73].

The SCS-6 fibers consist of a carbon core upon which SiC is grown through a two stage technique similar to vapor deposition involving the chemical decomposition of a silane-hydrogen gas mixture on a resistively heated graphite coated carbon monofilament. The resulting grain size in the fibers is on the order of 200-300 nm in the radial direction and 50-100 nm in the axial direction [74]. The fibers contain the cubic phase of SiC (β-SiC) and show crystallographic texture with the (110) plane preferentially aligned perpendicular to the axis of the fiber. The space group for β-SiC is F -4 3 m [75]. A cross sectional view of the composite is shown in Figure 4-1. The carbon core of the SCS-6 SiC fiber is clearly visible in this image.

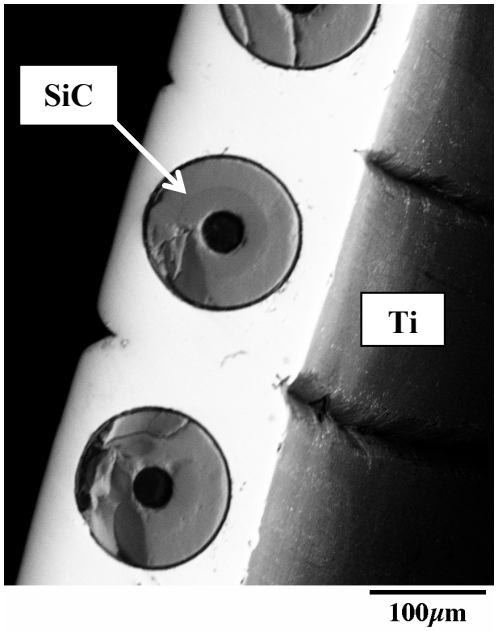

Figure 4-1 Scanning electron microscope (SEM) image of a typical specimen cross section. The fibers are 140 μm in diameter and are almost uniformly spaced with an average center-to-center distance of 240 μm. The carbon core of the SCS-6 fibers is visible as the dark circle in the center of the fibers. Two shades of SiC are also visible in the fiber corresponding to the two stages of SiC growth in manufacturing. The final dark ring around the fiber results from a protective carbon coat applied to the finished fiber. The cracks observed in some fibers occurred during specimen preparation. The total specimen thickness is about 200 μm. The shallow grooves seen in the Ti matrix are a result of the composite processing.

The samples were sliced to a 10 mm width from a 16 mm wide strip. In order to increase the stress at the gage section, the samples were electric discharge machined (EDM) to a 7 mm gage width. To prevent oxidation at the surface of the sample, Al plates were used to hold the strip. Aluminum oxidizes more easily than titanium. If not used, a TiO_2 film would form on the composite which would add noise to the diffraction patterns and alter the residual strains at the surface of the matrix. The remaining specimen dimensions were thickness, t = 0.20 mm, gage length, L = 26.00 mm (Figure 4-2). A 120 ohm strain gage was attached to measure the applied macroscopic strain at the surface in the longitudinal direction, parallel to the fibers (Figure 4-2).

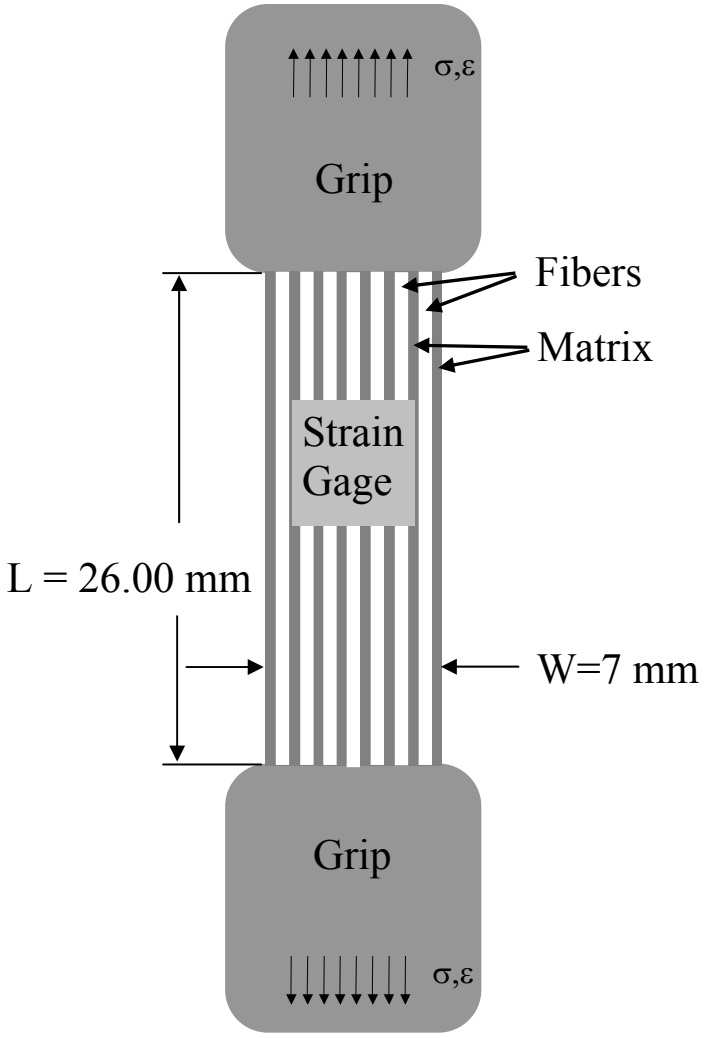

Figure 4-2 Schematic showing the composite geometry used in bulk XRD experiments. The composite thickness was 0.2 mm. Fiber positions are represented by white lines within a gray matrix (for illustration only – not to scale).

4-2. *X-Ray Diffraction Method*

The samples were examined using 25 keV X rays (wavelength, $\lambda = 0.496$ Å) at the 1-ID-C beam line (SRI-CAT, Sector 1), Advanced Photon Source (APS), Argonne National Laboratory. This energy was selected to assure sufficient penetration depth. For this composite, 25 keV X rays transmit 58% of the incident beam intensity. Assuming an exponential decay in the transmitted beam intensity from the sample surface inward, the midpoint of the sampling volume is 91 μm from the surface facing the incoming X-ray beam. Therefore, these measurements were not confined to a thin surface layer but were representative of the entire thickness of the composite (200 μm).

To obtain the desired diffraction geometry (see Section 2-2, Figure 2-3), a four-circle goniometer was used in transmission mode (Figure 4-3). The diffraction vector was along the fiber axis, thus the diffraction patterns provided the longitudinal (or axial) strain in the plane of the composite. The diffraction intensity was collected with a NaI scintillator detector equipped with a Si (111) analyzer crystal. As described in Section 2-2, the analyzer crystal improves the ultimate strain resolution. The X-ray beam size was defined by slits on the incident beam side. An internal standard Si powder (NIST, Standard Reference Material 640a) was attached to the specimen surface.

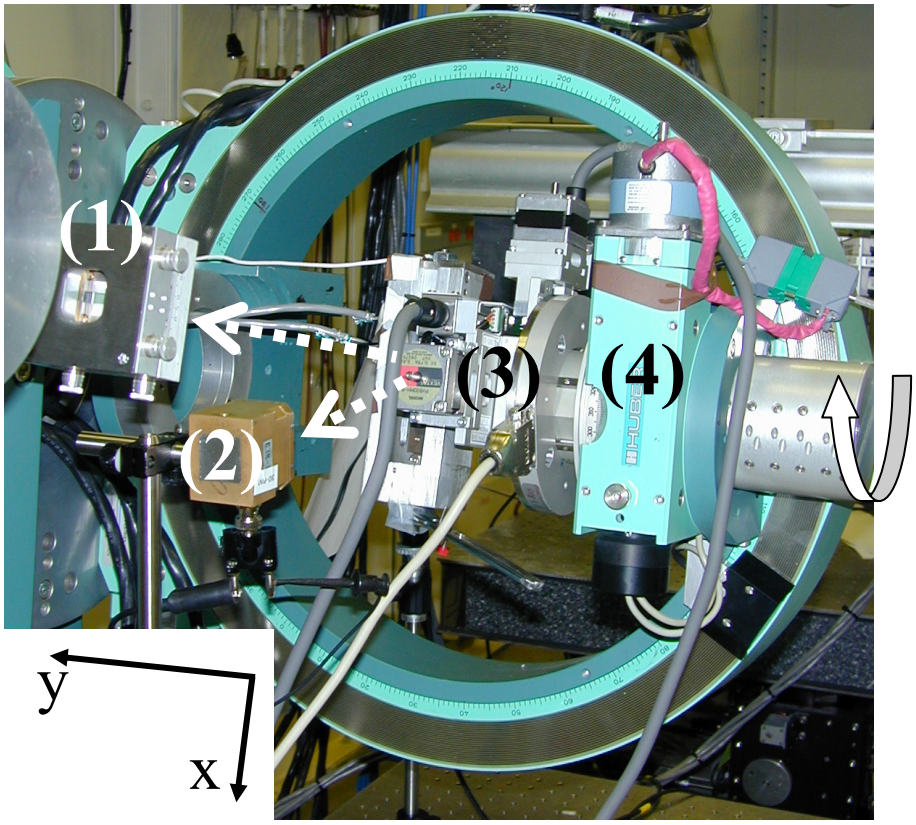

Figure 4-3 Photograph of the experimental setup used for the 25 keV measurements. The dashed line represents the transmitted and diffracted beam paths. The labels are as follows: (1) receiving slit, (2) Si diode beam stop, (3) translation stage, and (4) ϕ stage. θ and 2θ rotate about the y axis as shown by the curved arrow. See also Figure 2-3 b.

A nominally damage-free composite was scanned with a 2 x 2 mm^2 beam to obtain the average bulk residual strains and response of the composite to applied stress. The $\theta/2\theta$ scans were conducted over a range of 2θ = 10° to 24° (for indexed peaks, see Figure 4-4). The diffraction patterns exhibited reflections from β-SiC, α-Ti, Si powder, and to a lesser extent β-Ti, which comprises a small fraction of the matrix. In order to allow Rietveld refinements [76], 0.007° steps in 2θ were used. The Rietveld analysis was performed using the GSAS package [77]. In addition, individual peaks were also fit using a Lorentzian peak shape (peak fit method described in Section 2-2). Limited by goniometer motor speed, the long scans required 24 minutes to complete.

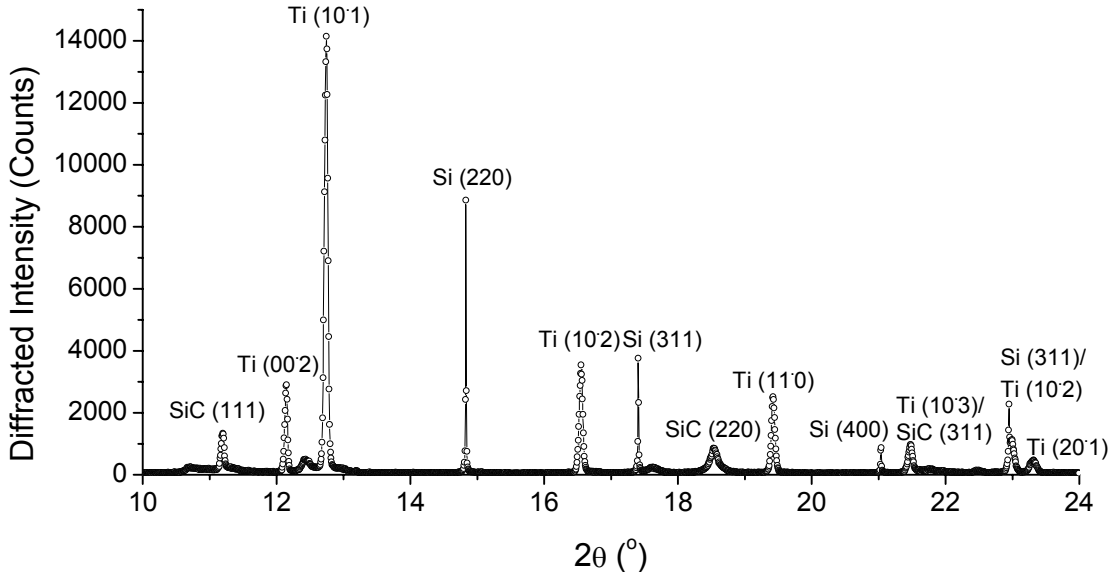

Figure 4-4 Indexed diffraction pattern for a θ/2θ scan of the Ti/SiC composite using a 2 x 2 mm^2 X-ray beam at 25 keV and a point detector.

A second undamaged composite was also illuminated with an X-ray beam of 0.5 x 0.5 mm^2, but at a much higher energy, 63.5 keV (λ = 0.190 Å). A photograph of the experimental setup is shown in Figure 4-5. The higher energy decreases the *2*θ angle of the diffraction rings allowing use of a digital image plate for recording the entire diffraction ring as apposed to the narrow slice of the ring collected with the analyzer crystal and scintillator detector (see Section 2-2 for the analysis procedure). The primary advantage of the image plate for this composite is the additional diffracting grains included for strain analysis. By including more grains, the measured average stress state better represents the stress state of the material examined. Therefore, with the area detector, the X-ray beam spot size can be reduced without the same loss in grain

representation normally seen with the point detectors [50] (an example using a microbeam will be shown in Section 5).

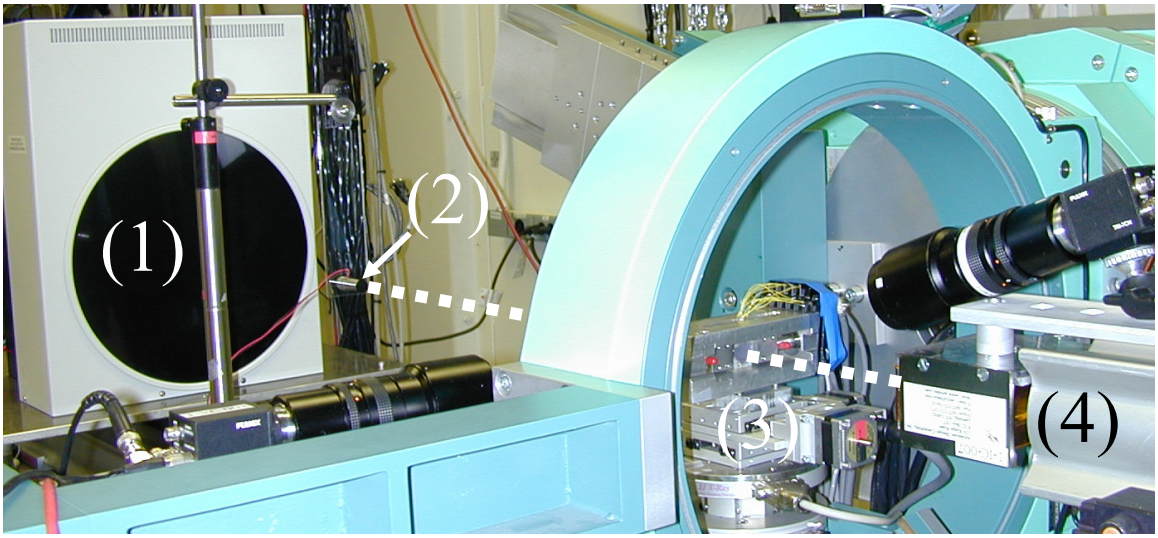

Figure 4-5 Photograph of the high-energy experimental setup. The incoming and transmitted beam path is represented by the dashed line. The image plate (1) is 1111 mm from the sample. A Si diode (2) acts as a beam stop also capturing the transmitted intensity. The translation stage (3) supports the load frame in a horizontal position as opposed to the vertical position shown in Figure 4-3. An ion chamber connected to the incoming beam pipe (4) measures the intensity of the incoming beam, I_0.

In accordance with the procedure described in Section 2-2, calibration of the image plate was performed with the Fit2D software using diffracted rings from the same standard Si powder (NIST, Standard Reference Material 640a) used also as an internal standard (see Appendix B and [52]). The calibration simplifies the analysis by correcting for tilt misalignment (here -0.4^o) of the image plate with respect to the plane perpendicular to the beam. The calibration can also be used to externally calibrate the image plate, but it was not used for that purpose here.* The results of the calibration placed the beam center at 1720.6 pixels from the left of the image and 1713.5 pixels from

* An external calibration is unimportant since the Si was also used as an internal standard and the strains derived from a difference in lattice spacings rather than absolute lattice spacings are reported (for details see discussion Section 2-2).

the top of the image. The images were converted as "radial" scan types using 120 azimuthal (η) bins and 1700 radial (2θ) bins. The following conversion parameters were taken from the Si calibration: a sample to detector distance of 1111 mm, a wavelength of 0.1897 Å, a rotation angle of -48.68^{o}, detector tilt angle of -0.41^{o}, starting azimuth (η) angle of 0.0^{o}, end azimuth (η) angle of 360.0^{o}, inner radial limit of 0.0 pixels, outer radial limit of 1700.0 pixels, and no intensity conservation was selected since the geometrical correction and the polarization correction were used [52].

4-3. *Mechanical Loading*

Uniaxial tension was applied to each composite sample using a custom-built aluminum load frame. A high-strength epoxy fixed brass tabs to the grip region of the composite. Turning a ½ inch threaded nut applied load to the composite. The nut was threaded onto a shaft connected to the sample grip with a pin. Since the grip was free to rotate at the pin, it provided a simple method to reduce off-axis loading on the composite. Off-axis loading promotes bending in the sample and complicates the intended stress state of the composite.

Load was applied in constant displacement steps; therefore, the stress was not constant with time. Upon termination of displacement, the stress decayed from a maximum initial value. When the applied stress settled, the X-ray measurements were performed. The settling time depends on the rigidity of the system. The observed settling was primarily due to deformation in the grip assembly. An example constant displacement step is shown in Figure 4-6. The composite exhibits macroscopic elastic behavior over the strain range shown. Thus the strain drop observed by the gage is associated with a load drop observed in the load cell.

Two loading cycles were performed on each sample analyzed for bulk strains. The first cycle went to a lesser applied load than the second. For the first composite, the maximum applied stress of the first cycle was 790 MPa, but the sample settled to 660 MPa for the strain measurements. The maximum applied stress of the second cycle did not exceed 780 MPa due to failure in the grips. The grips were reinforced for the second composite sample both to reduce the settling time between loads and increase the maximum achievable load. The maximum applied stresses for the second composite

were 400 MPa and 900 MPa for the first and second cycles, respectively. XRD strain measurements were taken in small stress intervals ranging from 10 to 30 MPa per step. As depicted in Figure 4-6, the load intervals were not kept constant in load since the frame was designed to maintain displacement (not load) over time. As discussed in Section 2-1, this required constant monitoring of the load and applied strain using the software described in Appendix A.

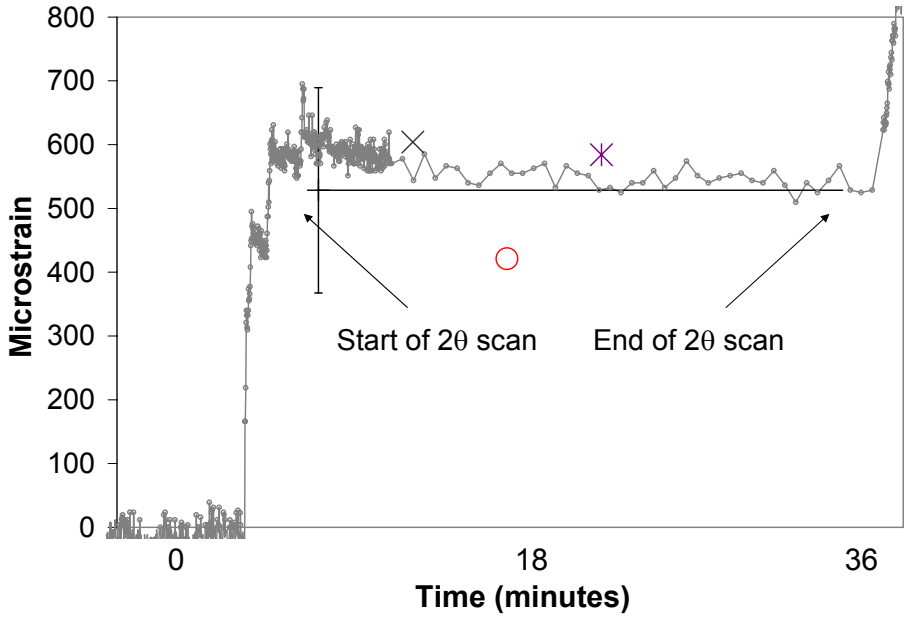

Figure 4-6 The strain gage (small circles with a connecting line) reveals drift of strain with time associated with the relaxation of load from a typical constant displacement load step. The strain in the matrix with its associated error given by the least squares refinement is shown by the flat line. Information from the entire 2θ scan (marked by arrows) is included in the refinement. The strains given by the Ti (11$\cdot$0) and Ti (10$\cdot$2) is given by the "x" and the "$*$," respectively. These along with the strain from the SiC (220) peak, a "o," are shown at the position the peaks occur in time.

4-4. *Bulk Residual Strains in the Composite*

The initial bulk longitudinal* residual strains in the laminate composite are shown in Table 4-1. Before loading, the fibers exhibit an average longitudinal compression of –1500 με due to thermal residual strains. The matrix balances this with an average tensile residual strain of +2200 με (obtained from the Rietveld analysis of the α-Ti phase). The reference *d* spacings for these residual strain measurements were taken from strain-free specimens of each phase. The systematic errors were compensated for by subtracting the "false" strain given by the internal standard. The preparation of the references is described along with other residual strains measurements for this composite in Section 5-2. Based on these strains, the FEM (Section 3-1) predicts average longitudinal stresses of –740 MPa and +350 MPa in the fibers and the matrix, respectively.

Table 4-1 Bulk residual axial strains in the Ti-SiC composite (from Figure 4-7).

Phase	**β-SiC (220)**	**α-Ti (Rietveld)**	**α-Ti (10·2)**	**α-Ti (11·0)**
***Initial* Residual Strain (x10^{-6})**	–1530 (±70)	+2200 (±150)	+1670 (±20)	+2890 (±20)

Employing the data for CTEs given in ref. [54], these thermal residual stress/strain results suggest an effective stress-free temperature of 550°C. This means, during cooling from the processing temperature, the thermal residual stresses/strains were effectively generated starting around 550°C. One must be cautious about the accuracy of this

*Here *longitudinal* and *axial* are considered synonymous since the axis of the fibers is in the longitudinal direction of the composite. This direction is also synonymous with the ε_{11}, ε_{xx}, 1, ξ, and *x* directions.

temperature as its value depends to a large extent on the accuracy of CTE data and the assumption of only elastic and plastic deformation in the matrix (i.e., any creep during cooling is ignored).

The fiber strains were based on measurements from the (220) reflection of β-SiC, which is a cubic phase. The choice to use only one reflection resulted from the high texture and small grain size (50-100 nm [78]) found in the fibers. Few SiC reflections were observed in the diffraction patterns, and among those, only (220) yielded good statistics. The literature values for this system confirm the observed thermal residual strains in the fibers. Withers and Clarke [55] and Choo *et al*. [69] used neutron diffraction and quote the same residual strain value for the SiC fibers in the longitudinal direction as was observed in this composite. The former used the (220) reflection as well, but the latter performed Rietveld analysis on β-SiC. In addition, Rangaswamy *et al*. [54] obtained a similar value (about –1300 με) using the same reflection. In sum, the (220) reflection of β-SiC yields representative values for the bulk strain state of the fibers. This can also be seen in Figure 4-7 where the strains along (220) follow closely the FEM predictions for the fibers.

The Ti-6Al-4V matrix exhibits significant elastic and plastic anisotropy. The initial thermal residual strains are seen to vary appreciably when plane-specific strains from α-Ti and the Rietveld "average" are compared (Table 4-1). (Note that the effect of the minority phase in the matrix (β-Ti) in the preceding and following analyses has been neglected due to its small percentage (less than 10 vol.%) [69].) Similar results were also observed by other researchers. For instance, Choo *et al*. [69] obtained +2600 με for the average axial strain in α-Ti from Rietveld analysis. In addition, their plane-specific

residual strains are similar to those shown in Table 4-1. The residual thermal strain anisotropy in α-Ti is due to anisotropy in its CTE (e.g., the CTE of the basal plane is higher than that of the prism planes) as well as its plastic anisotropy [69]. The latter would manifest itself in terms of variations in susceptibility to plastic deformation during cooling to relieve thermal stresses. As a result, plane-specific residual strains would be relaxed to varying degrees along prism planes in comparison with the basal planes.

4-5. *Bulk Applied Strains*

Application of tensile stress provided additional information about the plasticity in the matrix. Figure 4-7 shows the evolution of elastic lattice strains in the matrix and fibers, obtained from XRD data, during a loading/unloading cycle as well as the overall composite behavior, obtained through the strain gage. Residual strains from Table 4-1 are also included in Figure 4-7. From the strain gage, the surface of the composite shows linear elastic behavior up to 750 MPa applied stress (see also Figure 4-8). This is in agreement with the material data collected at 3M Corp. [73]. The composite's Young's modulus was 216 GPa, a value that compares well with the rule-of-mixtures prediction of 211 GPa and the nominal value provided by the manufacturer, 207 GPa [73].

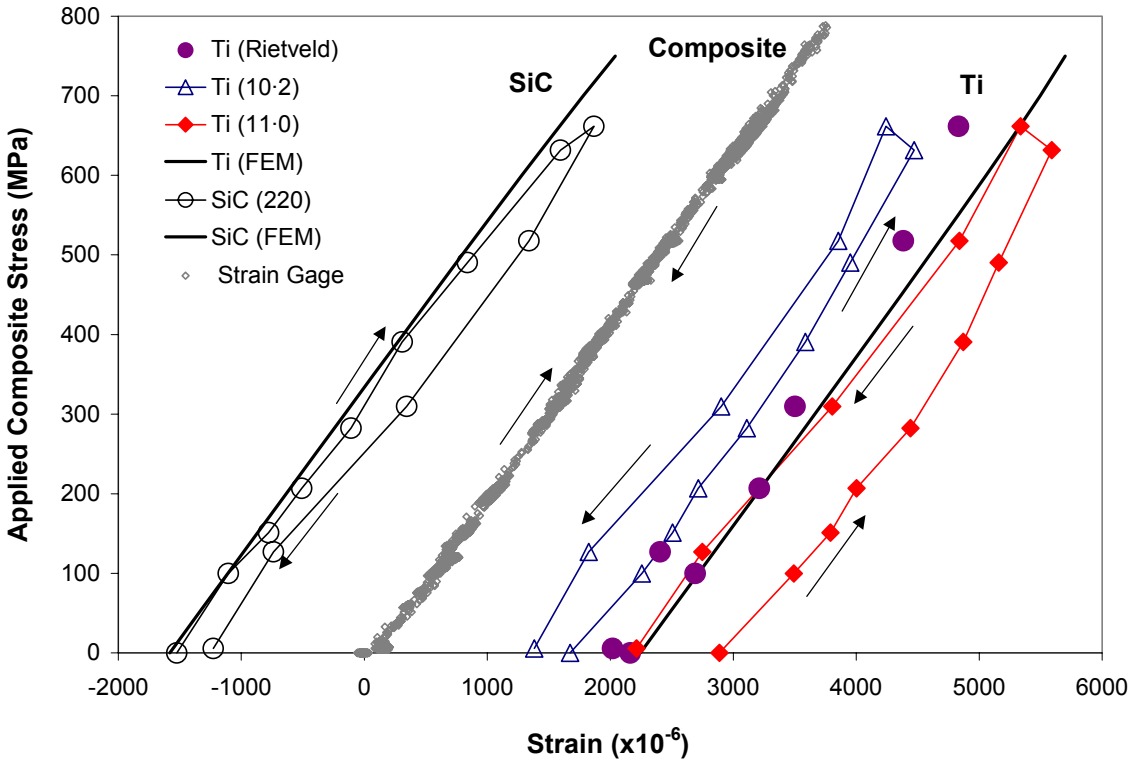

Figure 4-7 Comparison of experimental strains from bulk with FEM predictions of applied composite stress vs. average elastic axial strains in the first undamaged Ti-SiC composite during a loading/unloading cycle. Strain gage values are shown together with lattice strains in the Ti (10·2), Ti (11·0) and SiC (220) reflections obtained from diffraction. Thermal residual strains are included (see Table 4-1). Note that due to load drifts not every stress level could yield suitable data for Rietveld refinement.

When phase-specific lattice strains were studied, additional information about the mechanical behavior of the constituents was obtained. Single peak fits to the XRD patterns showed that, as the composite was loaded up to 500 MPa, the fibers and matrix co-deformed linearly (Figure 4-7). At higher stresses, the fibers began to strain more than the matrix at the same applied stress. This is a clear signal of load transfer to the fibers and implies yielding in the matrix. Unfortunately, time constraints during the initial XRD runs prevented the application of many stress levels to more precisely determine the *in situ* yield point of the matrix. A further complication was the load drift

due to deformation at the grips. This drift resulted in relaxation of applied stresses and led to lower stress levels during diffraction measurements than those initially applied (Figure 4-6). For example, although the composite was loaded to 780 MPa, the average stress during diffraction data collection was 660 MPa (Figure 4-7). This means the deviation from the linear curve in the lattice strains shown in Figure 4-7 resulted from yielding in the matrix between 650 and 780 MPa applied composite stress.

The *in situ* matrix yielding is expected to commence as a thin layer around the fibers (Figure 3-1 (d)). Since X rays sampled the entire cross section, matrix yielding is not realized until a significant plastic layer forms. The measured strains then confirm the FEM prediction that "global" yielding is not apparent until at least 600 MPa applied stress (Section 3-1 and Figure 4-7). The resulting change in residual strain will be presented with the next section in Table 4-2.

Similar behavior was seen in the second composite specimen examined with the image plate. Since reinforced grips were used, greater stresses were achieved and the load drift was diminished. The first cycle to 400 MPa showed primarily elastic strain. The strains in the second cycle to higher applied stress revealed yielding in the matrix. The attached strain gage shows slight global plasticity occurred in the composite after 750 MPa applied stress (Figure 4-8). The change in residual strain upon unloading also confirms that local plastic deformation occurred in the matrix (Figure 4-9 and Figure 4-10).

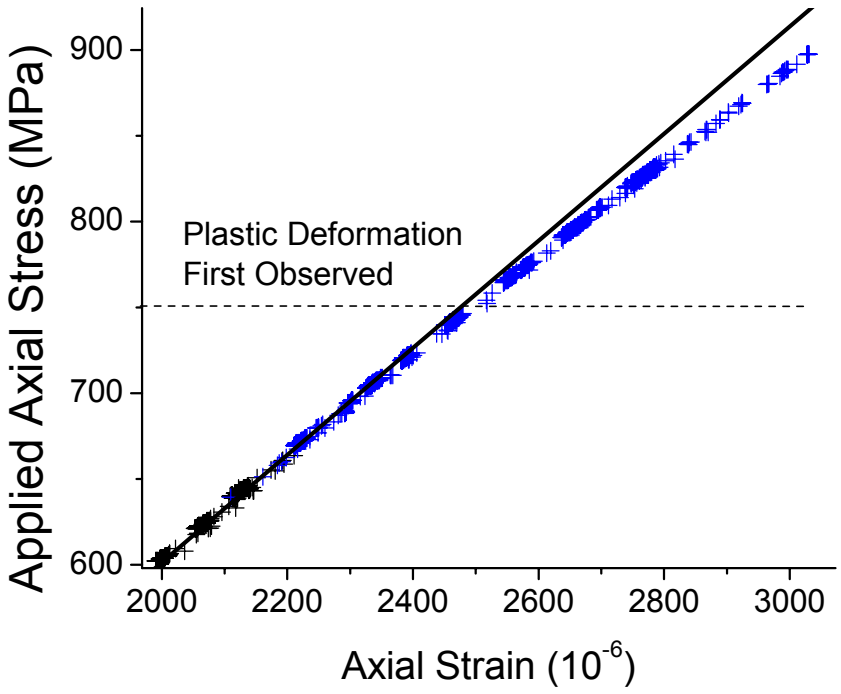

Figure 4-8 The macroscopic stress vs. strain in the first loading cycle of the second undamaged composite along the fiber direction according to strain gage data (symbols). Deformation in the composite was elastic up to at least 700 MPa with very little plastic deformation even after 800 MPa. A line from a linear regression fit to the elastic portion of the curve is plotted over the data points to help illuminate the slight deviation from linearity in the strains caused by plastic deformation.

An acceptable strain-free reference was not available for the image plate measurements directly, so the measurements made using the Rietveld refinements on the Ti strain-free reference were used for the matrix, and the Powder Diffraction File (ICDD,* PDF# 74-2307) database values for SiC were used for the fibers. Though the absolute residual strains will not be exact, this has no adverse effect on the accuracy of observed changes in residual or applied strain (i.e., the residual strains are limited by the accuracy of d_0, but the relative strains (total strain minus the residual strain) will remain

*International Centre for Diffraction Data, 12 Campus Boulevard, Newtown Square, PA 19073-3273

accurate [79]). Since the true residual strains were not available, for comparison with the FEM predictions, the residual strains in the second composite were assumed to equal the predicted residual strains from the model fit to the first composite. In addition, assuming the composites have the same residual strains is valid since the samples come from the same stock.

From the nature of the analysis on the second composite, strain information in the transverse direction is available simultaneously with the longitudinal direction. The strains in the transverse direction are predicted to locally vary more than in the longitudinal direction. This is due to the three-dimensional evolution of strains in the composite (Section 3-1). This local strain variation produces an associated variation of the peak center in 2θ at constant η for a range of η near 90^o, the transverse direction.

In spite of this strain broadening in the transverse direction, which increases error in the measured strains,* the bulk averaged transverse strain adds significant insight to the behavior of the composite. As the stress increases in the composite, the strains are seen to linearly increase in the fiber and matrix up to 500 MPa. Beyond this applied stress, the transverse strains increase and decrease nonlinearly signaling anisotropic plastic deformation (Figure 4-9 and Figure 4-10 (b)).

This nonlinear behavior should not be confused with the true bulk behavior of the composite. It is an artifact of the analysis procedure. When a grain begins to deform

*The analytical errors are smallest for the fiber axial strains (ε^f_{11}) and largest for the matrix shear strains (ε^m_{12}). In the fiber, the <111> texture for (220) weakened the reflection near $\eta = 90^o$ and 270^o. The lower intensity increased the error for ε^f_{22} and ε^f_{12}. In the matrix, graininess increases the error in average strain compared to the fiber. In addition strain broadening in the transverse direction associated with the range of strains in that direction increases the error of ε^m_{22} and ε^m_{12} compared to ε^m_{11} (see Figure 2-6 and error bars in Figure 4-9 and Figure 4-10).

plastically, its effective modulus decreases forcing neighboring grains to carry the remaining load. Since many grains are included in the X-ray average elastic strain, some of these neighboring "over stressed" grains contribute to the diffracted intensity increasing the measured elastic strain. The larger grain size in the matrix limits the number of grains contributing to each diffraction ring. Therefore, with the increased potential for variation in strain among the matrix grains with increasing load, it is likely that a few grains will be in a more optimal orientation for diffraction than the majority of the remaining grains. If some of these optimally oriented grains are in a local neighborhood that does not represent the bulk behavior of the composite, it may significantly perturb the results of the analysis with abnormally large (or small) changes in strain. This nonlinear effect is most pronounced in the transverse direction where the strains naturally vary over the irritated area to a much greater degree than in the axial direction. While this effect may encumber a modulus estimate from the transverse strains at high stress, it does provide evidence of early yielding in the matrix not observed with more conventional methods such as the strain gage analysis.

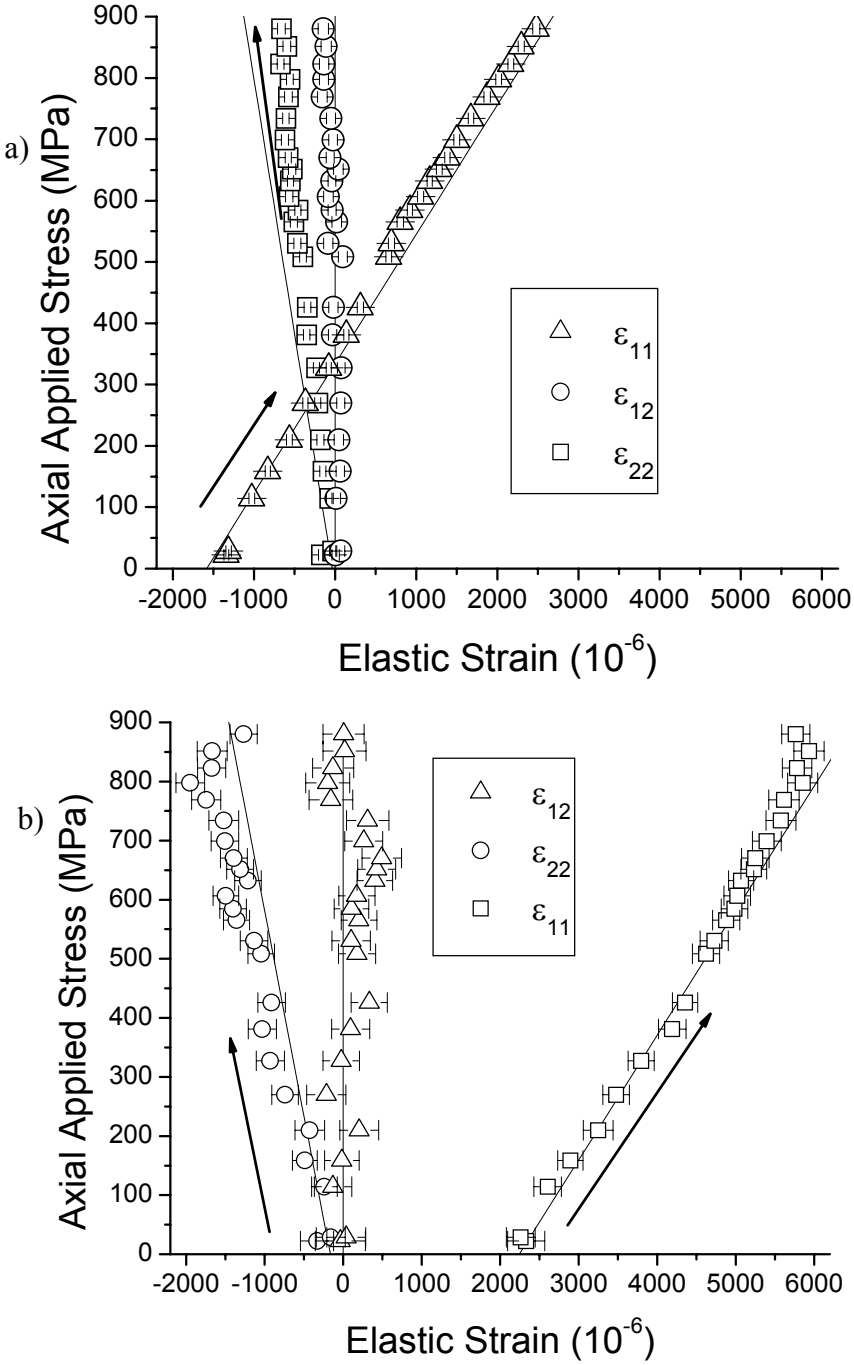

Figure 4-9 Elastic bulk strains in the fiber (a) and matrix (b) for increasing applied tensile stress in the second cycle (symbols) on the second undamaged composite. As before, the stress is applied along the fiber axial direction (axis 1). The FEM prediction for the loading cycle in the composite is also shown (lines). As in Figure 4-7 there is good agreement with the model up to the higher stresses. The deviation near 800 MPa signals the onset of global plastic strain in the matrix. An early onset of plasticity is observed in the transverse (ε_{22}) direction where individual grains naturally show larger variations in strain (see text). (Strains are taken from the matrix (10$\cdot$2) diffraction ring and the fiber (220) diffraction ring.)

As the applied stress is increased on the composite, the matrix strains begin to change nonlinearly in the axial direction. This deceleration in strain is associated with plastic strain in the matrix. Since plastic strain is attributed to flow by dislocation motion and not expansion of the lattice, the diffraction elastic strain can not continue to increase with increasing stress. This yielding behavior is realized near 700 MPa in the axial direction, the same stress predicted by the FEM, at least 50 MPa earlier than it is realized with the composite strains from the gage (Figure 4-8).

One advantage of the image plate over the point detector includes improved detection of matrix yielding. The nonlinear behavior observed in the transverse direction is more pronounced than the axial direction. Thus matrix nonlinear behavior, which before 700 MPa was within the statistical error of the axial strains, is more significant in the transverse strains. The nonlinear strain behavior in the transverse direction is observed as early as 500 MPa with a significant deviation by 600 MPa. This observation is consistent with a composite which initially yields to a small degree in the matrix along the transverse direction near 500 MPa, yielding continues to increase spreading to an increasing number of grains until it is initially observed in the axial direction near 700 MPa. Finally the matrix yielding becomes significant enough to affect the strain gage reading, 250 MPa after it was first observed, near 750 MPa.

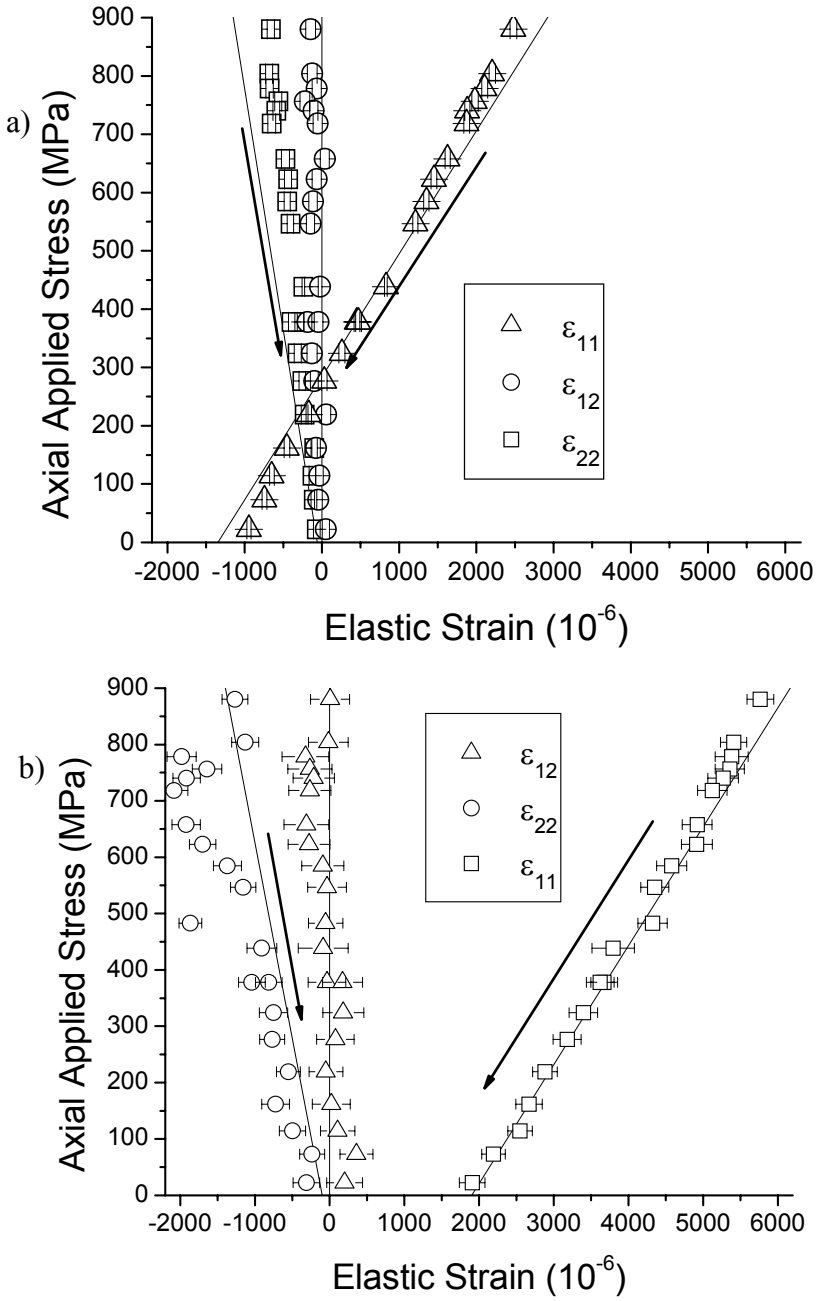

Figure 4-10 Strains during the release of applied tensile stress in the second undamaged composite. The arrows show the direction of unloading. The fibers (a) show an overall linear behavior with very little average shear strain over the range of applied stress. However, the matrix (b) appears to deviate from linear behavior particularly in the transverse (ε_{22}) and the shear (ε_{12}) directions.

Consideration for the intrinsic range of strains in the transverse direction must be included with these observations as the strain equation (2-3) and the analysis method was not optimized for quantification of these variations. A broader range of strains contributes to a more scattered position of the diffraction ring in the transverse direction (strain broadening, for example see Figure 2-6). Since there is a greater range of strains in this direction some grains will be closer to a yield point than others. Whereas in the axial direction the strains are more uniform and the grains approach their yield stress together. This becomes increasingly significant with load as XRD analysis intrinsically weights grains unevenly which will tend to highlight grain-specific behavior particularly in the transverse direction since only a portion of the available grains are included for calculating the mean of the broad range. The jogs in the transverse strains of Figure 4-9 and Figure 4-10 are likely due to a small number of grains or sub-grains rotating (or translating) slightly in and out of favorable orientation to diffraction which drastically changes the intensity around the transverse portions of the diffracted ring for small η. The solution to Eq. (2-3) changes for the transverse direction when these intensities change. Again, since a broad range of strains is present in this direction, loosing intensity for one outlier could noticeably change the result. A change which is consistent with the onset of yielding in the matrix though the magnitude observed may not fairly represent the mean strain in the composite.

4-6. *Bulk Residual Strain Evolution*

The outcome of matrix yielding visible in Figure 4-7, Figure 4-9, and Figure 4-10, is quantified in Table 4-2 as the change of the residual strains following unloading. Specifically, in the first composite—loaded to 790 MPa—new tensile strains (+300 με) were generated in the fibers and new compressive strains (about –200 με using the Rietveld analysis) were added to the matrix after unloading. The character of the yielding-induced residual strains is typical for a MMC in which the matrix yields and transfers load to the stiffer fibers [80, 55]. Assuming a simple one-dimensional stress model, the change in residual strains when fully unloaded for the first composite correspond to a 120 MPa increase in the fiber residual stress and a 25 MPa decrease in the matrix residual stress. Compared to other loading experiments in this MMC system, these values indicate small scale yielding in the matrix. For instance, Withers and Clarke [55] measured residual strain changes of +1000 με and –1800 με in fibers and matrix, respectively.

Table 4-2 Residual axial strain (10^{-6}) evolution in damage free Ti-SiC composites averaged over all fiber and matrix regions in the beam. The first three rows correspond to measurements from the first composite examined with the point detector. The last two rows row corresponds to values taken from the second composite using the image plate. The second composite was also taken to a greater applied tensile stress.

	Phase	**β-SiC (220)**	**α-Ti (Rietveld)**	**α-Ti (10·2)**	**α-Ti (11·0)**
1st Composite	***Initial* Residual Strain**	−1530 (±70)	+2200 (±150)	+1670 (±20)	+2890 (±20)
	***Final* Residual Strain**	−1230 (±70)	+2000 (±130)	+1400 (±20)	+2200 (±10)
	***Change* in Residual Strain After 790 MPa Applied Stress**	300 (±70)	-200 (±140)	-270 (±20)	-690 (±15)
2nd Composite	***Change* in Residual Strain After 850 MPa Applied Stress**	400 (±28)	NA	-420 (±172)	NA
	***Change* in Residual Strain After 400 MPa Applied Stress**	5 (±33)	NA	-26 (±182)	NA

Though a small change in the "average" matrix axial residual strains of the first composite sample (provided by Rietveld) was observed after the plastic deformation, significant plastic anisotropy was seen in the matrix (Figure 4-7 and Table 4-2). This is expected given the hexagonal crystal structure of α-Ti. Of the two crystal planes exhibited in Figure 4-7, (10·2) approaches the Rietveld average in terms of its susceptibility to plastic deformation. Its effective elastic constant was similar to that given by Rietveld as well—the unloading gradient of (10·2) strains was measured as 217 GPa versus 221 GPa from Rietveld. In comparison, (11·0) had an unloading gradient of 203 GPa. In addition, (10·2) is near both the (220) reflection of β-SiC and the (220)

reflection of Si (used as internal standard) in *d* spacing, reducing the data collection times. Thus the $(10\bar{2})$ was also examined using the image plate analysis method. The change in residual strain for the second composite loaded to 850 MPa is also given in Table 4-2. The change in residual strain was in accordance with those seen in the first composite. Furthermore, since a change in residual strain upon unloading signals yielding in the matrix, the lack of change in residual strain for the cycle to 400 MPa confirms the absence of matrix yielding below this stress as was concluded in the previous section.

4-7. *Conclusions on the Bulk Laminate Properties*

Using two X-ray diffraction methods, the phase-specific *in situ* residual and applied strains in a metal matrix composite were investigated. Of the two methods, the use of an image plate proved most valuable for the identification of global yielding in the matrix. Plastic yielding is revealed in nonlinear lattice strains usually dependent on the crystallographic direction analyzed. As was shown here, since the two-dimensional strain tensor could be observed at each load, the characteristic nonlinear behavior of yielding could be observed where it first occurred, the transverse direction. However, both the point detector and the image plate methods provide elastic strains comparable to a three-dimensional FEM (Section 3-1).

Due to the CTE mismatch, thermal residual stresses of −740 MPa in the fibers and +350 MPa in the matrix exist along the fiber axes. Although, using conventional mechanical testing, the global yielding of the Ti-SiC composite was not detected until 750 MPa applied stress; XRD strains revealed that measurable local yielding occurs as early as 500 MPa. These strains were due to growth of the yield zone around the fiber as predicted by FEM (Section 3-1). In the residual stresses and under the applied tensile load, plastic anisotropy was observed in the matrix. It provides a source for the grain-to-grain strain variation in the composite (Section 5).

From the applied strain results obtained here, the α-Ti (10$\cdot$2) reflection shows behavior representative of the matrix average obtained from Rietveld. The α-Ti (10$\cdot$2) also showed similar sensitivity to plasticity-induced residual strains as the matrix average. Thus, the same reflection was used in the microdiffraction study described below.

5. Microscale Deformation of Ti-SiC Composites

The bulk deformation information from the analysis above provided valuable insight concerning the mechanical behavior of the composite. However, damage such as a fiber break will not necessarily occur uniformly throughout the composite, making the bulk analysis less useful in discerning the micromechanical behavior of the composite. What is needed to fully understand the micromechanics of the composite, particularly near fiber breaks, is spatially resolved strain information. Since damage in the composite typically results in fiber fracture, the micromechanical dimension of interest according to the MSSL model (Section 3-2.1) is the fiber diameter. In order to obtain strains at this scale, XRD was used to build maps of the elastic strains near fiber breaks in the composite. While the fibers are well suited to the micro-analysis technique, the matrix grain size is on the order of one fifth of the fiber diameter. This presented a challenge, as only a few grains would contribute to the measured stain at the dimensions of interest. As will be shown, this challenge was overcome through the use of high-energy two-dimensional micro X-ray diffraction (HEμXRD^2). The observed strains are presented in this section with a comparison to the predicted strain profiles in Section 5-7. The section begins with the introduction of damage into the composite.

5-1. *Controlled Damage in Ti-SiC Composites*

In order to examine a region of interest ideal for application of the MSSL mechanics model [34], the presence of at least one damaged fiber was required. Finding naturally damaged fibers *in situ* during loading is a strong capability of X-ray imaging such as microtopography or tomography; however, in order to isolate the effects of the damaged

fiber, it is also desirable to find a broken fiber that is surrounded by a uniform region of damage free matrix and fibers. Lastly the damage must be located far from the grips and sample edge in order to eliminate spurious effects from these regions of non-uniform stress. Others have attempted the examination of SiC fiber strains using X-rays in a composite processed with free fiber ends in a Ti matrix [81]. Though an interesting study particularly for its use of radiography to identify fiber breaks, the local stress state in such a composite does not directly relate to the problems of interest for the engineering and modeling community since load transfer from broken to intact fibers could not be investigated. In addition, the matrix strains between fibers were overlooked in that study.

For this analysis, two methods were used to produce controlled damage in the continuous fiber Ti-SiC composite. In the first method, matrix at the center of the gage length was etched (using 50% hydrofluoric acid), exposing a section of SiC fibers. In the center of the exposed region, one fiber was damaged by compressing a sharp bit into the fiber perpendicular to the fiber axis. The matrix was left intact around and behind the roughly 0.6 x 0.2 mm^2 exposed region or "damage area" (Figure 5-1). The fibers examined were labeled -2 through 2 with 0 being the initially broken fiber. The specimen dimensions were: thickness, t = 0.20 mm, gage length, L = 26.00 mm, and gage width, W = 10.25 mm (Figure 5-2). As with the bulk composite analysis, a 120 ohm strain gage was attached to measure the applied macroscopic strain at the surface in the longitudinal direction, parallel to the fibers (Figure 5-2).

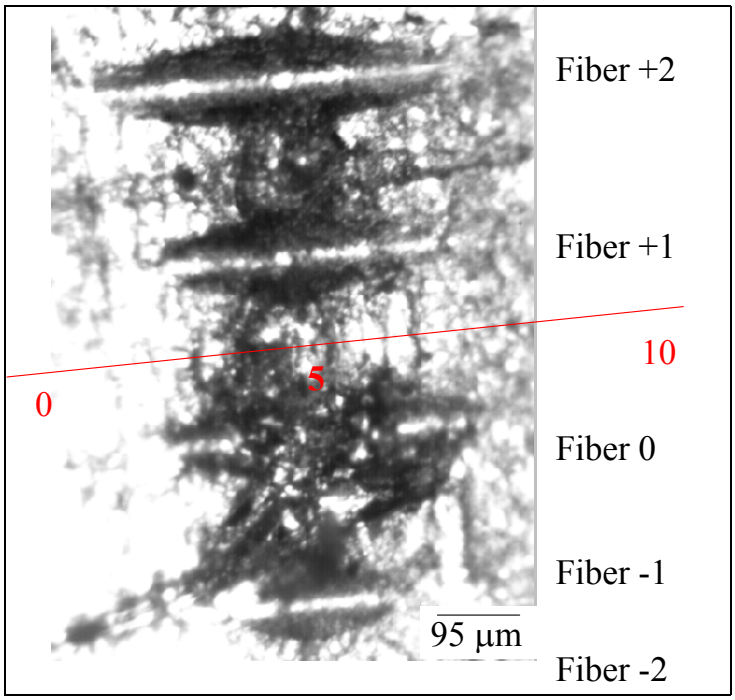

Figure 5-1 Optical micrograph illustrating the exposed fibers around the damage zone. The red numbered line is parallel to the fibers with the red numbers displaying the approximate scale for some axial positions where strains were measured.

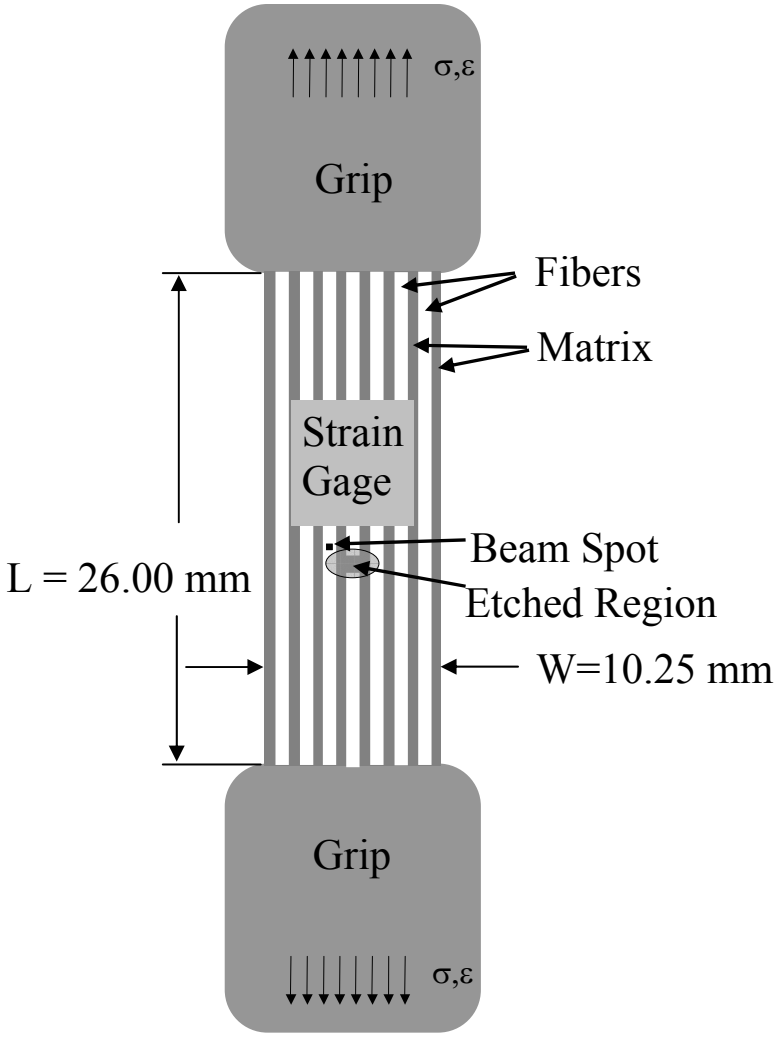

Figure 5-2 Schematic showing the damaged sample geometry used in the XRD experiments. The composite thickness was 0.2 mm. Fibers positions are represented by white lines within a gray matrix. The region etched is marked by an oval below the strain gage (for illustration only – not to scale).

While the first sample afforded a good comparison with the model, uncertainty associated with the geometry of the damage zone was alleviated by a second sample. In the latter, a small hole was cut by plunging an EDM wire into the center of the composite. Similar to the EDM technique first attempted on the macroscopically analyzed sample, oxidation of the Ti surface was avoided by sandwiching the composite between two Al strips.

The dimensions of the hole affect the stress concentration on the surrounding fibers. Accurate measurement of the hole size and initially broken components is critical for unambiguous application of micromechanical models. Using images from an SEM, the hole measured 290 μm across cutting one fiber, labeled *D*, and the matrix between two fibers, fibers *D* and *E*. The neighboring fiber, labeled *E*, and adjoining matrix region were also partially cut by the EDM wire (see Figure 5-3). The length of the hole along the fiber was measured to 240 μm. The opening of the hole in the fiber axial direction tapers towards zero as it approaches fiber *E*. The average length along the cut matrix region was measured to 226 μm.

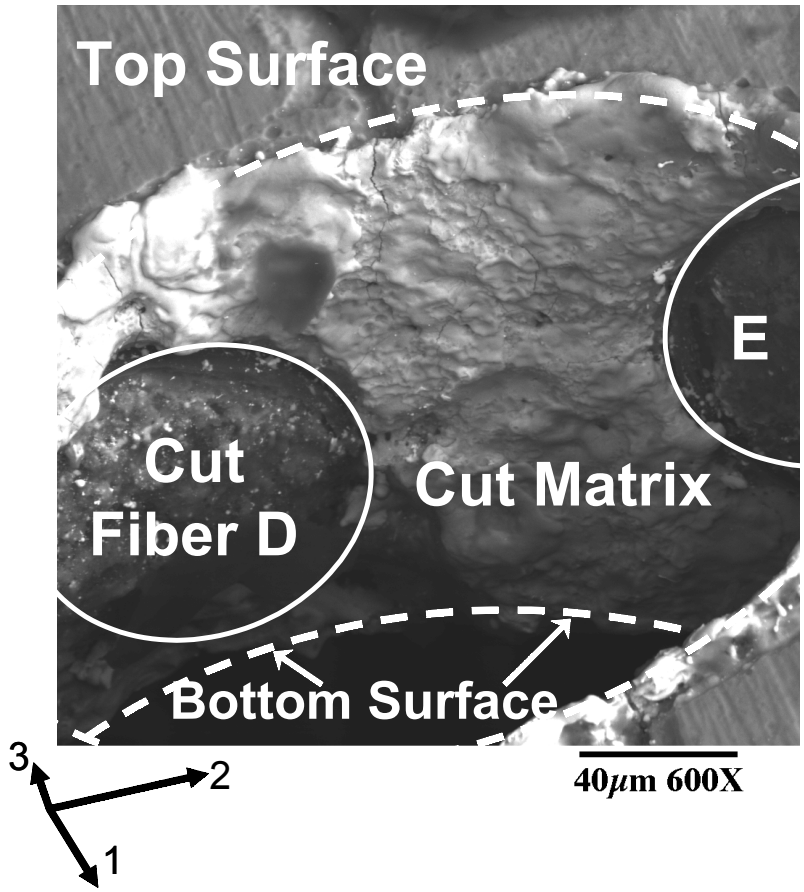

Figure 5-3 An SEM image at a 45^{o} tilt angle of the hole cut by EDM in the second composite. The hole cut completely through one fiber which was later assigned the label *D*. Beside it is fiber *E* which was partially cut. The matrix between these fibers is obviously cut as well as some of the matrix adjacent to *D*, the completely cut fiber.

5-2. *Additional Residual Strain Measurements in Ti-SiC Composites*

The following describes some additional experiments focused on the residual strain in the composite. A comparison of the results from the different techniques is presented along with some of the difficulties in obtaining accurate residual strains from this composite system.

For an ideal measurement of residual stress particularly in a fiber composite, a strain-free reference is necessary. Though the chemical composition of a powder may be identical to the consolidated phase of interest, any one of a number of processing parameters may disturb the lattice parameter of the consolidated material making the powder a deceptive strain-free reference. In practice, simply obtaining a strain-free powder identical in composition to the phase of interested may also be difficult.

For the Ti-SiC composite system, a strain-free reference was obtained by etching a portion of the matrix away from the fibers. SiC is stable in the presence of aqueous HF and did not react with the etchant used to remove the matrix. Thus strain-free fibers, or more precisely, fibers whose residual strain state no longer depended on the matrix were easily attainable. Such a reference is preferred over the raw fibers since processing them into the composite potentially changes the structure of the fibers on a scale which would be measured by X rays (10 ppm).

A more tedious procedure of layer removal by etching was used to obtain the matrix strain-free reference. The matrix was slowly rinsed from one surface of the composite down to a depth exposing the radius of the fibers. As the matrix was removed, the

remaining composite curved away from the exposed fibers providing visual proof of the compressive residual strain state in the fibers and tensile residual strain state in the matrix. Finally, to completely remove the fibers from the matrix, one end of the remaining composite was immersed in etchant. With a portion of the interface etched away, the thermal residual stress provided enough force to separate the matrix from the fibers resulting in the matrix strain-free reference.

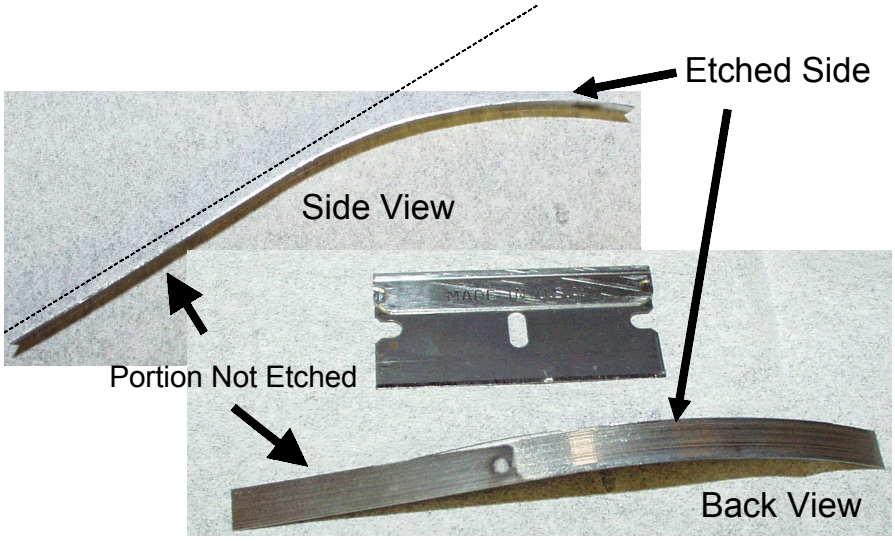

Figure 5-4 Two photographs of the etched composite during the process of making the strain-free reference (before the fibers were etched away from the matrix). The thermal residual strains are strikingly apparent from this image. Once the fibers were freed from the matrix both phases returned to their originally flat configuration. A razor blade is also shown to provide scale.

In some circumstances, a strain-free reference cannot be obtained. An option for measurement of the residual strain in these cases is the "*d* vs. $\sin^2\psi$" technique [17]. The technique requires measurements of the lattice spacing at one location over several sample angular orientations (defined as ψ whether the rotation is along θ or χ). For example, to obtain the values of $\sin^2\psi$ used here (0.051, 0.10, and 0.20), the sample was rotated in θ through the angles 13.05^o, 18.43^o, and 26.57^o away from the θ = "2θ" / 2

position (or standard $\alpha = 0^o$ position). The resulting lattice spacings are then used to solve the relevant form of the strain equation (for example, Eq. (5-1) below) and provide the residual strain (for more discussion see [17]).

This technique was used to measure the transverse residual strain in the matrix of the Ti-SiC composite. Three distinct $\sin^2\psi$ residual strain measurements were performed on sections of the Ti-matrix/SiC-fiber composite consisting of a single row of unidirectional fibers. First, a microdiffraction experiment that involved scanning the Ti matrix to identify individual grains reflecting at a given Bragg angle for several ψ tilts is presented. Then, two macrodiffraction experiments including a Cu radiation experiment conducted at Caltech and a through-thickness high-energy experiment performed at the Advanced Photon Source are compared to the microdiffraction measurements. The sampling volume involved the same grains in both macrodiffraction cases. The analysis illuminates the non-uniformity of residual strains in the composite, specifically in the transverse direction, and highlights the significance in averaging data from individual grain measurements.

5-2.1. "sin$^2\psi$" Experimental Procedure

"sin$^2\psi$" Specimen

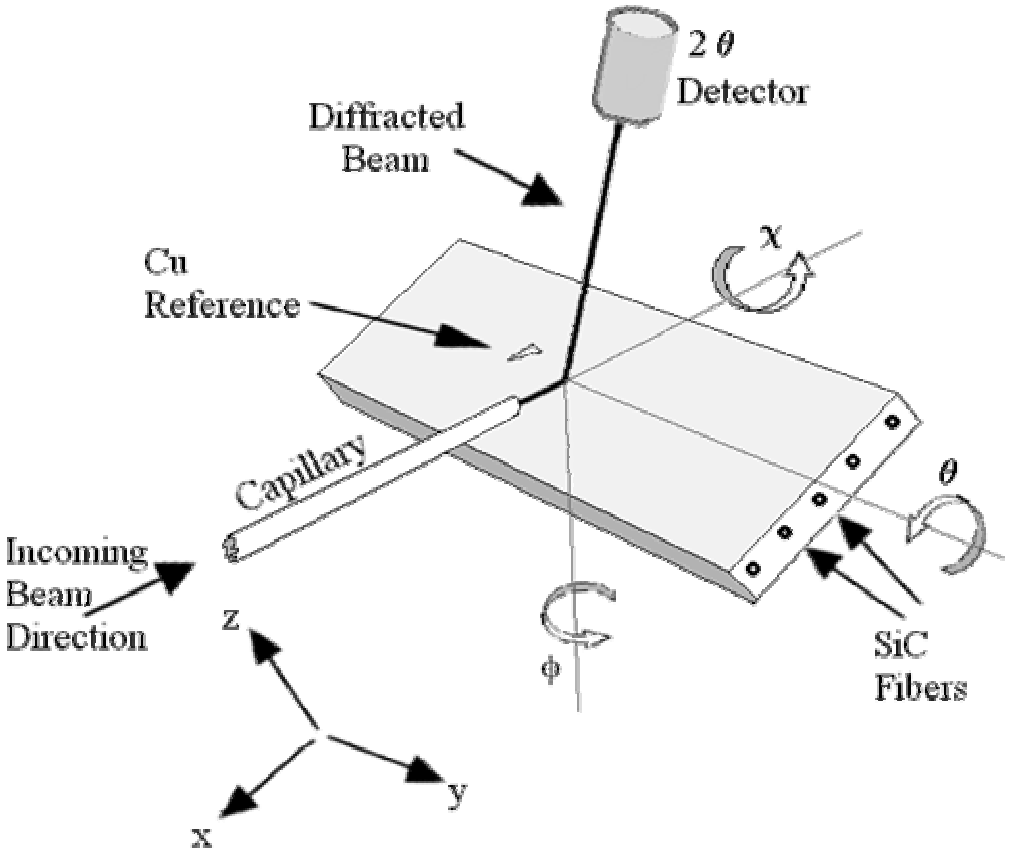

Figure 5-5 Diagram of the low-energy microdiffraction technique. 2θ is in the same direction as θ.

For the following measurements, a separate section of unidirectional laminate from the same Ti-SiC composite described earlier was examined. After cutting and mechanically polishing the sample in order to expose the fibers at each surface, the dimensions were 16 mm wide in the x^* direction and 38 mm long in the y direction (see directions in Figure 5-5). A triangular copper marker was placed near the region of

---

*As noted in the figure, the orientation of the x and y directions for the sin$^2\psi$ analysis are perpendicular to the directions used in the other analyses.

interest, which was used as the reference position for the observed grains. For this study, the region analyzed by X rays did not have exposed fibers. Its total thickness was 0.17 mm in the *z* direction.

Using the linear intercept technique, the average grain size of Ti was 29 μm ± 3.5 μm [82, 83]. Measurements were made at 40x and 20x magnification on an optical microscope. In the plane parallel to the axis of the fibers, 110 grains were averaged (the *x*, *y* plane in Figure 5-5). For the plane perpendicular to the fibers, too few grains were available to use the linear intercept technique.

"$\sin^2\psi$" *Micro*diffraction Procedure

The microdiffraction analysis was performed on the X-20 beamline of the National Synchrotron Light Source of the Brookhaven National Laboratory using an Ω goniometer. For this analysis, the energy of the X-rays was fixed at 9 keV providing good statistics for count times of approximately 1 second when using a 0.2^o receiving slit width and a microbeam capillary with a 0.3^o divergence in place [37]. The experiments were conducted at room temperature.

In a reflection orientation with the fibers running perpendicular to the beam, the sample was scanned in the plane parallel to the surface of the sample (Figure 5-5). Individual α-Ti grains with the $(20\bar{3})$ plane in a similar orientation were identified by their diffracted intensity around $2\theta = 88.6^o$. With an X-ray spot size on the surface of the sample approaching 10 μm in diameter, the grains were resolved as shown in Figure 5-6. Grains were selected for further analysis based on their relative diffracted intensities.

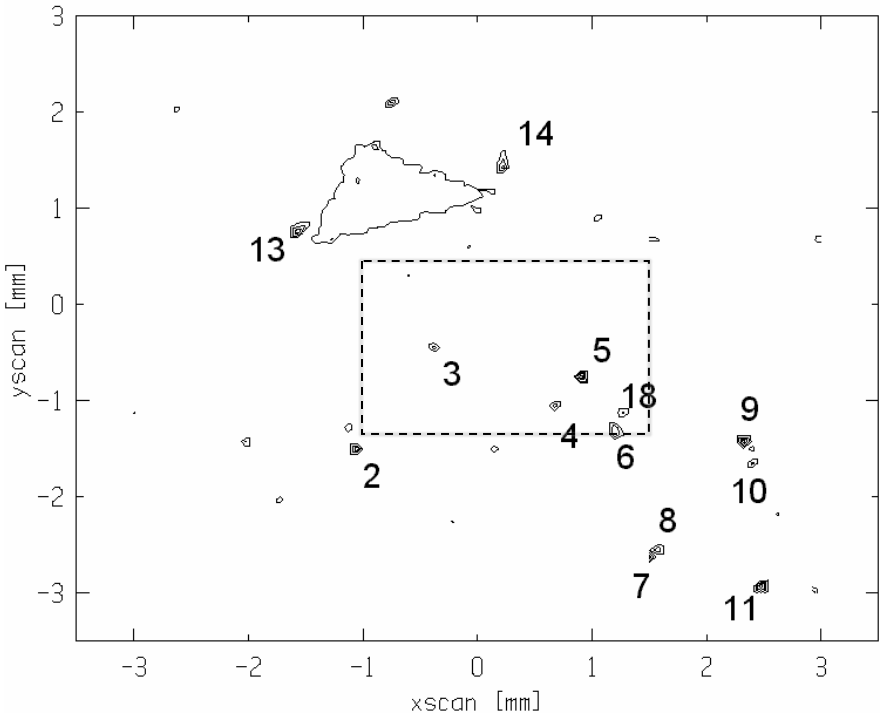

Figure 5-6 Contour plot of Ti (20·3) reflection from microdiffraction. The Cu (311) reflection, which is close in *d* to the Ti reflection, exposes the Cu marker as the rough triangle between grains 13 and 14. The rectangle in the center of the figure borders the region scanned at higher ψ's.

The coordinates of the numbered grains shown on Figure 5-6 were optimized first in *x*, then in *y* based on the maximum intensity of the diffracted peak while varying *x* and *y* independently. At least two iterations of a similar optimization procedure were performed for the θ and χ angles. Finally, *2*θ was varied while holding the sample fixed. A maximum in *2*θ was then calculated based on the full width at half maximum (FWHM) of a Gaussian curve fit to the peak. The receiving slit width for this measurement was 0.02 mm. The procedure was then repeated for $\sin^2\psi$ = 0.051, 0.10, and 0.20, respectively, on a total of 38 separate grains.

At 9 keV, the penetration depth ($G_{0.99}$, defined as the thickness that contributes 99% of the intensity diffracted in reflection at $\theta = 44.3^o$) was calculated to be 28 μm. For a

grain 29 μm across and a 36 mm^2 area, assuming square grains, the Lorentz factor predicts approximately 80 grains should reflect at $2\theta = 88.6^o$ [17]. As can be seen in Figure 5-6, approximately half that number of significant grains were observed for the 36 mm^2 area sampled at $\psi = 0^o$. Thus, half of the predicted number of grains contributed to the majority of the diffracted intensity.

"$\sin^2\psi$" *Macro*diffraction Using Low Energy X Rays

The same α-Ti reflection, $(20\bar{3})$, was again examined at Caltech on a Siemens D500 diffractometer using Cu radiation (8.04 keV, $G_{0.99}$ = 20 μm). The ψ tilts were performed at the same angles as in the microdiffraction procedure: 0.00^o, 13.00^o, 18.46^o, and 26.57^o. The area probed by the X-ray beam was approximately 2 mm in the *x* direction by 4 mm in the *y* direction at 0^o ψ with 0.3^o slits (Figure 5-5). To correct for potential alignment errors, a standard LaB_6 powder (NIST Reference Material 660) was simultaneously scanned in 2θ at the (411) reflection (d = 0.9798 Å). The Ti reflection was fit using a Gaussian profile function, and the LaB_6 (K_α and K_β) reflections were fit using Lorentzian profile functions. The d_{203} results are plotted on Figure 5-7.

$\sin^2\psi$ Macrodiffraction Using High Energy X Rays

The same sample was again analyzed in transmission using 25 keV X-ray radiation provided by the Advanced Photon Source (APS) at the SRI-CAT (Sector 1) beam line. For 25 keV X-rays, $G_{0.99}$ is 170 μm; therefore, the strain data obtained is a through-thickness exponentially weighted average. An area of 2 mm along the fiber direction for $\chi = 0^o$ by 1 mm perpendicular to the fiber direction was sampled. The area investigated intersects the area sampled by the low-energy microdiffraction $\sin^2\psi$ analysis. For this

procedure, ψ was taken to be in the χ direction instead of the θ direction (Figure 5-5). As in the other procedures, ϕ was not varied for this sample. The values of $\sin^2\psi$ examined were 0, 0.1, 0.5, and 0.702. The α-Ti (20·3) reflection position was determined using a Lorentzian profile function.

5-2.2. "$\sin^2\psi$" Results and Discussion

The results of the microdiffraction analysis were averaged for each ψ and are shown on Table 5-1. In the case of $\psi = 0^o$, two values are given. The first value is the average *d* spacing of all 13 grains analyzed at $\psi = 0^o$. The second value is the average of the five grains, 3 through 6 and 18, within the dashed line box on Figure 5-6. Also in Table 5-1 are the respective standard deviations in the *d*-spacing at each ψ. Some are almost half the proof strain limit (~0.2%) for ductile materials, with the largest measured variation between grains at 0.00318 Å for $\sin^2\psi = 0.10$.

Table 5-1 Averaged results of the *micro*diffraction analysis.

Number of Grains	*Sampled area (mm^2)*	$sin^2\psi$	d_{203} *(Å)*	*standard deviation*
13	36	0.000	0.98573	0.0844%
5	4.0	0.000	0.98602	0.0656%
9	3.6	0.051	0.98597	0.0736%
9	4.0	0.100	0.98570	0.0934%
7	3.6	0.200	0.98536	0.0567%

For the strain analyses calculated herein, the reference *d* spacing, d_o, value is taken as the value measured at $\psi = 0^o$. For $\phi = 0^o$ we have [17]

$$\frac{d_{\phi\psi} - d_o}{d_o} = \varepsilon_x \cdot \sin^2\psi + \varepsilon_z \cdot \cos^2\psi + \varepsilon_{xz} \cdot \sin(2 \cdot \psi) \qquad (5\text{-}1)$$

Using values predicted from a linear fit to the averaged values for the roughly 4 mm^2 area in Table 5-1 and solving Eqn. 5-1, the relative strain in the direction perpendicular to the fibers (ε_x) is –3500 με. In the case of the microdiffraction analysis performed at $\psi = 0^o$, the number of grains measured was significant enough to show strong variations in the measured *d* spacing throughout the 36 mm^2 area. These variations suggest large strain gradients. In order to localize averaging over significant transverse strain gradients, the $\sin^2\psi$ scans were performed on an approximately 4 mm^2 area of diffracting grains (the region bordered by the dashed line box in Figure 5-6). If the *d* spacing given by the entire 36 mm^2 region at 0^o ψ is instead used in the analysis, the result is -2400 με. This dependence on area exemplifies transverse strain gradients on the surface of the polished composite sample.

The *d* spacing values given in Table 5-1 are plotted in Figure 5-7 along with the values measured by the 8.04 keV macrodiffraction analysis as a function of $\sin^2\psi$. The error bars for the microbeam analysis represent the standard deviation for the grains averaged at that ψ. The error bars for the macrobeam analysis represent two times the standard deviation of the (411) LaB_6 reflection position measured simultaneously with the Ti (20$\cdot$3) reflection.

As can be seen from the graph, the slope of the macrodiffraction measurement agrees with the microdiffraction measurements within the error of each measurement. Using

values predicted from a linear fit to the average for the macrodiffraction data and Eq. (5-1), the predicted relative strain in the matrix is –3100 με in the *x* direction (here perpendicular to the fibers). Since, nominally, the same small number of grains was sampled in both analyses, a similar deviation in *d* spacing among grains is expected. For the macrodiffraction analysis, this deviation contributes to the broad peaks observed. Since the low-energy experiments were performed using the θ direction for ψ, at high ψ the spot size of the beam decreased. In addition, absorption of the diffracted radiation becomes increasingly significant with an increase in ψ. These changes account for some of the observed variation in intensity of the reflections with ψ.

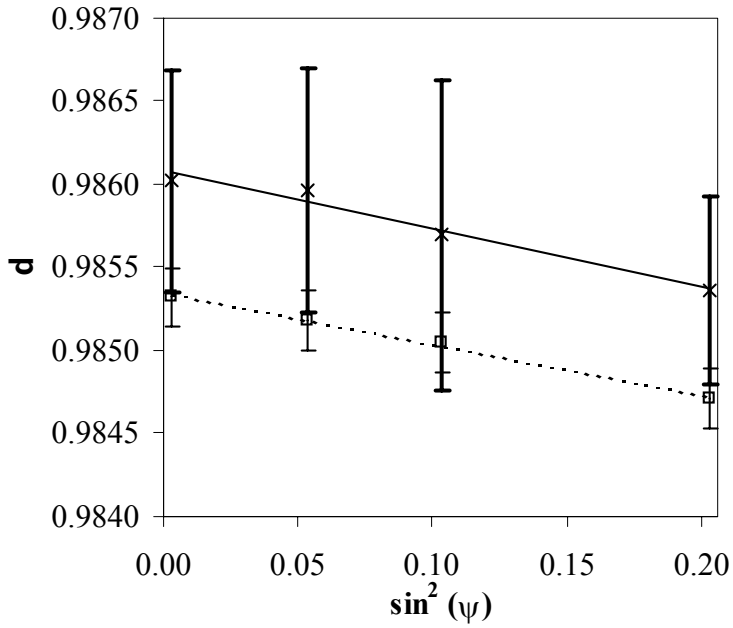

Figure 5-7 Comparison of the macrobeam, □, and microbeam, x, low-energy measurements.

The 25 keV data shows the matrix in transverse compression with ε_{xx} = -860 με. The high-energy transmission data also gives a negative slope (Table 5-2). In all three cases, similar areas of the sample were analyzed. However, as the 25 keV results originate from

transmission measurements, the entire depth of the sample was probed; thus, these results represent a larger set of grains than the previous analysis in reflection geometry.

Table 5-2 Comparison of slopes and residual strain values for each technique used.

Technique	**Slope of the "d vs. $\sin^2\psi$" curve (Å)**	**Residual strain in the transverse direction (10^{-6})**
Microdiffraction	-0.00346	-3500
Macrodiffraction	-0.00307	-3100
Transmission	-0.00085	-860
Transmission (using a strain-free standard)	NA	Average -560 Min. -3320 Max. 1760

Independent Cu K_α diffraction measurements of thick electrochemically polished Ti-6Al-4V-matrix/SiC (SCS-6)-fiber composites gave 174 με for the matrix residual strains in the transverse direction [54]. The difference in these results may be due to mechanical polishing or differences in the initial processing history, but the residual strain measurements using the strain-free standard also gave -560 με for the same composite system with a strong variation depending on position from the fiber (Section 5-4).

5-2.3. "$\sin^2\psi$" Conclusions

A model Ti-SiC composite was examined using three distinct X-ray techniques: low-energy microdiffraction (9 keV synchrotron radiation), low-energy macrodiffraction (Cu radiation), and high-energy macrodiffraction (25 keV synchrotron radiation). When considering similar sampling areas, the microdiffraction analysis verifies the same compressive strain state observed using the traditional macrodiffraction technique. This is not surprising since the same grains were observed in both cases. However, though the "*d* vs. $\sin^2\psi$" plot appears linear with similar slopes for the two low-energy reflection measurements, the strain measured in high-energy transmission is considerably different. This is also compounded with the large variation in strain between grains.

The difference in low-energy to high-energy data suggests a large strain gradient through the depth of the sample and likely a three-dimensional strain state making questionable the use of "*d* vs. $\sin^2\psi$" data for residual strain measurements in this system. These measurements were conducted observing lattice planes in the direction parallel to the fiber axis (transverse direction). Measurements using transmission and a true strain-free reference later confirmed the non-uniform strain state in this direction and a dependence on the proximity of the measurement to the fibers in the out-of-plane direction as is predicted by an FEM model (Sections 3-1, 4-4, and 5-4).

5-3. *Microbeam Diffraction Method*

The high intensity of synchrotron X-rays makes practical the generation of small beams that allow a detailed study of the co-deformation of phases in composites. While the microbeam method is similar to the macrobeam method described in Section 4-2, the addition of spatial resolution requires some procedures not covered there. A description of these additional procedures and the resulting data follows. These microdiffraction experiments were primarily done at the Advanced Photon Source (APS), but some surface measurements were also performed at the National Synchrotron Light Source (NSLS).

The composite damaged by etching (first composite) was examined with a micro X-ray beam at 25 keV (wavelength, λ = 0.496 Å) at the 1-ID-C beam line (SRI-CAT, Sector 1), APS. The beam size was adjusted with incoming beam slits from 30 x 30 μm^2 to 90 x 90 μm^2. Similar to the composite first examined with the 2 x 2 mm^2 beam, the energy was chosen to provide a through-thickness average of the strains from each phase (see Section 4-2).

To obtain the desired diffraction geometry, a four-circle goniometer was used in transmission mode. The diffraction vector was maintained along the fiber axis, thus the diffraction patterns provided the longitudinal (or axial) strain in the plane of the composite. The diffraction intensity was collected with a NaI scintillator detector equipped with a Si (111) analyzer crystal. The X-ray beam size was defined by slits on the incident beam side. An internal standard Si powder, (NIST, Standard Reference Material 640a) attached to the specimen surface, verified beam and sample stability (Figure 4-3).

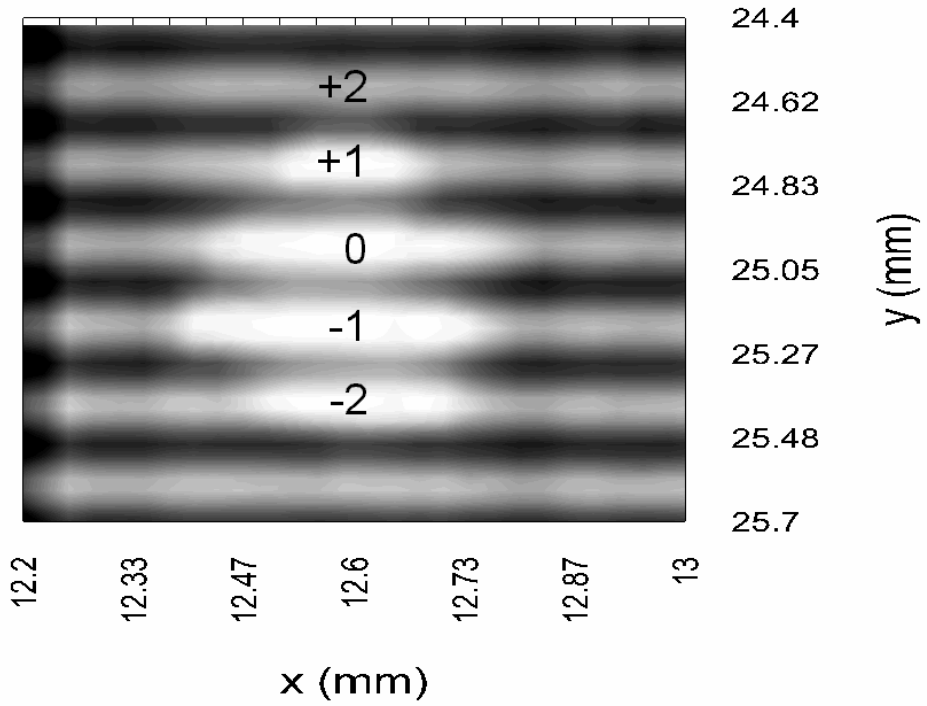

Figure 5-8 Absorption contrast image of the damaged region in the first composite as captured by the Si diode. Intensity is proportional to absorption, i.e., the darker a region the higher the absorption. The contrast is primarily due to Ti thickness. The low density SiC fibers do not reveal features such as cracks. The absence of matrix from the surface of the sample near the damage region is evidenced by the bright region near the center of the image. The periodic change in intensity along *y* corresponds to the position of SiC fibers in the matrix. The fibers examined are labeled by number. Matrix regions examined lay between the labeled fibers.

The first task was to determine the location of the buried fibers around the damage region. A Si diode, which monitored the transmitted beam intensity during each experiment, provided contrast from X-ray absorption due to the large difference in the absorption coefficients of the matrix and fibers: 36 cm^{-1} for Ti and 4.6 cm^{-1} for SiC (at 25 keV, from [84]). Absorption contrast maps using a 30 x 30 μm^2 beam size provided the sample coordinate system in relation to the laboratory system (Figure 5-8). At the same time, the 2θ detector was set at fixed angles to monitor the intensity of the β-SiC

(220) reflection (Figure 5-9) after loading and the α-Ti ($11\bar{2}$) reflection (Figure 5-10) before loading.

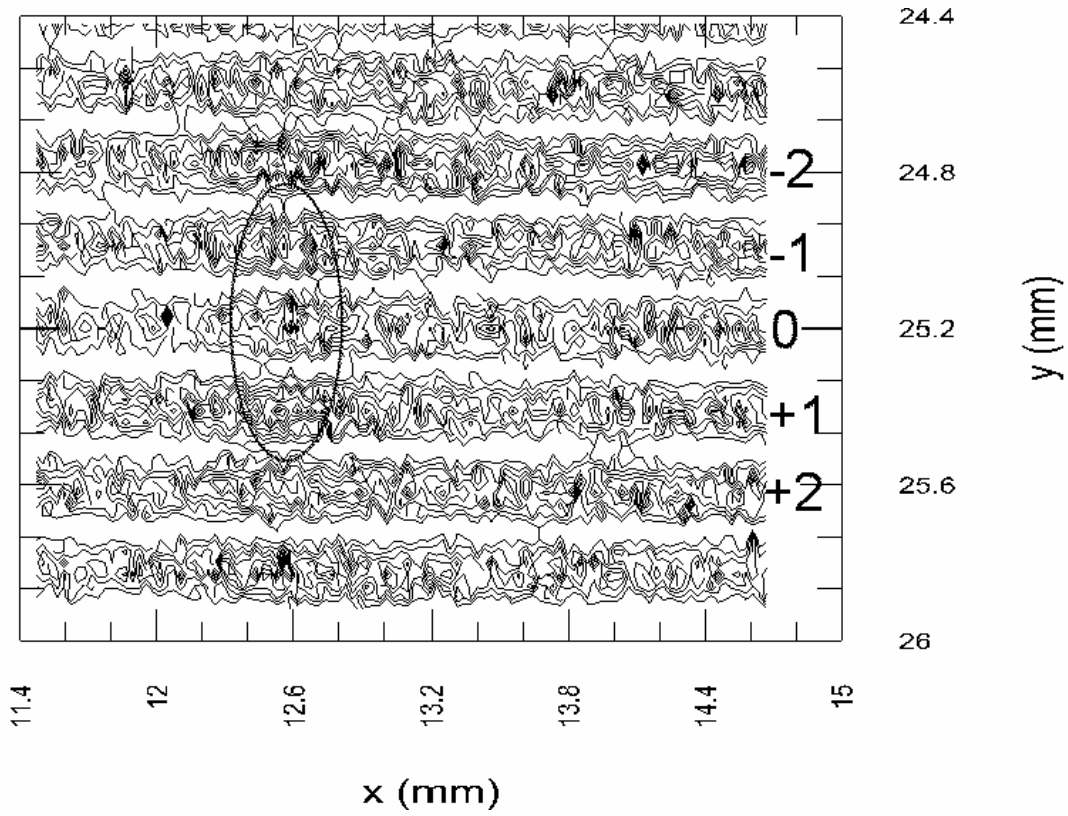

Figure 5-9 Map of β-SiC (220) reflection indicating the location of the buried fibers. The oval outlines the damaged region. Fibers are numbered to indicate their location with respect to the damage zone (at the beginning, "*Fiber 0*" was broken). It is interesting to note that the 30 x 30 μm^2 beam size used in this experiment yielded a continuous map for SiC confirming its small grain size.

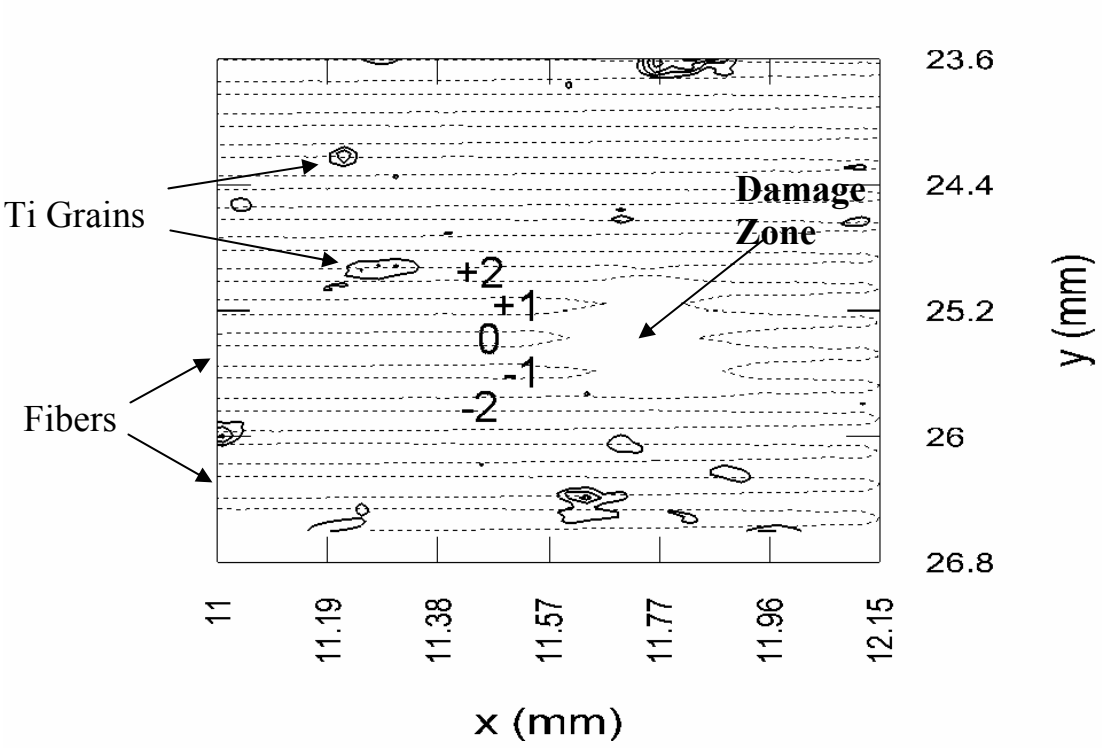

Figure 5-10 Map of α-Ti (11$\bar{2}$) reflection indicating the location of diffracting Ti grains. The marked damage zone and fiber locations are visible from the dashed lines available from the transmission data collected simultaneously during the scan. With an average Ti grain measuring 29 μm across, few grains are oriented for diffraction at a given θ angle. The damage zone marked by the arrow was etched to expose fibers.

At the X-20A beam line of the NSLS, similar grain maps were obtained from the α-Ti (10$\bar{2}$) peak using a 10x10 μm^2 beam focused by a capillary with a lower (9.1 keV) energy. Since this reflection was used for the majority of the matrix strain measurements, a representation of the grain distribution exposes the number and density of grains included in the analysis. This low energy samples a depth equal to one average grain in the matrix. For this second set of grain maps two layers of Ti grains were investigated, first at the surface and another at the fiber midplane. These layers were available from

the surface of the matrix reference sample processed as described in Section 5-2. These grain maps clearly show the distance between grains with respect to the scale and position of the fibers (Figure 5-11). In keeping with the better statistics for this lattice plane, there are more diffracting grains per area in this grain map than seen in Figure 5-10 (the difference, while apparent as shown, is even more substantial when considering that in Figure 5-10 the entire thickness is sampled and in Figure 5-11 only the surfaces are investigated). The grains typically have at least one to two dimensions greater than the fiber diameter. As seen in the grain map, some elongation of the matrix grains in the plane of the fibers was observed (likely due to processing).

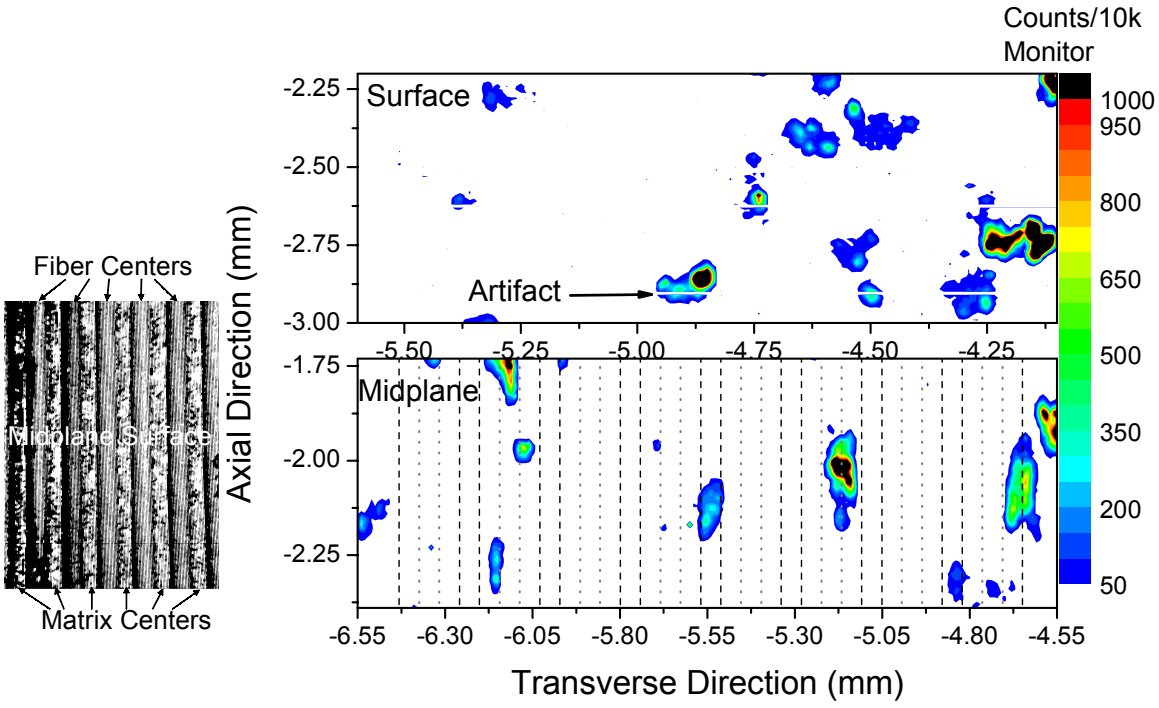

Figure 5-11 The position of diffracting α-Ti grains that contribute to the intensity of the (10$\bar{1}$2) reflection using a 10 x 10 μm^2 X-ray beam. Since 9.1 keV X-rays are used, the examined grains are restricted to the surface of the sample. Both sides of the Ti matrix reference specimen were examined so that a layer of grains is exposed at the surface and the midplane of the sample (see Section 5-2 for description of the matrix reference). A photograph of the midplane surface is shown to the left of the contour plot. The layer at the midplane is also marked with what were fiber centers (between the black dashed lines marking the position the fibers were removed from) and matrix centers (between the grey dotted lines). The white horizontal lines are an artifact common to synchrotron analysis.

Taken together, the maps of diffracted intensity for the fibers and matrix clearly show the contrast between the two regions. Strains measured in the fibers at a scale of the fiber diameter will represent an average over many grains. This averaging makes the resulting strains more representative of a continuum than would be observed if only a few grains were available for diffraction. The total number of matrix grains irradiated by a 90 x 90 μm^2 beam through the thickness of the composite is approximately 60 (assuming the grains were 30 x 30 x 30 μm^3 cubes). Strains taken from the matrix at a scale of the

fiber diameter will potentially represent only a fraction of these 60 grains.* Thus XRD strains in the matrix at a scale of the fiber diameter will clearly be subject to perturbations from intergranular stress.

The effect of broken fibers on the neighboring fiber and matrix regions was studied with a 90 x 90 μm^2 beam at APS (Figure 5-2). This spot size was selected to optimize the diffraction intensity, while still maintaining a smaller size than either an individual fiber or an interfiber matrix region. For the first damaged composite, the four nearest fibers adjacent to the initially broken fiber (nos. = +1, +2, -1, -2), the broken fiber itself (no. = 0), and the intervening matrix regions (i.e., five fibers and four matrix regions—see Figure 5-1, Figure 5-2, Figure 3-3) were scanned along the fiber axes for a distance of 10 fiber diameters in each direction away from the break in 280 μm steps. Additionally, at a significant distance from the break (1.89 mm from the center of the nearest scanned fiber around the damage region), one control fiber and its adjacent matrix region were scanned at each applied stress to obtain a measure of the *in situ* applied far-field strain in the composite. The elastic lattice strains in the matrix and fibers were obtained by monitoring one reflection from the dominant phases in each: (10·2) from α-Ti and (220) from β-SiC. Results from the 2 x 2 mm^2 beam analysis show the α-Ti (10·2) direction is representative of the average in terms of its susceptibility to plastic deformation as well as its effective elastic constant [85] (see also Section 4-7). The diffraction peaks were fit, using the method of least squares, assuming a Lorentzian peak profile for each phase.

*6 to 10 of the 60 grains in the (10·2) direction would be sampled randomly using a point detector with a 90 x 90 μm^2, 25 keV, 0.3° divergent incoming beam (based on the grain maps in Figure 5-11).

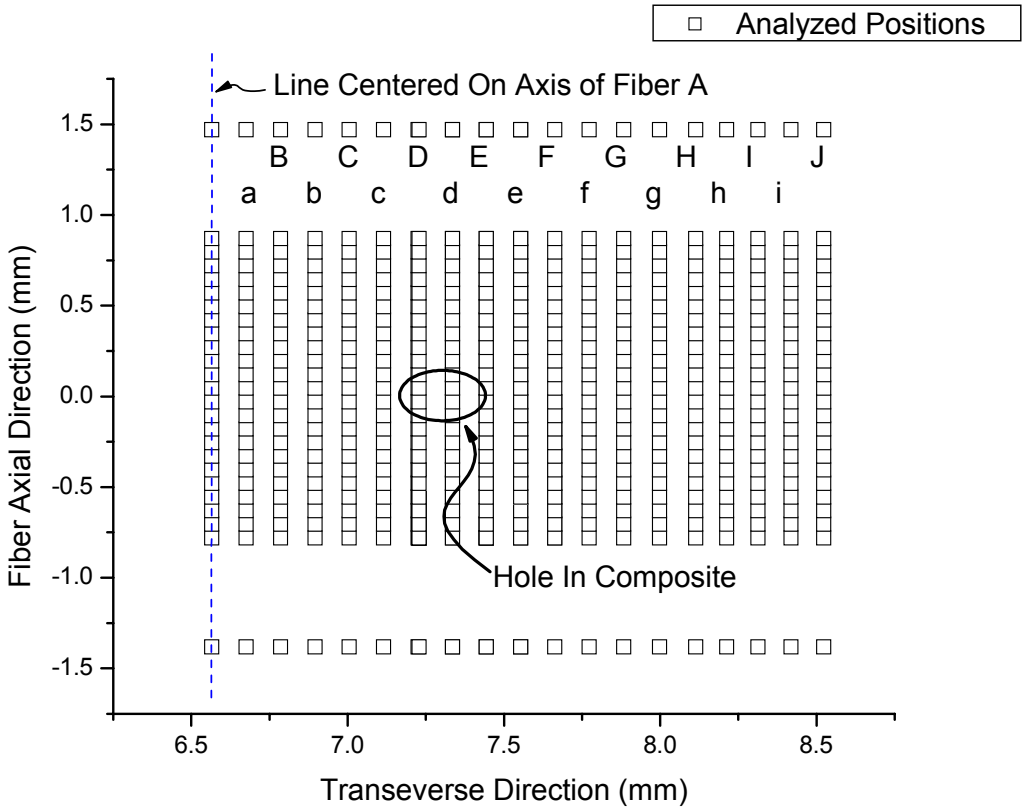

Figure 5-12 A map of the positions sampled for fiber and matrix strains using the image plate method on the second damaged Ti-SiC composite. Each of the 10 fibers was given a label "*A*" through "*J*". Matrix positions are labeled "*a*" through "*i*." A hole was cut in fiber *D* and its neighborhood using EDM and is marked with an oval. The axial positions at +/-1.43 mm provide information for the far-field strains. Time constraints prevented collecting data from each position on this map. Relevant subsets were examined at each applied stress and are shown separately.

The second damaged composite was also studied using a 90 x 90 μm^2 beam at APS. However, in this case the energy was increased to 65.3 keV, the axial step size was reduced to 75 μm near the break, and additional fibers with neighboring matrix regions were examined. The far-field strains were monitored at each matrix column or fiber at a point 10 fiber diameters from the crack plane (Figure 5-12). In addition, to provide better grain averaging for the matrix regions, the image plate was used in this second

examination. Over the course of the study 10 fibers were examined, fibers *A* through *J*. The EDM hole cut in fiber *D* is visible from the radiograph in Figure 5-13.

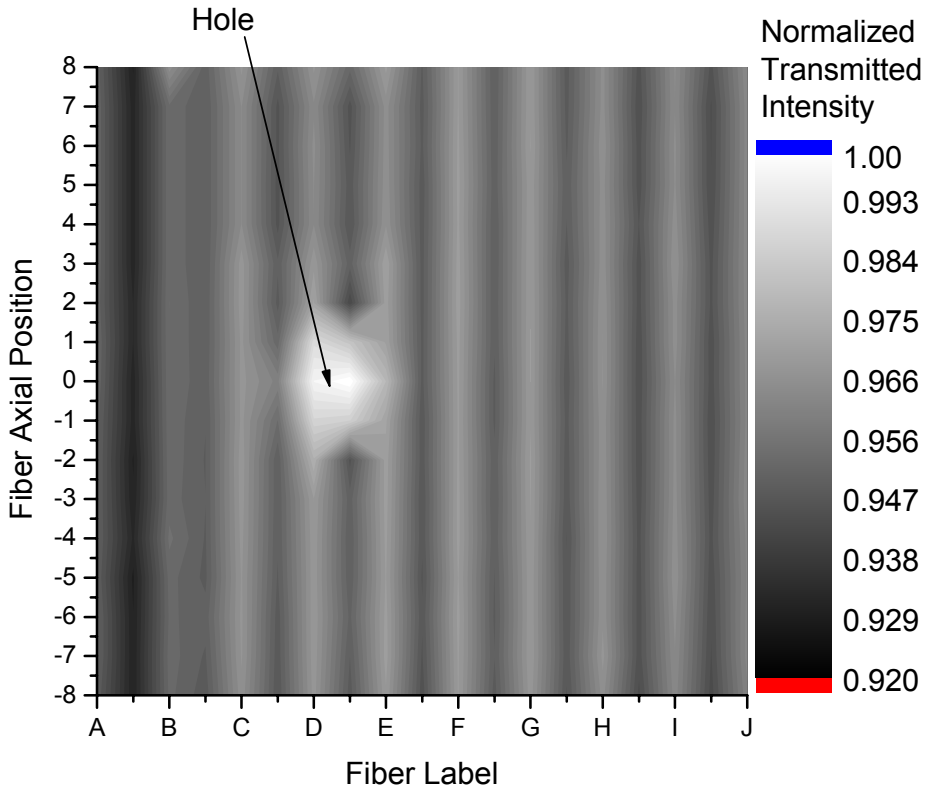

Figure 5-13 The intensity of the transmitted 90 x 90 μm^2 beam at 65.3 keV reveals the position of the fibers, grey columns, and the hole cut in the second damaged composite, a bright spot. Each of the 10 fibers is labeled on the *x* axis. The *y* axis provides the "Fiber Axial Position" which corresponds to the sampling position shown in Figure 5-12 numbered from the center of the hole outward in 75 μm steps. The first fiber, *A*, and neighboring matrix region were examined with a smaller 30 x 30 μm^2 beam giving rise to the lower transmitted intensity before fiber *B*.

Again, the elastic lattice strains in the matrix and fibers were obtained by monitoring the (10·2) from α-Ti and (220) from β-SiC. Calibration was also performed on both samples using the Si (220) peak from the internal standard Si powder, (NIST, Standard Reference Material 640a) attached to the specimen surface.

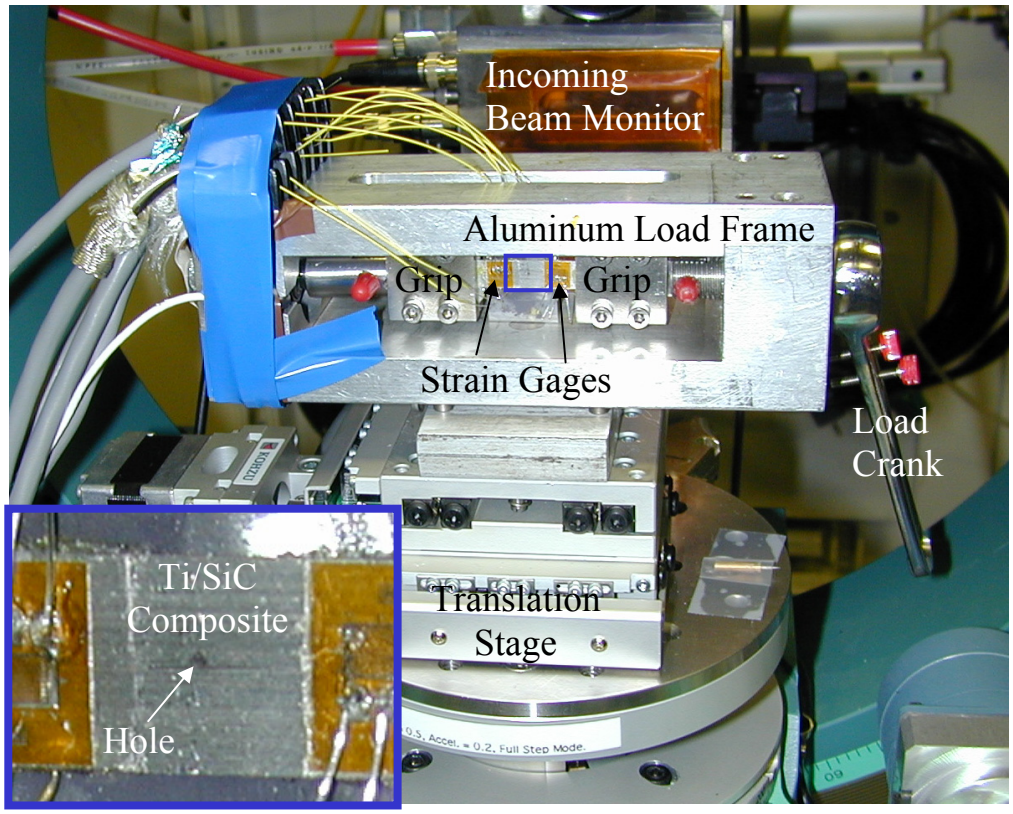

Figure 5-14 Photograph of the load frame mounted on the goniometer in hutch C downstream from 1-BM (bending magnet 1) at APS. The sample with a hole is shown in the grips. See inset (marked by blue rectangle) for a close-up of the composite. Placement of the strain gages is also visible in the image. The Si standard powder is mounted on the upstream side (back side in this image) of the sample.

The composites were stressed in tension using a custom-built load frame. The attached strain gages (see Figure 5-2, and Figure 5-14) allowed the applied macroscopic strain to be measured in a conventional fashion, thus providing a secondary means to obtain the global behavior of the composite. While simultaneously recording the strain from the gages, the applied load was logged by computer via a load cell. As with most constant displacement experiments, the load would temporarily decay after it was increased to a new value; hence, more time was required for the load to stabilize as displacement was increased. The scan times logged with the applied stress and

macroscopic strain were matched to the diffraction scan times, and the stresses averaged over the scan time.

The first damaged composite was stressed to three loads. The average stresses during the fiber strain measurements were 90 MPa, 420 MPa, and 530 MPa. The second damaged composite was stressed to 850 MPa. In order to identify the effects from damage, both composites were first examined for spatially resolved residual strains. In addition, the second damaged composite (with the EDM hole) was examined in an unloaded condition (after the application of 850 MPa) in order to observe the change in residual strains due to permanent deformation under load.

5-4. *Microscale Residual Strains*

The lattice spacing measured before applying stress to a composite serves two purposes. The first is to provide a reference lattice spacing grid. This is subtracted from the lattice spacing grid at applied load so that the change in lattice strain may be observed. Using the unloaded composite strains as a reference for loaded strains is particularly important for composites with a damage zone as the residual strains around the damage zone are non-uniform. The second purpose is to measure the initial residual strain in the composite. As with the bulk measurements (Section 4-4), this requires use of a strain-free standard for the reference lattice spacing.

For the composite with an etched damage zone (the first damaged composite), the examination of strains before loading the composite revealed the removal of the matrix relaxed the longitudinal residual (thermal) strains in the fibers near the crack plane (see Figure 5-15 and Figure 5-17). Figure 5-15 also depicts the array of positions examined using the technique. The release of thermal residual strains was due to etching (compare Figure 5-15 with the micrograph in Figure 5-1).

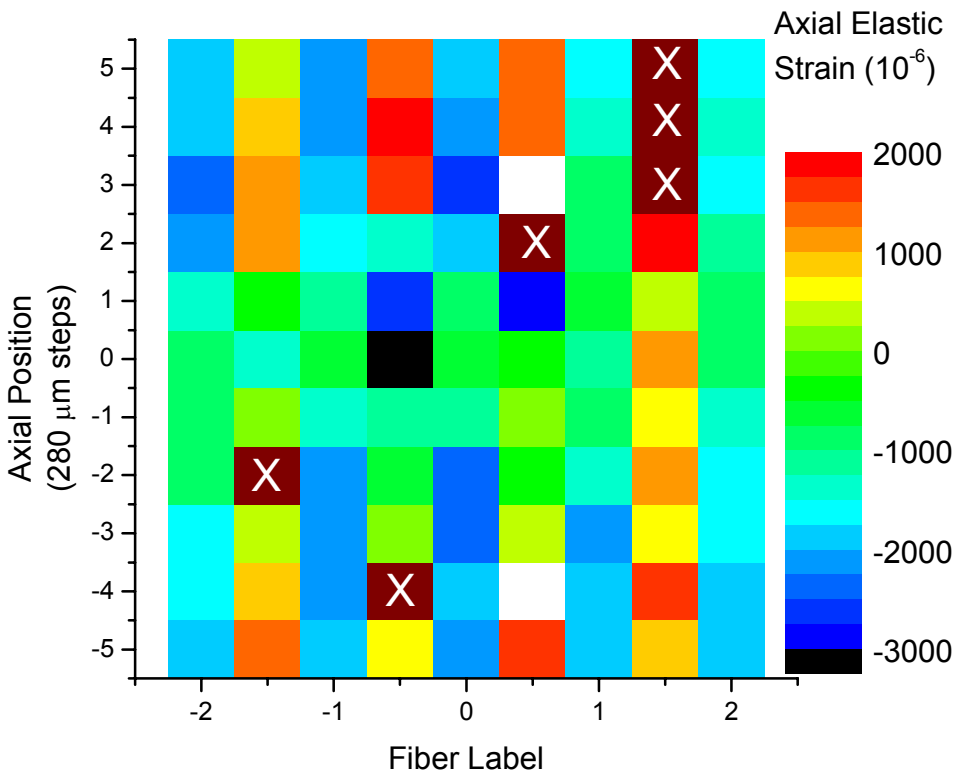

Figure 5-15 The elastic residual strains in the fibers and intervening matrix regions as a function of axial position and fiber number for the damage zone of the first composite. The shade of each square depends on the value of strain measured using the 90 x 90 μm^2 beam at that position. Squares containing an "X" denote matrix positions where grains were not favorably oriented for diffraction. The position of the damage zone can be read from the relaxed (near 0) residual strains.

Since the point detector only observed grains which were oriented for diffraction along constant η, the matrix residual strains could not be obtained in a continuous manner along each matrix column (Figure 5-18); however, for some regions, near a grain with the desired orientation, the diffracted intensity was high. This fluctuation in intensity (see for example Figure 5-16) is the source for the variation in error bars in Figure 5-18. (For more discussion on errors see Section 2-2.)

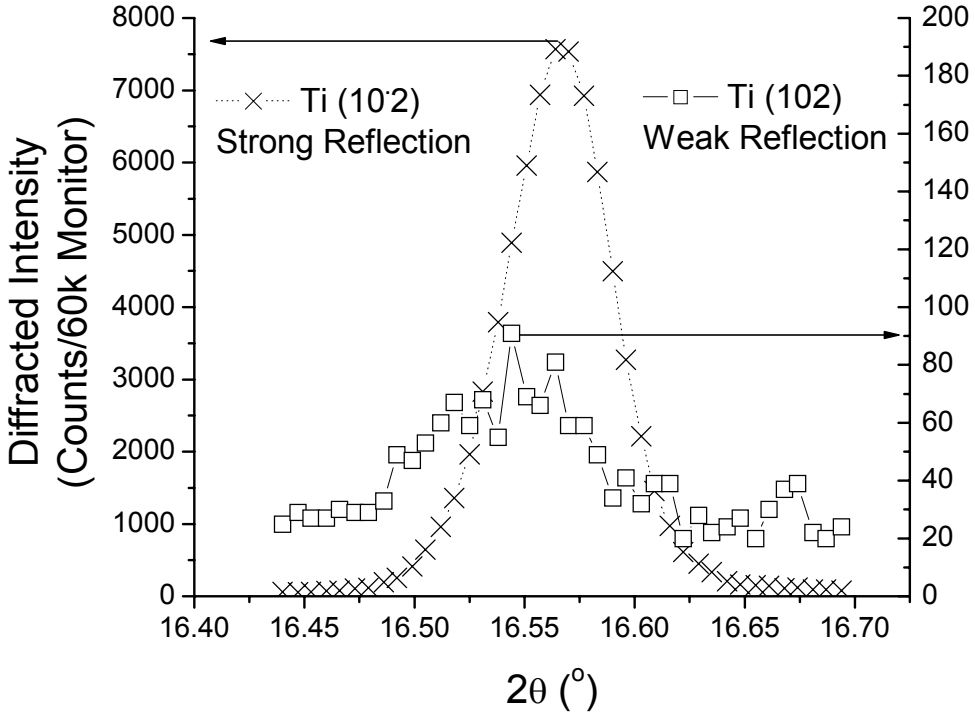

Figure 5-16 Example of diffracted peaks obtained from the matrix using the microbeam and a point detector. The weak reflection shown here contributed to an "X" for the cluster of 3 in the upper right corner of Figure 5-15. Its signal to noise is too low for adequate fitting. The background intensity is the same for both peaks.

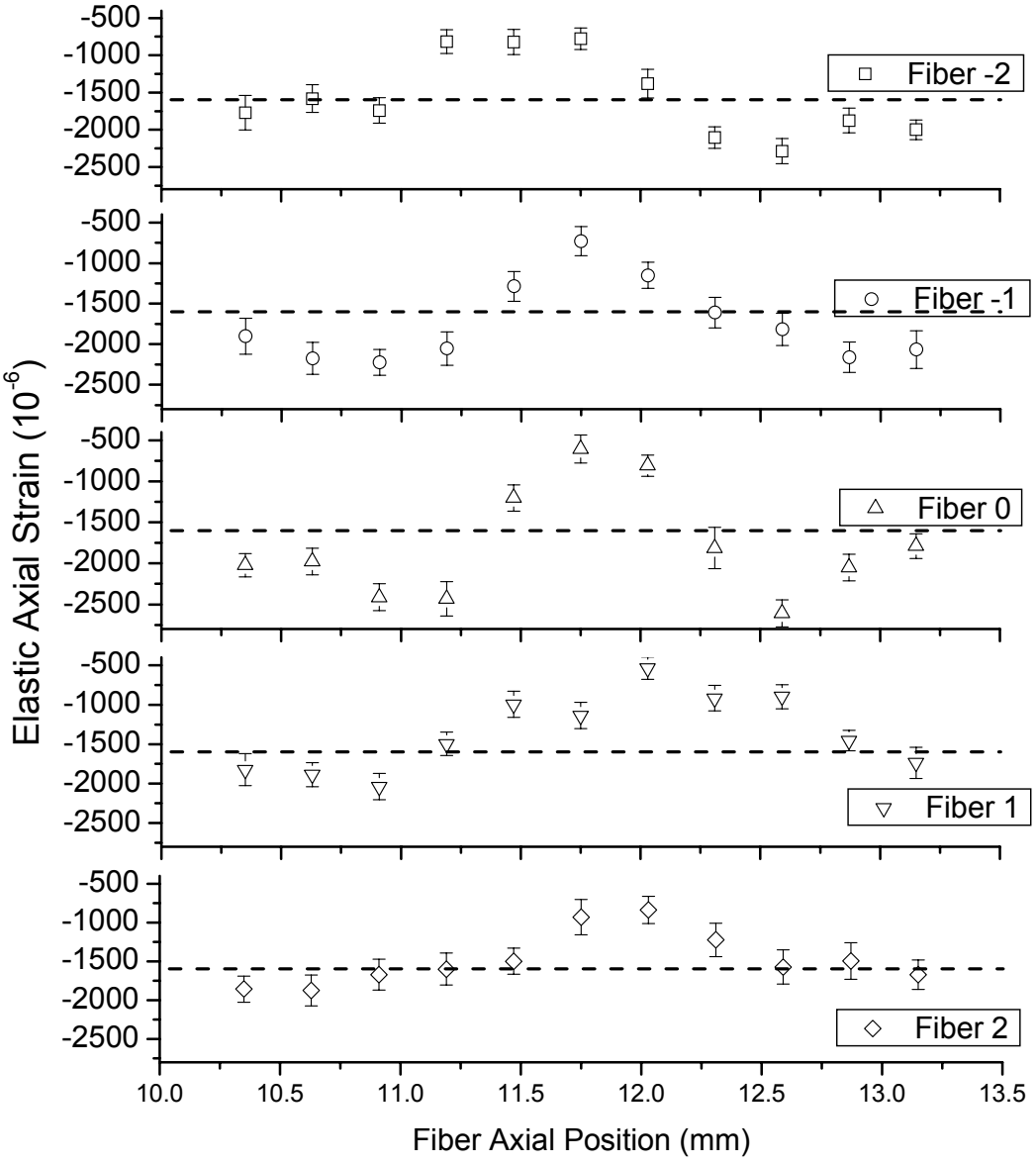

Figure 5-17 Residual fiber axial strain as a function of fiber axial position for the 5 fibers near the etched damage zone in the etched composite. Fiber 0 was broken before applying load. The change in strain for the fibers as a function of axial position is a result of matrix etched from above the fibers. The dashed line shows the strain given by the control fiber far from the damage region.

For the first damaged composite, the residual strains given by the control fiber approach the values at each extreme axial position (far-field region) found in the fibers of the damage region. These strains, -1500 με in the fibers and +1400 με in the matrix, also

agree with the bulk residual strains found in the undamaged composite (see Section 4-4). In the far-field region, the residual strains observed with the microbeam are due to the disparate CTE of the fiber and matrix along with the elastic and plastic anisotropy of the matrix grains. In this region, local variations of 900 με were observed in the matrix across neighboring fibers with a maximum of 1700 με and a minimum of 430 με. Influenced by variations in matrix strains, variation was also observed in the far-field fiber strains (-2066 to -1366 με). Though not available from the bulk measurements, these variations would also be expected in the composite analyzed for bulk properties (Section 4-4). As a comparison, the average value obtained with the 2 x 2 mm^2 beam lies within one standard deviation of the far-field microbeam measurements. Thus, the composite's residual stress state far from the damaged region is similar to the undamaged composite.

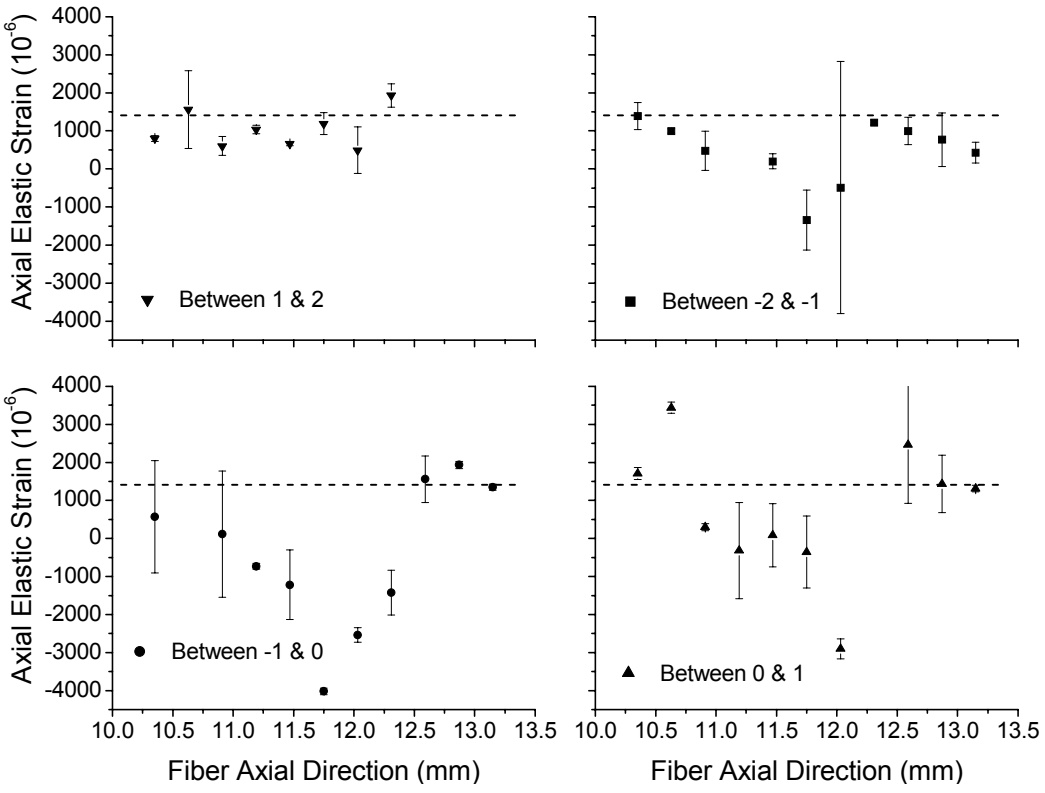

Figure 5-18 Residual matrix axial strain as a function of fiber axial position for the 4 matrix regions between the 5 fibers examined in the first composite. Both the action of etching away matrix from the surface and breaking the fiber acted to create the observed residual strains. The change in error bar length is associated with the presence or absence of diffracting grains. The strains given by the control matrix region are marked by the dashed lines.

The effect of etching the matrix and breaking a fiber was clearly observed in the microscale residual strains. Etching is primarily the source of the decrease in matrix axial residual strains observed near the crack plane between fibers 0 and 1 and between fibers -2 and -1 (Figure 5-18). Particularly between fibers -1 and 0, in addition to the decrease observed from etching, a large degree of residual axial compression was measured in the matrix strains due to the action of breaking fiber 0 (Figure 5-18). Even far from the damage zone, the matrix residual strain was seen to vary by as much as 50%. This variation was also reflected in the fiber strains creating locations where the residual

compressive stress partially relaxed. The difficulty in obtaining information from the matrix is clear from the absence of strains or large error associated with the diffracted intensity available from portions of the matrix.

In the second damaged composite with an EDM hole, the image plate technique was applied in order to increase the number of matrix grains sampled at each position. Here, 10 fibers and the intervening matrix regions were examined. External calibration of the absolute strains using the strain-free references was not available with this method. Therefore, translation error between the references and the composite was not compensated making the absolute residual strains potentially less accurate than the residual strains measured in the previous composite. In order to observe the significance of potential translation errors, a separate analysis of translation error was made on the second composite using the unstrained internal standard Si powder. From the Si (220) ring position, the standard deviation due to translation was 70 με with random fluctuations up to 114 με. These errors are small compared to the measured strains, ~5% of the total measured strain. Complications from overlap of the standard peaks with other Ti reflections, make further study of the potential translation errors beyond the scope of the analysis technique. However, a clear residual compressive or tensile state can be deduced from the data obtained from the second composite. Since this composite was processed along with the previous composite, the far-field residual strains were expected to be similar. To distinguish strain results of the two composites, the 10 fibers were given letter names for the composite with an EDM hole studied with the image plate versus the numerical labels used in the first composite with an etched damage region.

The EDM hole visible in the transmission contour plot (Figure 5-19) was also clearly visible in plots of the residual strain field around the hole in both the fiber and matrix (see Figure 5-20, Figure 5-21, and Figure 5-22). The fiber axial strains were in residual compression with a tendency towards less residual strain closer to the hole. Similar results were obtained from the transverse fiber strains, except to a lesser degree of tension.

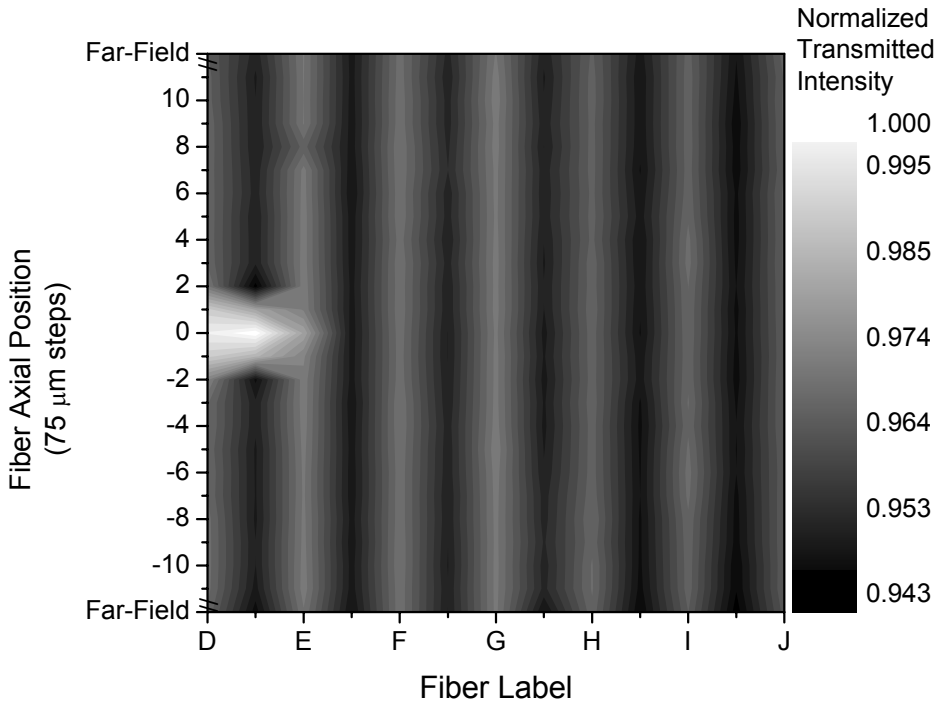

Figure 5-19 For each fiber examined (*D* through *J*), the transmitted intensity measured by a silicon diode divided by the incident intensity measured by an ion chamber is plotted for each axial position sampled along the fiber. The fiber positions are identified by the lighter shade, more transmission, and the thicker matrix regions by the darker shade associated with less transmission. The hole appears the brightest. The axial position spacing is 0.075 mm except for the two extreme "far-field" positions, +/-12, which were an additional 0.6 mm from the previous point (Figure 5-12).

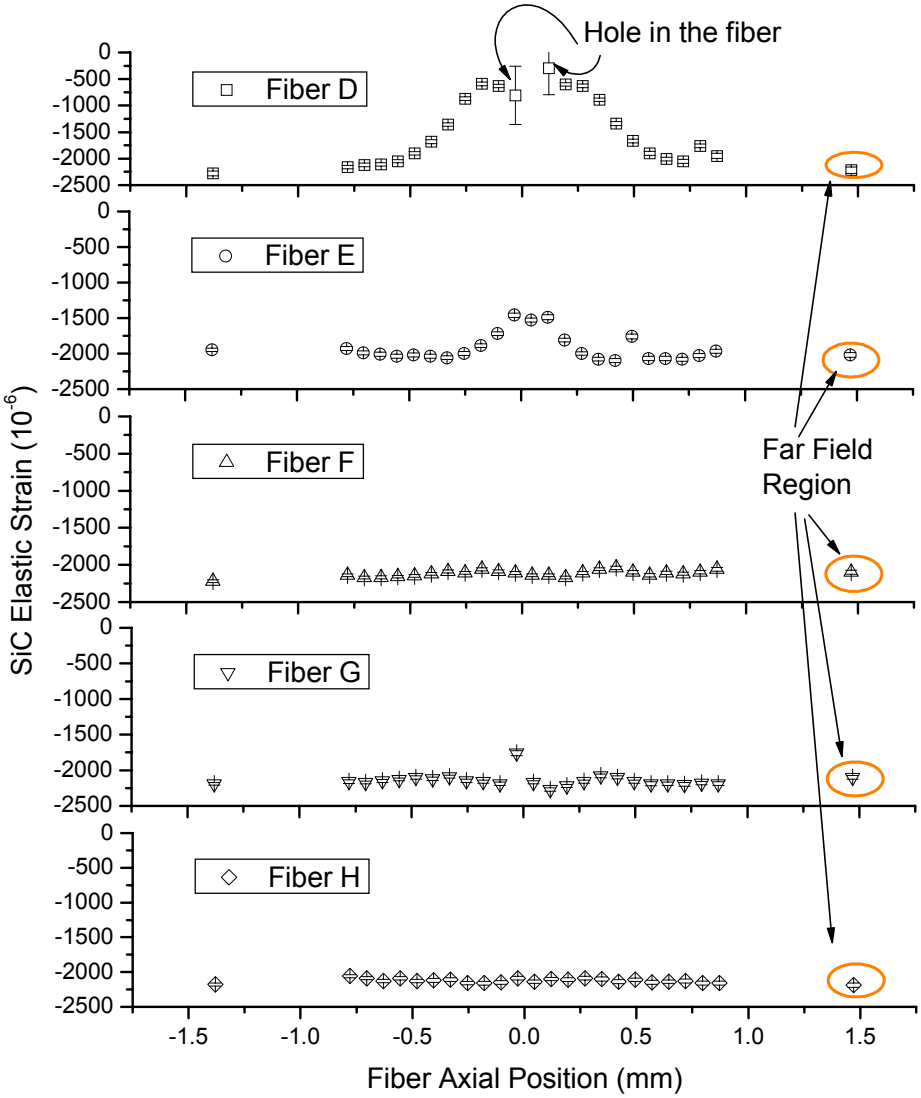

Figure 5-20 The axial residual fiber strain as a function of fiber axial position for fibers *D* through *H*. The "far-field region" marked by an oval will later be used to normalize the fiber strains to compare with a micromechanical model. Two more fibers, *I* and *J*, (not shown) were similar to *H*. The error bars are smaller than the data points for all but two points near the hole on fiber *D*. The poorer statistics available from these positions is due to less diffracting material in the beam.

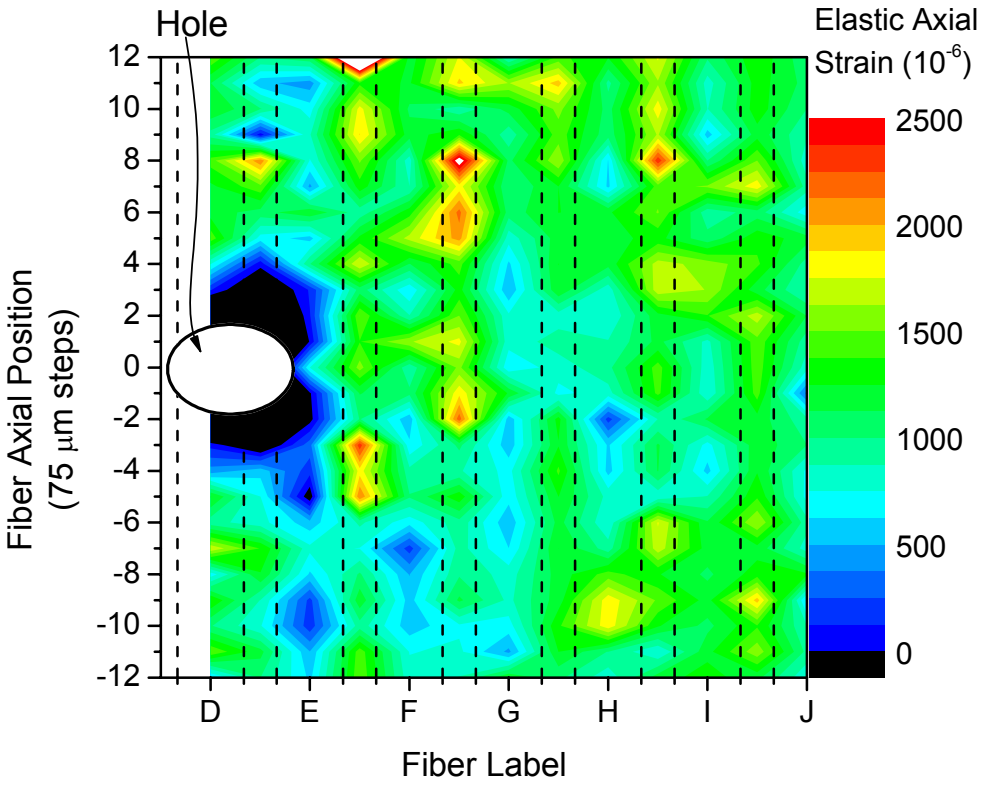

Figure 5-21 A contour plot of the matrix axial elastic residual strain for the regions associated with the fibers, marked by the fiber label, and between the fibers. The presence of the hole around axial position 0 diminishes the residual strains in the matrix around fibers *D* and *E*. Even at regions distant from the hole, variation is present in the matrix residual strains. Compare spatial resolution with Figure 5-15.

Table 5-3 The average axial strain in matrix regions between the fibers (*lower case*) and matrix regions located at the fiber (above and below, *upper case*). Total averages for each region are in bold.

Position	Mean Strain (10^{-6})	Standard Deviation (10^{-6})
g	1239	259
H	968	371
h	1414	361
I	1051	286
i	1387	213
J	883	195
Between	**1347**	**278**
At Fibers	**967**	**284**

Since matrix material exists not only between the fibers (Figure 4-1), but also above and below the fibers, Ti matrix strains were available from both regions. The residual axial strain from the latter matrix regions is on average 380 με less than the strains measured between the fibers (Table 5-3). The FEM does not predict a significant variation in axial strains between these two matrix regions (see Section 3-1). However, the transverse and out-of-plane strains are predicted to change significantly between these two positions. The transverse strains change opposite to the direction observed axially and would only influence the measured axial strains if the sample was significantly misaligned in ψ (see Figure 2-3). The out-of-plane strains are in the direction of the

beam. Over the fiber, the FEM predicts compressive strains in the out-of-plane direction (ε_{yy} in Figure 3-1), but between the fibers it predicts a gradual change from compressive to tensile with an average close to zero. Some minor influence from these strains is expected, since the scattering vector $(q)^*$ is a few degrees out of the plane of the composite ($\theta = 0^o$ with $2\theta < 10^o$), but the 28% change observed between each position is greater than would be caused by a few degrees in the q vector alignment. Furthermore, since the out-of-plane strains are expected to average close to zero between the fibers, they should have even less effect on the axial strain measurements between the fibers even for a significant 2θ. Thus, there exists a measurable axial strain difference in the two matrix neighborhoods not seen in the FEM.

As a comparison to the axial matrix strain measured in the acid-etched (first) composite, the axial matrix strains measured in the EDM-cut (second) composite using the image plate show no missing regions since grains diffracting in all η orientations are included in the analysis (compare Figure 5-21 with Figure 5-15). Increasing the number of sampled grains in this way causes a reduction in the measured local fluctuation of strains suggesting the measured strains are close to an average value for the region investigated. The additional grains also lead to a significant improvement in the average specific error (see error bars Figure 5-22 compared to Figure 5-18). Thus, with the analyzer crystal, grain-specific strains were revealed compared to the image plate where a representative average strain over many grains even for the 90 x 90 μm^2 region was obtained. What does appear as scatter in the matrix residual strains should not be

*Direction along which the strain is measured (see Figure 2-3).

considered experimental error, but real variation in the matrix strains, a result of intergranular stresses (Figure 5-21 and Figure 5-22).

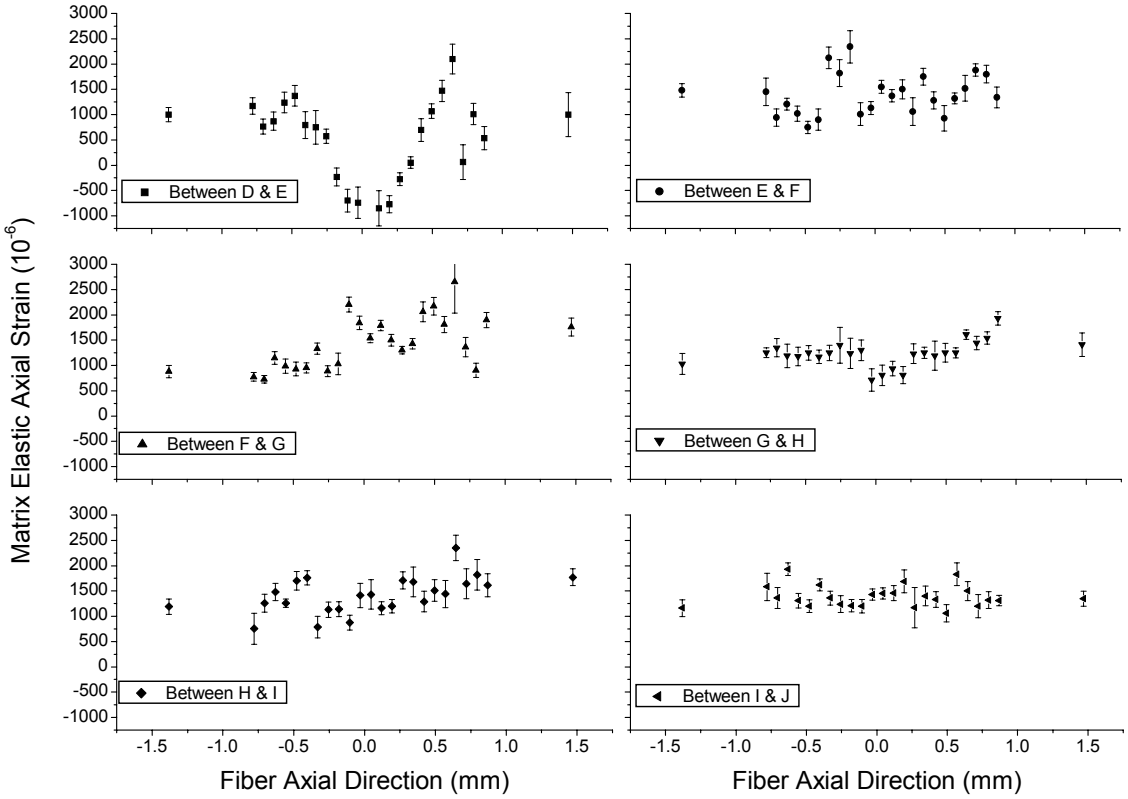

Figure 5-22 The axial residual matrix strain as a function of fiber axial position for the regions between fibers *D* through *J*. The effect of cutting the matrix is primarily visible in the matrix between fibers *D* and *E*. The other matrix regions show fluctuations in strain, but since they are also observed far from the hole, they were due to possible spatial variations in processing and/or intergranular stress. The image plate clearly improves the ability to observe matrix strain (compare with Figure 5-17).

Far from the hole, a more striking contrast between the two versions of matrix regions was available from the matrix transverse strains. The matrix material between the fibers was on average in a transverse residual compressive state, primarily due to thermal residual stress. Whereas the matrix above and below the fibers is on average in a transverse residual tensile state (Figure 5-24), also primarily due to thermal residual

stress. The difference between the strain states in these regions can be understood from a three-dimensional perspective of the composite.

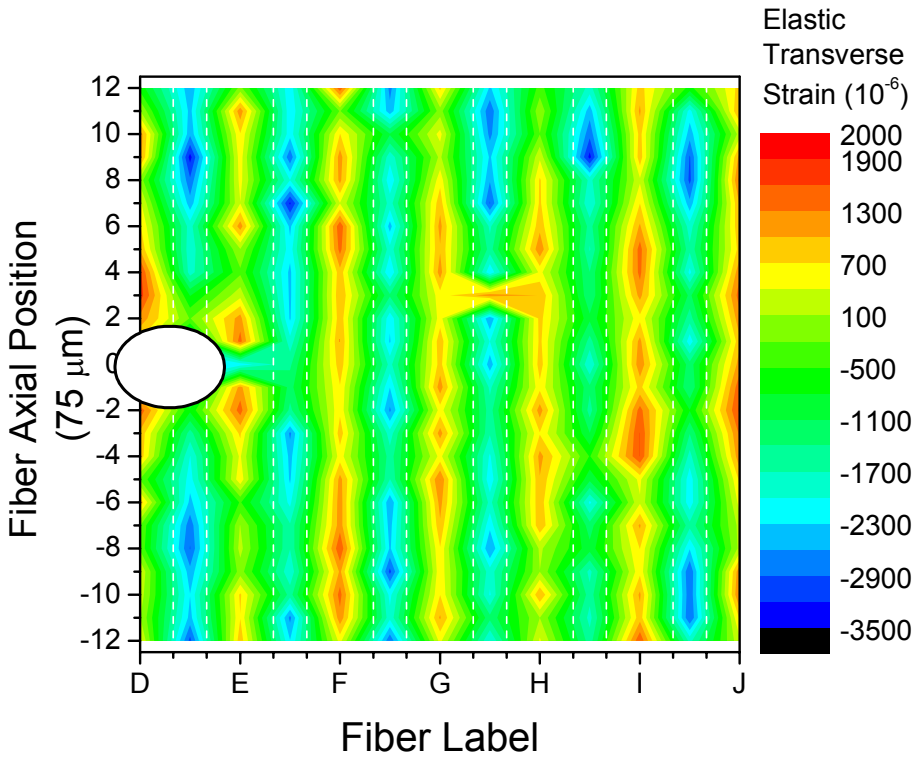

Figure 5-24 Matrix transverse residual strain from the α-Ti (10$\bar{1}$2) peak. Residual compressive strain (dark shade) was observed between the fibers and residual tensile strain (light shade) was observed in the matrix above and below the fibers (marked by the "Fiber Label" positions).

The main contribution to the residual strain component measured by diffraction for the matrix regions above and below the fibers stems from the thermal mismatch between the fiber and matrix along the circumference of the fiber. This mismatch contributes to a residual tensile hoop strain in the matrix upon cooling. Between the fibers the compressive residual strain is again a result of coefficient of thermal expansion mismatch. However, in this region the contribution from the compressive radial component of the matrix strain to diffraction is greater than the tensile hoop component.

Two line plots from the FEM predictions of the transverse thermal residual strain illustrate the difference between the two positions in the matrix (Figure 5-23). Both lines are perpendicular to the plane of the composite, but the first is centered in the fiber and the second centered between the fibers. The FEM also reveals a variation in matrix strain with depth (the out-of-plane direction). This variation contributes to the strain broadening also observed in the transverse matrix strains.

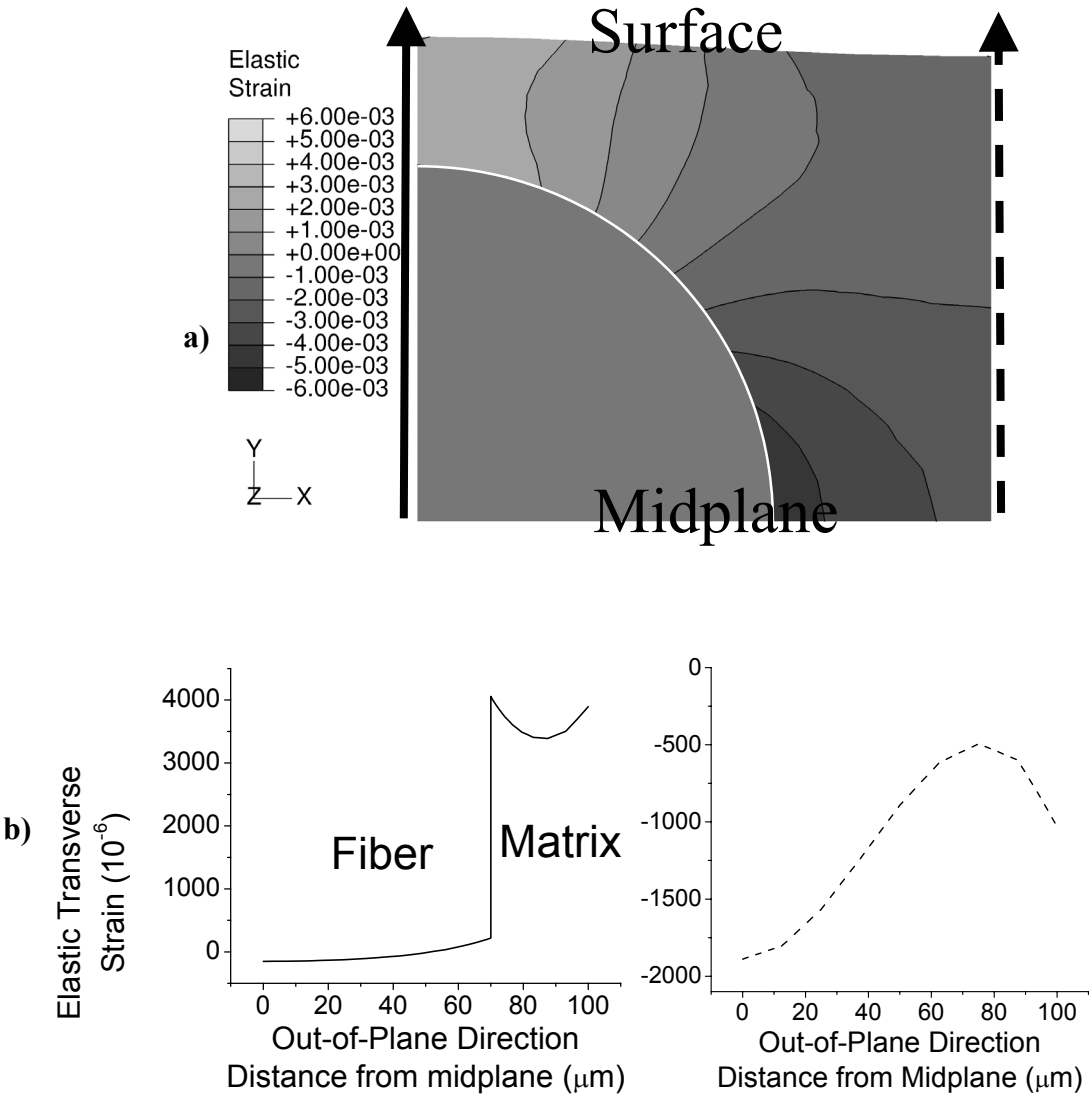

Figure 5-24 a) The FEM prediction from Figure 3-1 with a solid and dashed arrow along the border of the plot exposing from where the solid and dashed lines for part "b)" were taken. **b)** Transverse thermal residual strain predicted in the composite by FEM. A center line along the fiber from the midplane of the composite to the surface shows tensile strain in the matrix (solid line). The transverse strains in the matrix centered between the fibers is compressive (dashed line).

In summary, the measured residual strains revealed the effect the CTE mismatch had on each phase (axially compressive in the fibers, axially tensile in the matrix with a periodic variation in the transverse matrix strain associated with the position of the

fibers). Relaxation of the thermal residual strains in both phases was seen near the region of damage in both composites. With the analyzer crystal, grain-specific strains were revealed in the matrix compared to the image plate where a representative average strain over many grains even for the 90 x 90 μm^2 region was obtained. Even in the far-field region, the grain-specific matrix residual strain was seen to vary by as much as 50%.

5-5. *Microscale Load Sharing*

In this section, the micromechanical behavior of the composite under tensile load is explored. Again, both phases in each damaged composite are considered. The damage is shown to evolve first through fiber failure then through matrix plasticity. The fiber and matrix strains were measured at three applied loads in the first composite for the same positions given in the residual strain section (Section 5-4). The second damaged composite was examined at higher applied load. These results describe damage evolution in the composite and will be compared with the MSSL model in Section 5-7.

For the individual fibers, the residual strains were subtracted from the total measured strains when stress was applied. This is defined as the *applied strain* and will be presented in the following figures. For the second composite, the applied load was significant enough to induce global matrix yielding, so in addition to the applied strains the total strain (residual + applied) will also be presented.

In the first damaged composite, fiber +1 broke between the first and second applied stresses (90 MPa and 430 MPa). This evidence of damage evolution during loading is depicted on Figure 5-25. This figure plots applied stress vs. axial fiber lattice strain at the crack plane in each of the five fibers examined around the etched damage zone. From Figure 5-25 the stress/strain behavior of fiber +1 is seen to resemble that of the initially broken fiber, $n = 0$, above 100 MPa deviating from that of the intact fibers. This deviation reveals that fiber +1 broke while applying stress to the composite. Figure 5-25 also shows that, for a given applied stress, the intact fibers closest to the broken fibers carry the majority of the load given up by the broken fibers (i.e., at the same applied load

the strain is greatest for the intact fiber closest to the break). The behavior of fiber -2 (a second nearest neighbor to the break) shows strains similar to the control fiber far from the break.

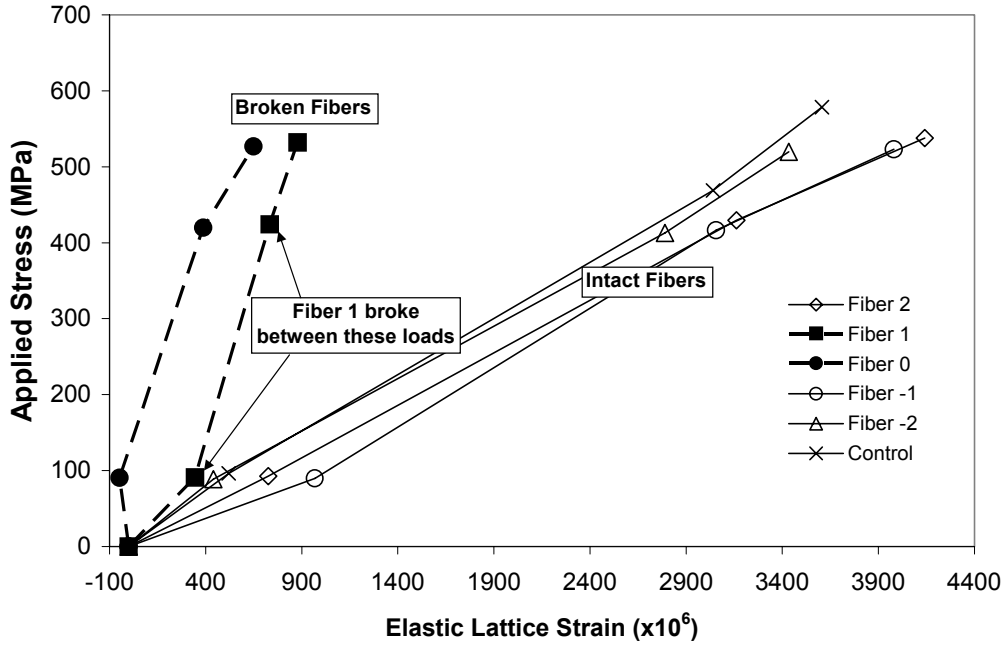

Figure 5-25 Damage evolution under tensile load at the crack plane (x = 0 in Figure 5-1). Applied stress is plotted against applied axial lattice strain in the five fibers around the damage zone. At the beginning of loading, only fiber 0 was broken. When the stress/strain profiles of the intact and initially broken fiber are compared, it is obvious that fiber +1 broke between 90 MPa and 430 MPa.

Understanding the load transfer requires an examination of the strain along the fiber and matrix as a function of axial position. For example, only the crack plane is shown in Figure 5-25, but the strain transfer to the neighboring fibers is expected to occur along a direction which results in an axial strain profile that is not necessarily maximum at the crack plane [34, 81] (see Section 3-2.1 case (i)). In addition, the characteristic decay length (δ, Section 3-2.1, Eq. (3-2)) for the broken fibers requires measurements of strain at regular intervals along the fiber axial direction. The strains for the first nearest

neighbor to the naturally broken fiber as a function of axial position from the crack plane were observed in fiber +2 (Figure 5-26). In addition, further confirming the break, strains consistent with a broken fiber were identified in fiber +1 (Figure 5-27), the strain along the axial direction in fiber +1, under the larger applied stresses, also resembles the strain for the initially broken fiber, fiber 0 (Figure 5-28). The strains in the other first neighboring fiber to the break (fiber -1) are seen in Figure 5-29. As seen from Figure 5-30, the second nearest neighbor also shows sensitivity to the broken fibers.

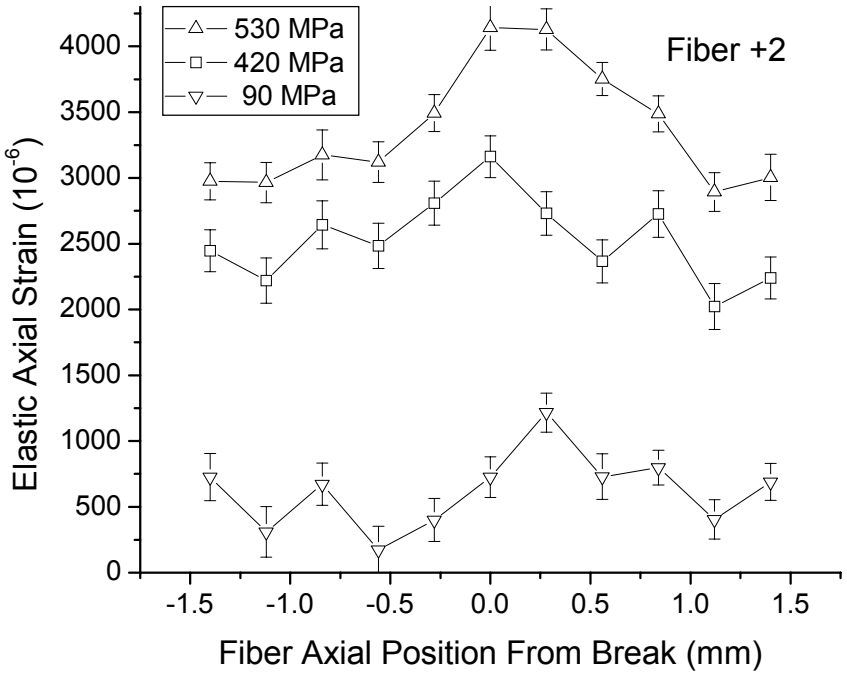

Figure 5-26 Applied strain in the first nearest neighbor fiber to the natural break (fiber +2, first damaged composite) for each load as a function of the axial position in the fiber. Load transfer (increase in strain compared to the far-field) from the broken fibers is realized even at the smaller load and continues to increase its magnitude and breath as the load increases.

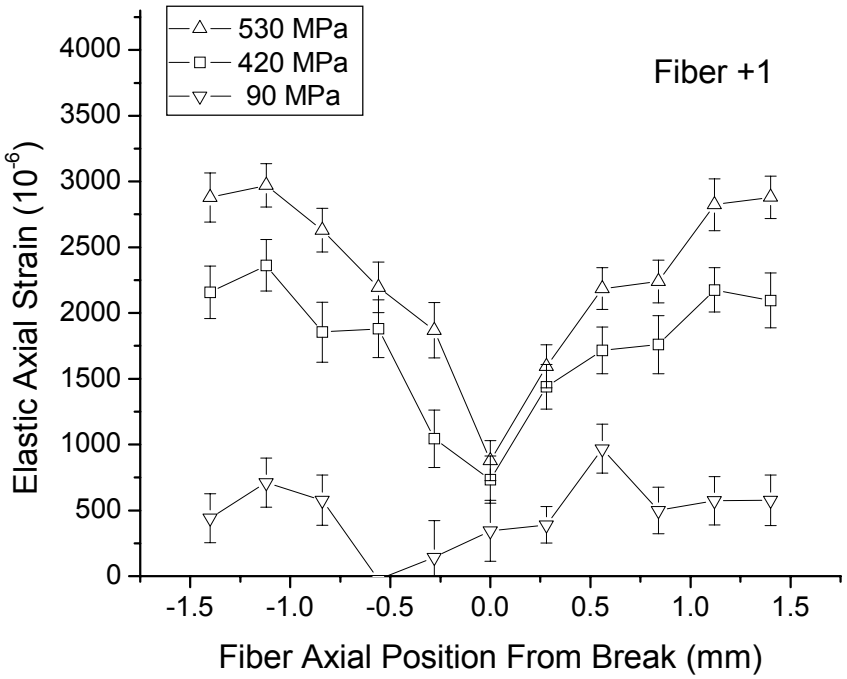

Figure 5-27 Applied strain in fiber +1 which naturally broke while loading the first damaged composite. The fiber shows a clear decrease in strain at the break plane.

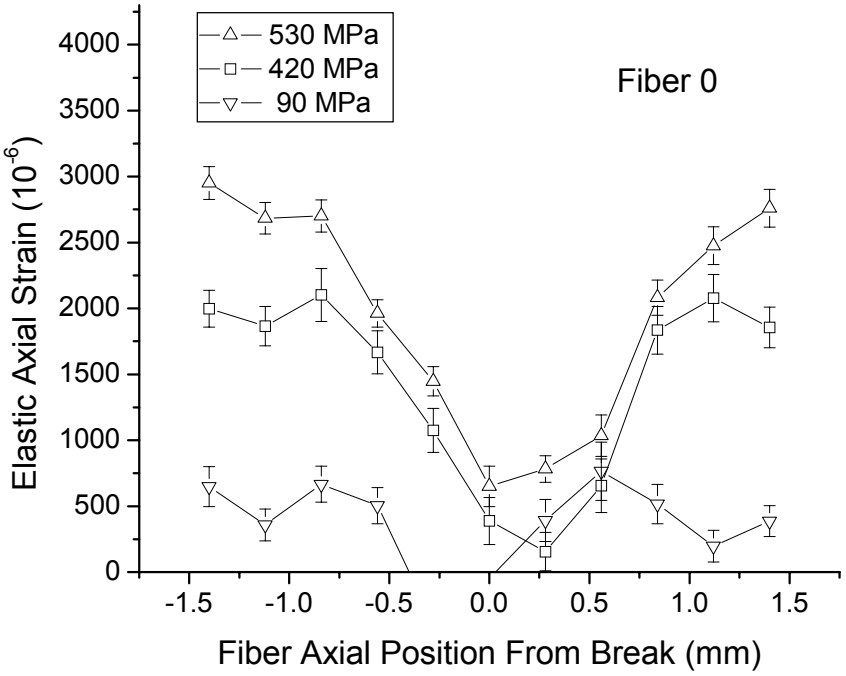

Figure 5-28 Applied strain in the initially broken fiber as a function of axial position from the break. The wider profile observed in this fiber's strains compared to the naturally broken fiber are due to the extent of initial damage in the fiber. (Data also from the first damaged composite.)

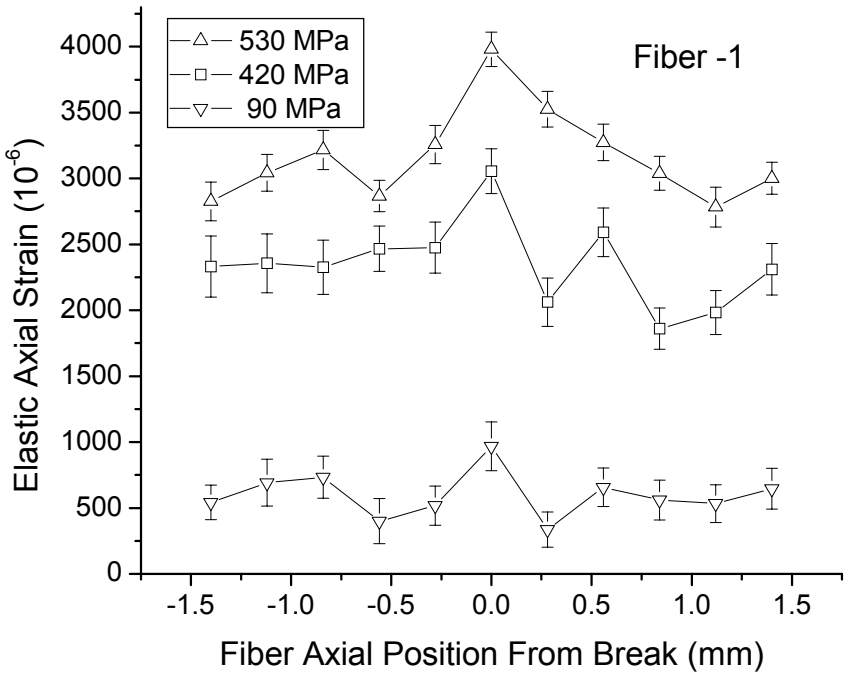

Figure 5-29 Similar to fiber +2, the strains in the fiber which was a first nearest neighbor to the initially broken fiber as a function of axial position from the break are shown. The load transfer is first apparent at the smaller applied stress and increases with increasing stress. The profile looses symmetry with the break plane due to the damage profile in its neighbor (Figure 5-28). (Data also from the first damaged composite.)

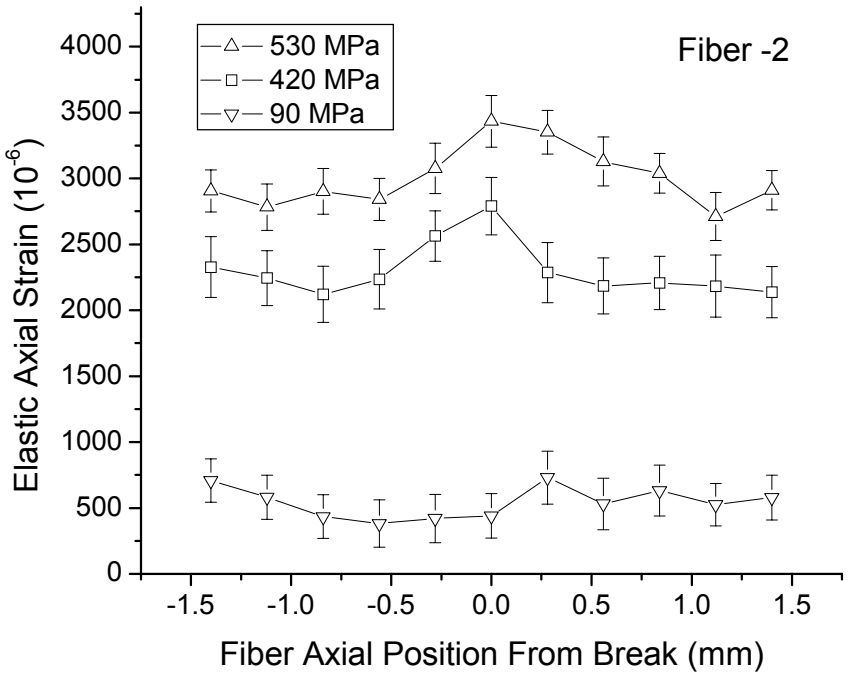

Figure 5-30 Applied strain in the second nearest neighbor fiber to the break (fiber -2) for each applied load as a function of the axial position in the fiber. An effect from the broken fibers is realized even at the smaller load and continues to increase its magnitude and breath as the load increases. (Data also from the first damaged composite.)

Since the composite was examined at multiple loads, multiple strain maps for the fibers and matrix are available. By selecting one load from the strains in the first damaged composite shown in the above figures, a contour plot may be constructed (Figure 5-31). Such a figure constitutes a strain map and shows spatially where load is transferred in the composite. Ideally a higher resolution is desired giving a clearer picture of the spatial gradients. The higher resolution was achieved with the image plate experiment results shown below. However, the results from the first damaged composite do show stress transfer (strain increases compared to the far-field) in the matrix and were beneficial in comparison with the model (Section 5-7).

As was the case with the residual strains (Figure 5-18), the applied strains in the matrix were not always available. However, it is clear from the observed increase in matrix strains that load transferred to the matrix from the broken fibers. The results from the matrix strain measurements are reported in Section 5-7 where they are compared to the model.

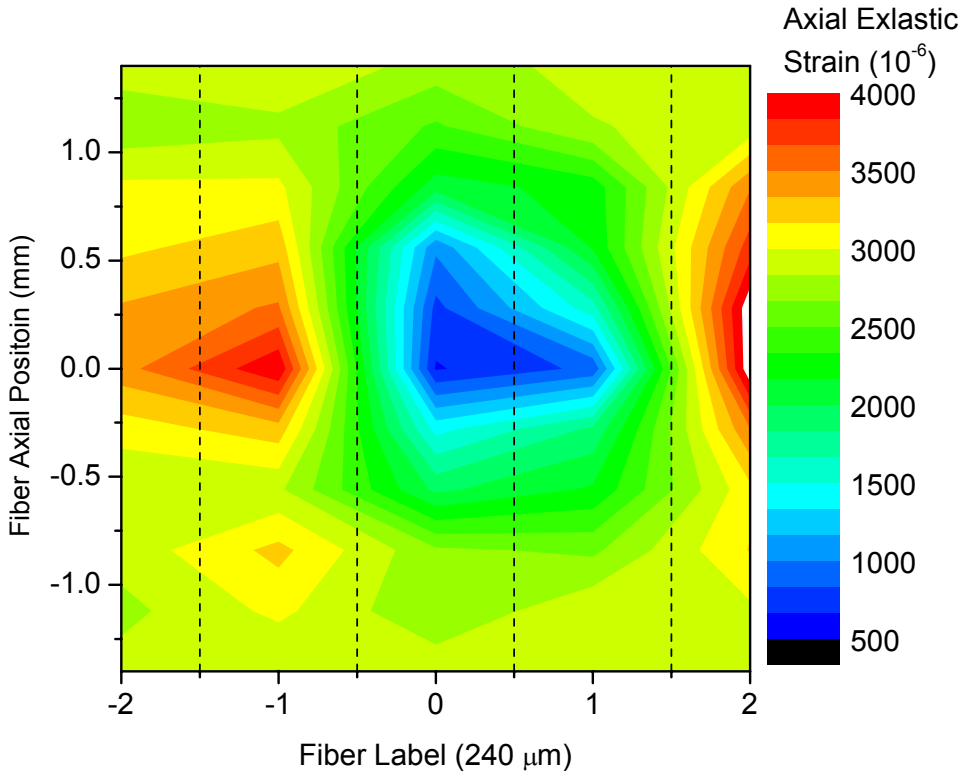

Figure 5-31 Contour plot of the strains at the maximum applied stress (530 MPa) for all the fibers examined in the first damaged composite. The relative position of stress transfer from the break to the intact fibers is clear. The data here is taken from the last applied stress shown in Figure 5-26, Figure 5-27, Figure 5-28, Figure 5-29, and Figure 5-30.

For the second damaged composite, damaged with a hole by EDM (Section 5-1), the 10 fibers examined also show evidence of a fiber fracture during loading. A subset of the positions sampled at the initially unstressed condition (Figure 5-12) were sampled at 850 MPa applied stress (Figure 5-32). The positions at each fiber label were analyzed for

fiber and matrix strains. The positions between the fiber labels were analyzed for matrix strains. The strains for analyzed fibers are shown in Figure 5-33 and Figure 5-34. The axial strains in the matrix are shown in Figure 5-35. The shear and transverse strains in the matrix were also recorded (Figure 5-36 and Figure 5-37).

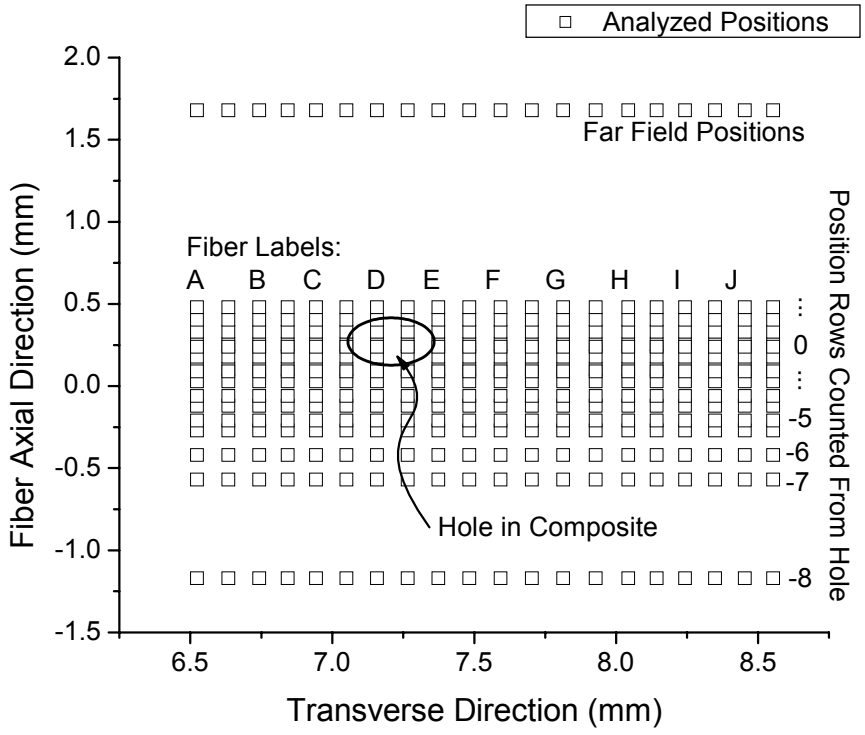

Figure 5-32 Each box represents a position analyzed with the 90 x 90 μm^2 beam. The fibers *A-J* and neighboring matrix regions were analyzed in the configuration shown. These positions are a subset of the positions analyzed before stressing the composite (Figure 5-12). The numeric label for the positions used in the strain contour maps is shown on the right of the figure. For reference, the position of the hole cut in the composite is also shown in the figure.

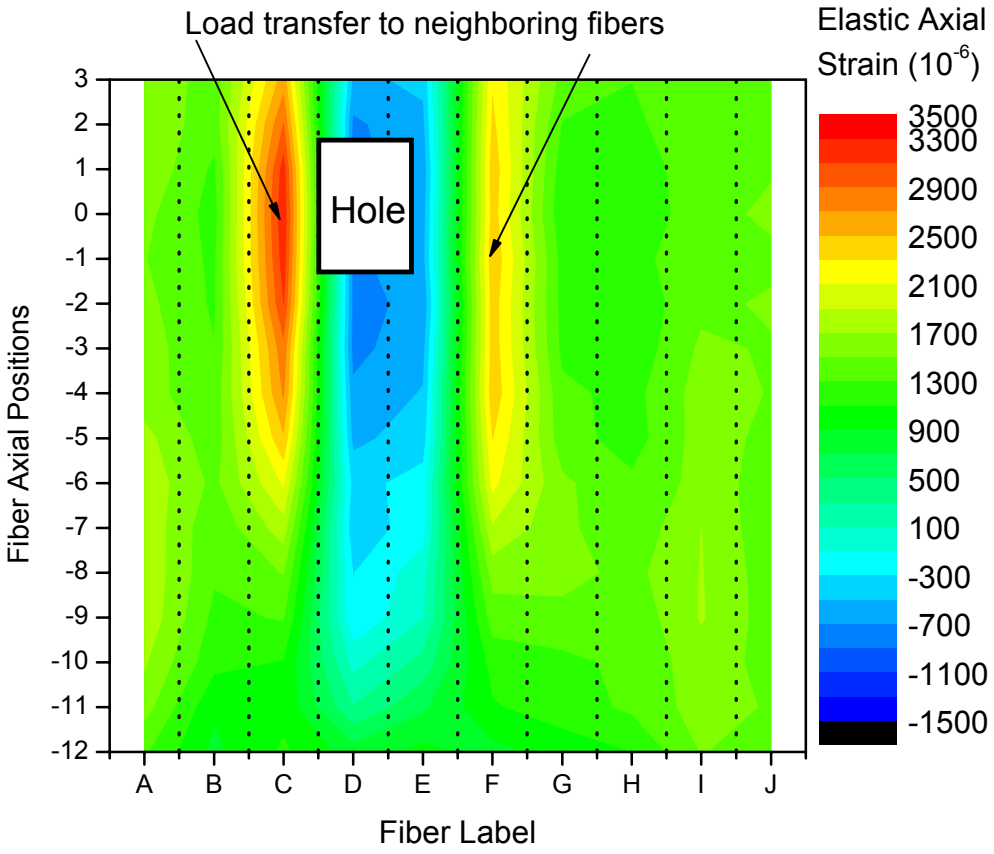

Figure 5-33 A strain map of the <u>total</u> elastic axial strains (residual + applied) in the <u>fibers</u> for the composite with a hole at 850 MPa applied stress. The hole is marked as a square since no matrix regions are shown. The strains reveal a decrease in strain near the hole for the broken fibers *D* and *E* with the first nearest neighbor fibers *C* and *F* compensating with larger strains. The rest of the fibers show strains around 0.11%. Compare with Figure 5-31 prepared from the point detector data.

The total elastic axial strains in the fibers for the composite with a hole at 850 MPa applied stress are shown in Figure 5-33. Approximate absolute strains in the composite may be observed as well as the significant gradient in strains resulting from the combined effects of the damage and the applied stress. Also, since a larger subset of positions was examined at applied load than no load, the total strain map provides the opportunity to see the load transfer to neighboring fibers to the left of the break (fibers *A* through *C*). As

expected, some of the load given up by fiber *D* is transferred to its neighbor *C*. On the other hand, as can bee seen from these strains, fiber *E* did not accept load from *D* but shows strains consistent with a broken fiber. In contrast, for the applied strains (Figure 5-34), only fibers to the right of the break (*D* through *J*) were available for analysis. Applied strain is total minus residual, and only these fibers residual strains are known (Figure 5-20). Viewing only the applied strains subtracts out any variations due particularly to the damage and highlights the stress transferred among fibers as a result of the broken fibers.

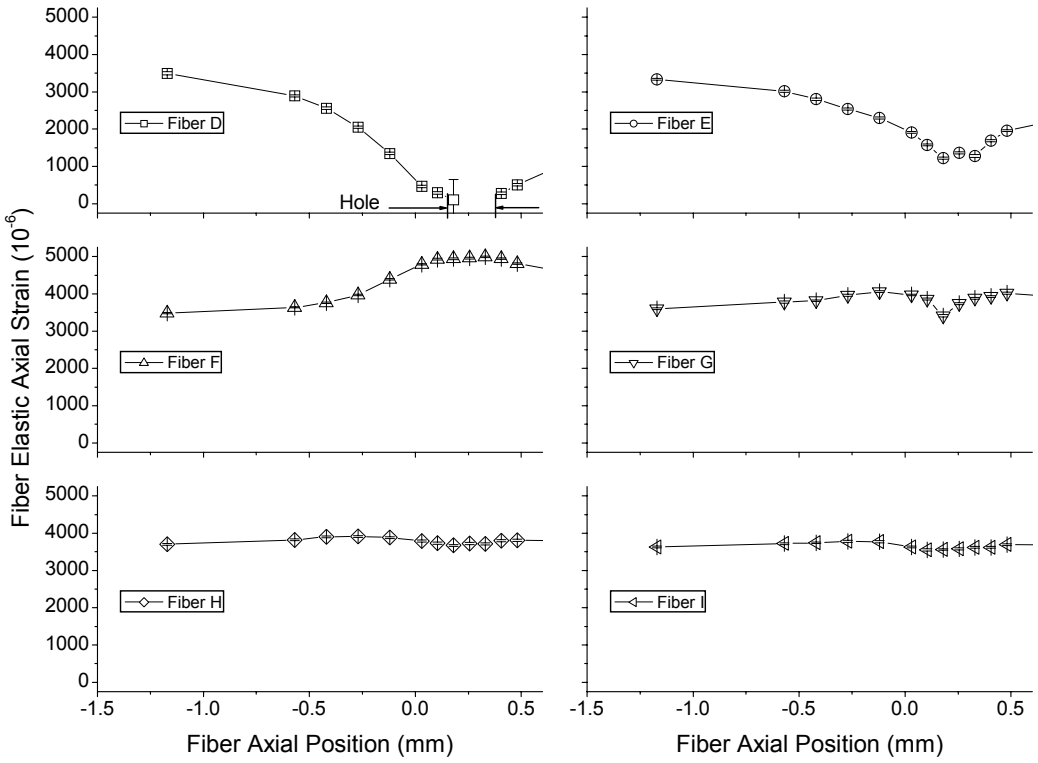

Figure 5-34 The applied axial strains (total strain (Figure 5-33) minus the residual strain (Figure 5-20)) for the fibers *D* through *I* are shown for the 850 MPa applied stress. The width of the hole is marked on the graph for fiber *D*. The spatial resolution and strain resolution have both improved compared to the etched composite previously examined with the point detector. The data point on fiber *D* taken inside the hole showed less intensity, and therefore a greater error than the other positions.

Since these strains were obtained using the HEμXRD[2] method which includes many grain orientations for each reflection, similar figures may be constructed from the matrix strains. Also, since matrix was observed between and at the fiber locations, twice as many matrix strain measurements are available for inclusion in the strain maps as there were for the fiber strain maps. As was observed in the residual strains, the matrix also presents strong transverse strain gradients. These were not observed in the fibers, so the fiber transverse and shear strains are not shown.

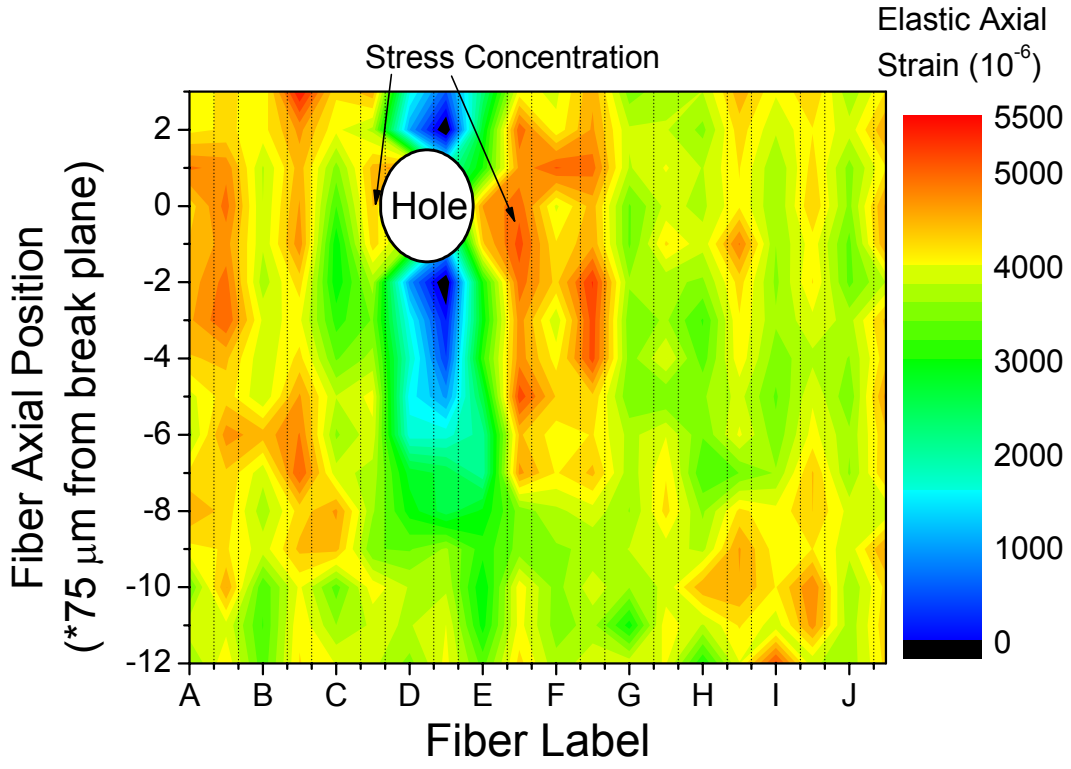

Figure 5-35 A contour map of the total elastic *axial* strains in the Ti matrix for the composite with a hole at 850 MPa. The fiber positions are labeled and separated from the "matrix only" columns by dashed grid lines. The broken fibers appreciably affect axial matrix strains two fiber diameters from the break. Such a figure with continuous strain information from the matrix cannot be constructed from the point detector results.

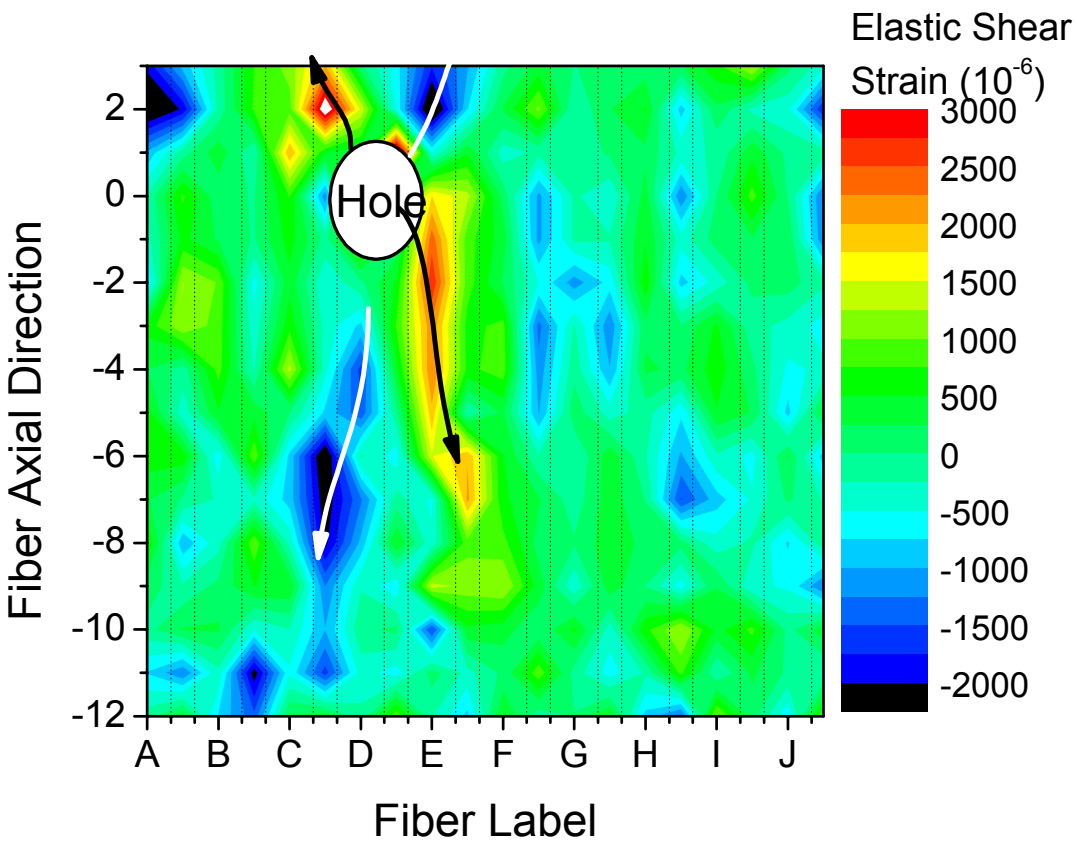

Figure 5-36 A map of the total elastic *shear* strains in the Ti matrix of the composite with a hole at 850 MPa. The effect of load on the hole is observed in the stress concentrations around the hole. Arrows follow the path of maximum shear away from the hole.

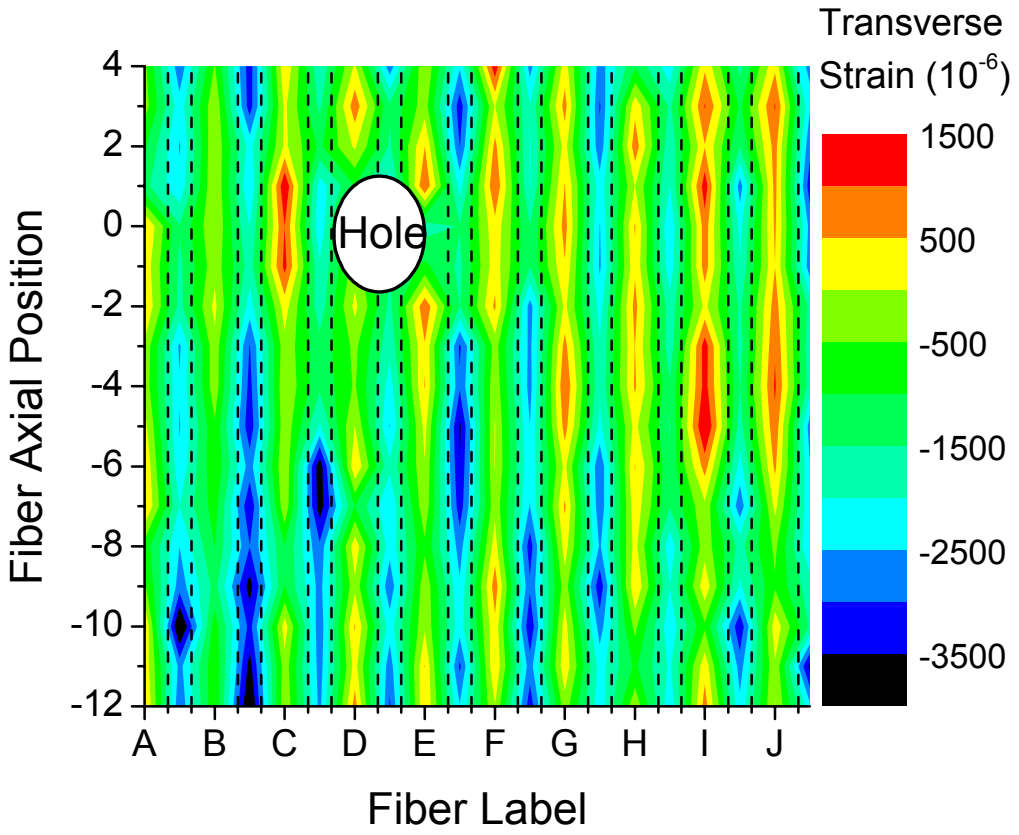

Figure 5-37 A strain map of the total elastic *transverse* strains in the matrix of the composite with a hole at 850 MPa. The strain at each fiber location is tensile but the strain between each fiber is on average compressive.

The spatially resolved applied strains clearly revealed load sharing, fiber breaks, and stress concentrations. Load sharing, or strain transfer, over multiple fibers was observed in both composites. The majority of the strain given up by the broken fibers was carried by the first two neighboring intact fibers. In the broken and intact fibers, the strains were measured along the fibers revealing a recovery to the far-field strains along the length. Also in both composites the matrix was observed to carry load, but a clear picture of the matrix strains was only available from the second XRD[2] experiment. Significant load transfer to the matrix was observed in the second composite. For the first composite an

exposed fiber was observed before and after failure in the composite. Also, in the second damaged composite, a fiber was observed after natural failure. Both X-ray methods provided useful information as a function of position and applied stress. However, the area detector clearly allowed a more detailed and continuous characterization of the composite, particularly in the matrix.

5-6. *Residual Strain Evolution in the Microscale*

Upon unloading, a final examination of the residual strains in the composite damaged with a hole was performed. Changes in the residual strain identify permanent deformation in the composite such as that due to plastic deformation in the matrix. The same fiber and matrix regions were again examined. The position of the composite relative to the beam was measured with a 30 x 30 μm^2 X-ray beam. As with the loaded case, the hole was used as the origin of the measurements shifting the positions to be measured in the original laboratory coordinate system. The monitor normalized transmitted intensity at the sampled positions along the broken fiber are shown in Figure 5-38. Though alignment would be less critical for observing the total strain, subtraction of the initial residual strain requires accurate positioning of the sample with respect to the beam so that the measurement grid for each load is built from the same locations on the sample.

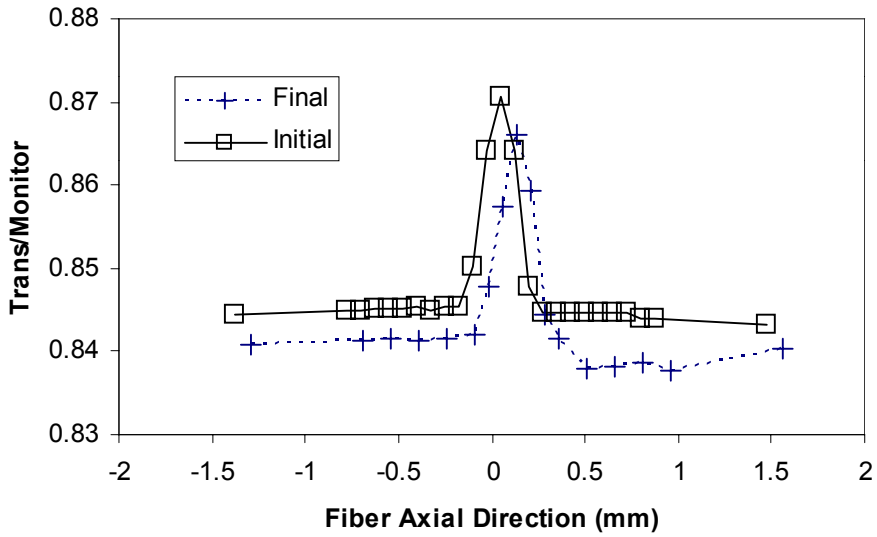

Figure 5-38 A typical shift (90 μm) in the axial position of the hole referenced to the laboratory coordinate system due to changing the load on the composite. The transmitted intensity along fiber *D* normalized by an incoming beam monitor allows alignment in the fiber axial direction. Alignment in the transverse direction may be performed through monitoring the intensity change along the fiber radius (not shown).

The final residual strain state (absolute strain) of the matrix for axial, transverse, and shear strains is shown in Figure 5-39, Figure 5-40, and Figure 5-41. Away from the hole the matrix regions between and at the fibers remained in residual axial tension. Close to the hole the matrix went into residual axial compression. However the matrix regions between the fibers were in residual transverse compression as opposed to the matrix regions at the fibers which were in residual transverse tension. The regions of shear strain gradients observed at applied load were also apparent in the unloaded state (compare Figure 5-36 and Figure 5-41).

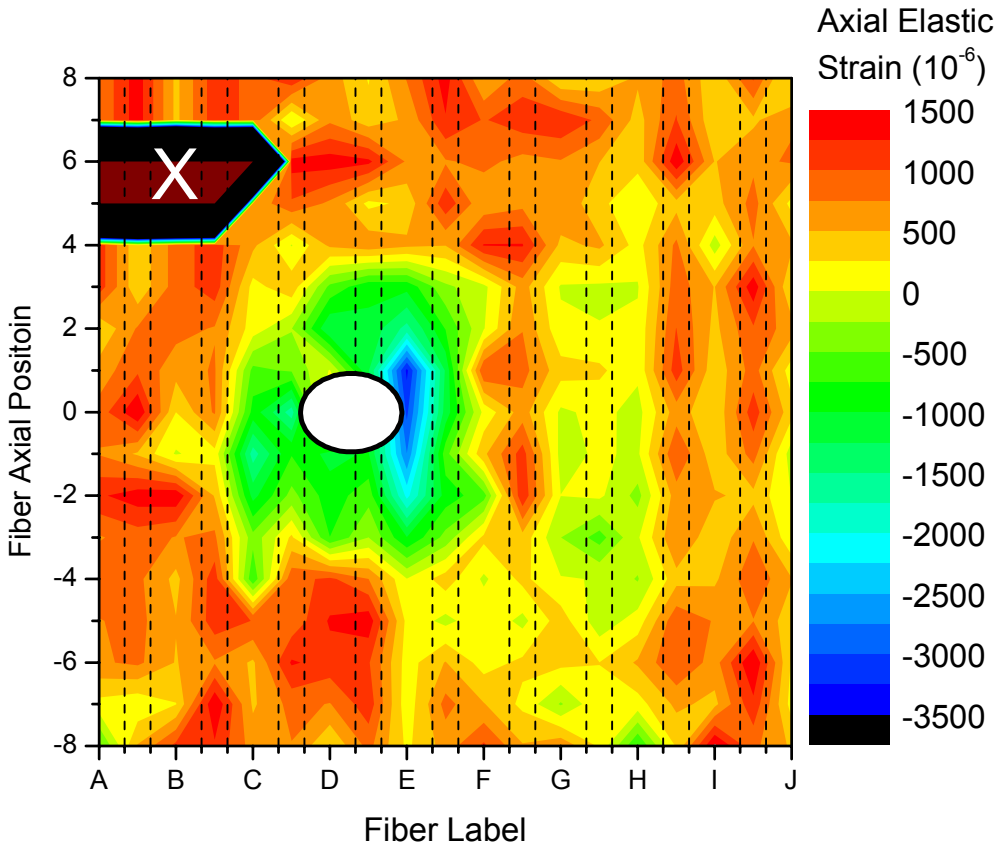

Figure 5-39 Total *matrix* axial residual strain around the hole after loading and unloading the composite from 850 MPa. The position of the hole in the composite is marked with an oval. The region marked by the "X" was not sampled due to time constraints.

As is evident in the SEM micrograph (Figure 5-3), the hole was not symmetric with respect to the broken fiber, *D*. This asymmetry manifests itself in the asymmetric change in residual strains (see for example Figure 5-39). Since these strains are absolute, the peculiarities of each grain's local neighborhood perturbed by the local strains are preserved leading to the observed gradients in even the far-field strains. Subtracting out the residual strains would hide these peculiarities. For example, the axial strain around fibers *I* and *J* exceeds its immediate neighbors (Figure 5-39), but since this was also

observed in the residual strains (Figure 5-21), the change in strain would not reveal the same uniqueness of this region.

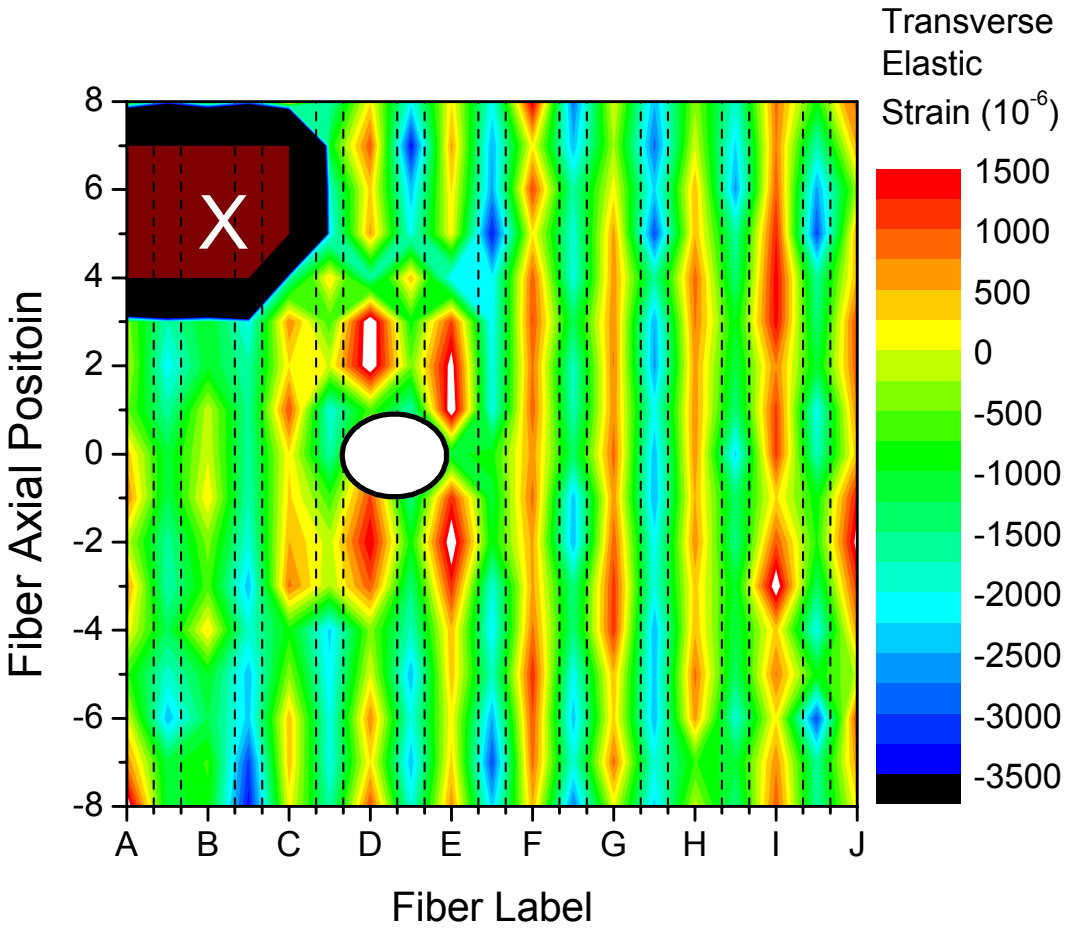

Figure 5-40 Matrix transverse residual strain around the hole after loading and unloading the composite from 850 MPa. The position of the hole in the composite is marked with an oval. The position labeled "X" was not sampled due to time constraints.

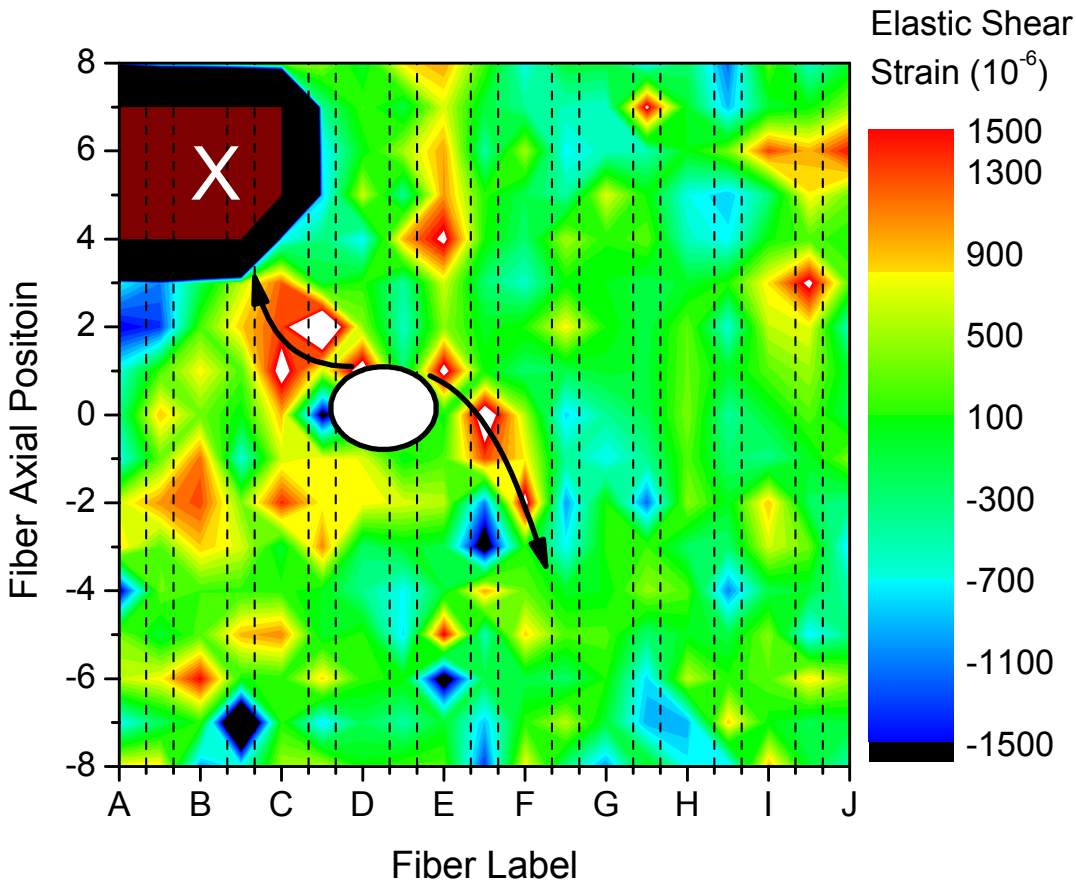

Figure 5-41 Matrix residual shear strain after loading and unloading the composite from 850 MPa. The position of the hole in the composite is marked with an oval. The arrows connect the points of maximum shear strain traveling away from the hole. As with the plots above, the position labeled "X" was not sampled due to time constraints.

Another perspective of the final state of the composite requires subtracting the initial residual strain from the final residual strain. The resulting strain change observed is due to deformation and damage evolution in the composite. Changes in residual strain measured by diffraction have been used to identify matrix yielding in other MMCs [28]. The observation can be understood as follows. The matrix is initially in residual axial tension. When tensile stress is applied, the matrix responds with an elastic strain until yielding begins. Then the measured elastic strain diminishes while yielding continues

and load is transferred to the fibers. In the loaded state, after yielding, the residual strains have already changed. The yielding tends to relax the initially compressive residual strain in the fibers. As the composite is unloaded, the elastic strain given up by the matrix along with some of the elastic strain given up by the fibers is recovered. But, in the matrix, the elastic strain from tensile loading is not enough to bring the composite back to zero applied stress, so the strains in the matrix continue to progress elastically past their initial residual strain state (which was tensile) and the fibers never get a chance to recover all the way back to their initial residual strain state. For example, far from the hole, deformation in the composite created a compressive change in the residual axial tensile strains—a sign of global plastic strain in the matrix (the light contours in Figure 5-42). Close to the hole between fibers *D* and *F*, the change in residual strain increases further, suggesting a region where additional axial plastic strain occurred in the matrix. And, as expected, no change in residual strain was observed at free surfaces immediately above and below the hole. Systematic errors such as displacement during the application of stress would have appeared as false strain. This lack of change in axial residual strain immediately above and below the hole provides internal evidence that the measured strains are reasonable and not subject to significant systematic errors (Figure 5-43).

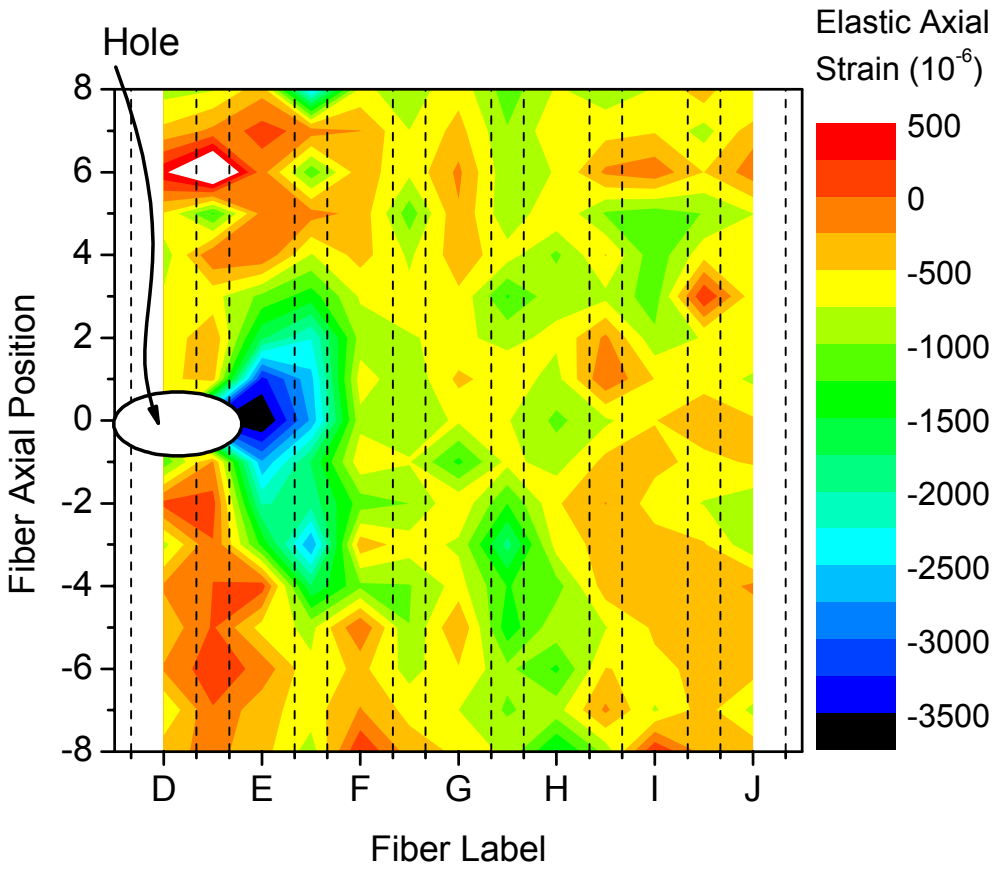

Figure 5-42 Strain map of the change in *matrix* axial residual strain due to loading (to 850 MPa) and unloading the second composite. The matrix over the broken fiber, *D*, is the first column on the left of the map. The darker regions identify locations of greater plastic deformation while loading the composite.

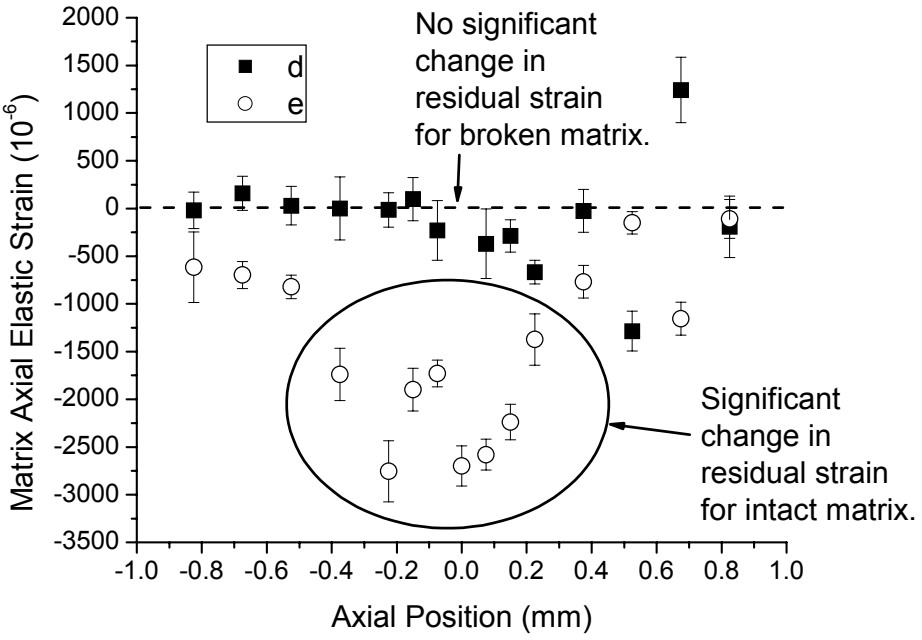

Figure 5-43 The change in axial residual strain for the first two matrix columns illustrates the contrast between the two regions. Near the plane of the broken fiber significant deformation from the 850 MPa applied stress occurred in the intact matrix column *e*. Since matrix column *d* was broken it could not carry load and consequently did not significantly deform near the break.

Since the composite is unloaded, the fibers must compensate for the new matrix strain state. The fibers do not deform plastically at room temperature and, given a well bonded interface, would return to their initial unloaded strains unless their environment was changed. The plastic strain in the matrix deforms the fibers' environment and mechanical equilibrium requires that the fibers respond to the matrix, balancing the strain. As shown in Figure 5-44 for fiber *E* that broke *in situ*, the change in residual strain for the fibers is in general opposite to the matrix surrounding the fiber.

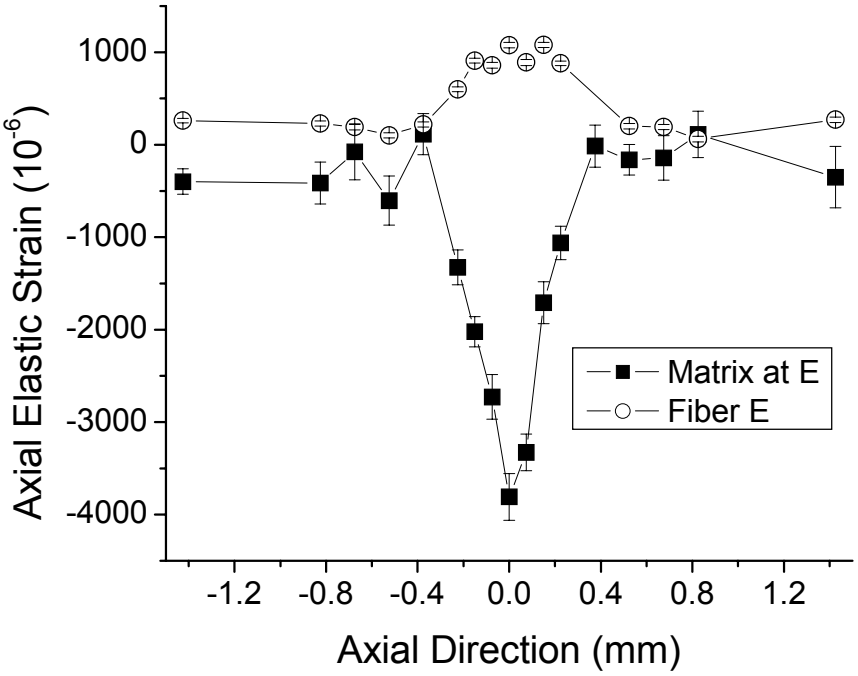

Figure 5-44 The significant change in fiber residual axial strain for fiber *E*, which broke under the application of load. Permanent deformation in the matrix above and below the fiber which deformed as a result of the strain associated with the break is also revealed by the analysis.

As with the cut matrix column, *e* (Figure 5-43), the change in residual strains in the cut fiber, *D*, approach zero near the free surfaces (Figure 5-45). Figure 5-45 also contrasts the strains seen in the cut fiber with the first intact fiber, *F*. As was seen above in fiber *E,* the matrix around *F* permanently deformed due to the transfer of load. With the exception of a point on fiber *G*, the fibers far from the break show a change in residual strain consistent with bulk yielding in the matrix and transfer of load to the fibers (Figure 5-46) [28, 29].

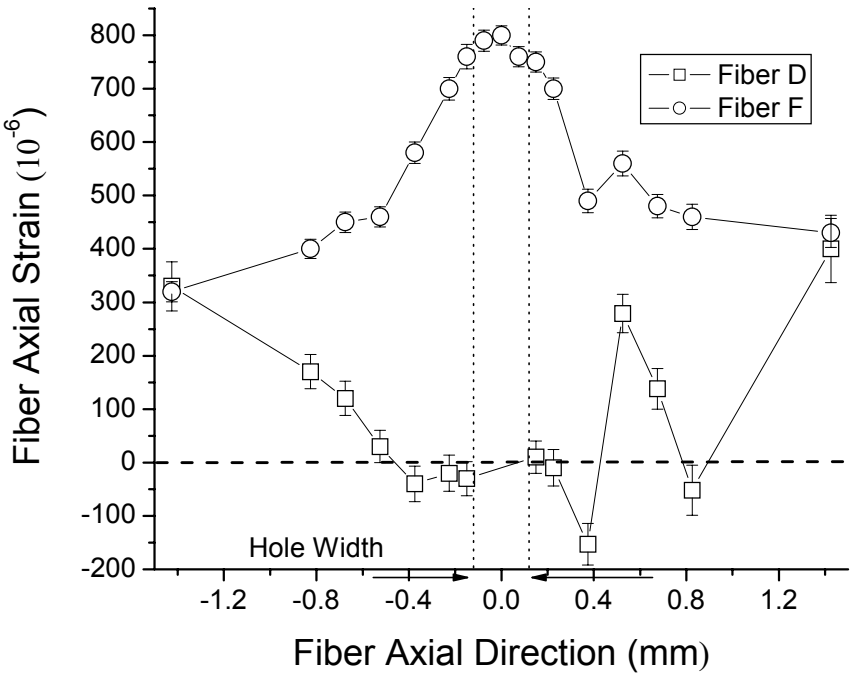

Figure 5-45 Change in axial strain for fibers *D* and *F*. The axial strain does not change near the free surface for the cut fiber *D*. In contrast, the intact fiber F shows a significant change in residual strain upon unloading due to permanent deformation in the matrix.

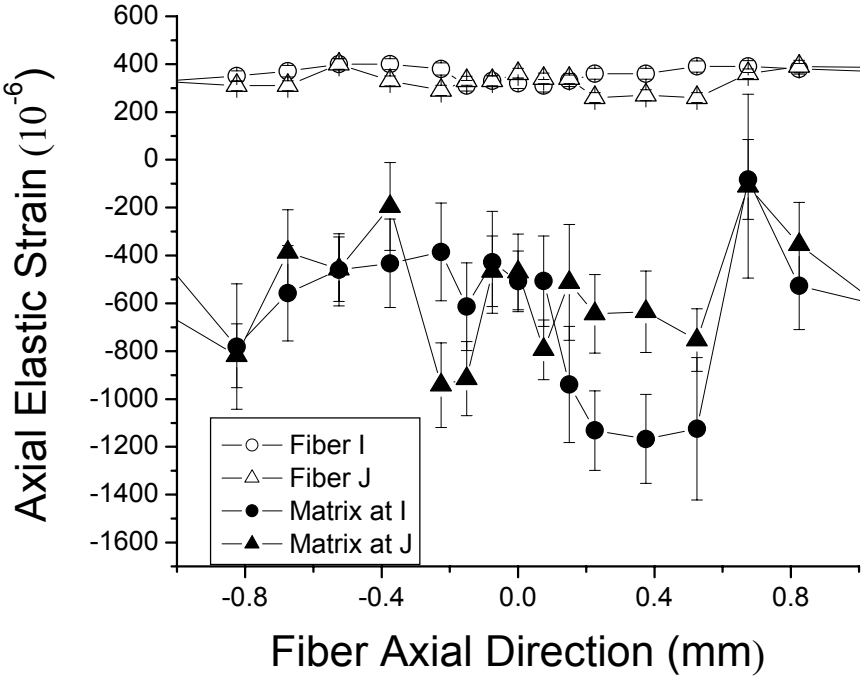

Figure 5-46 Change in axial strain for the two fibers furthest from the break. Change in the axial matrix strains at these fiber locations is shown as well.

Fiber *G* is a second nearest neighbor to the naturally broken fiber *E*. Some permanent deformation related specifically to the transfer of load is expected in this fiber. Though this is observed, a position near the crack plane shows no change in residual axial strain (-20 με, less than the error bars, Figure 5-47). Since the fiber is elastic, the lack of change in strain requires the immediate neighborhood around this region of the fiber did not permanently deform. However, the matrix in this neighborhood showed the opposite behavior with an abrupt increased change in residual stain associated with an exaggerated permanent deformation. One way to reconcile this observation is to relax the assumption of an intact interface at this specific region, then—since its neighborhood cannot change—the fiber residual strain cannot change and the stress which would have been

carried by the fiber was transferred to the matrix adding to the observed local increase in deformation.

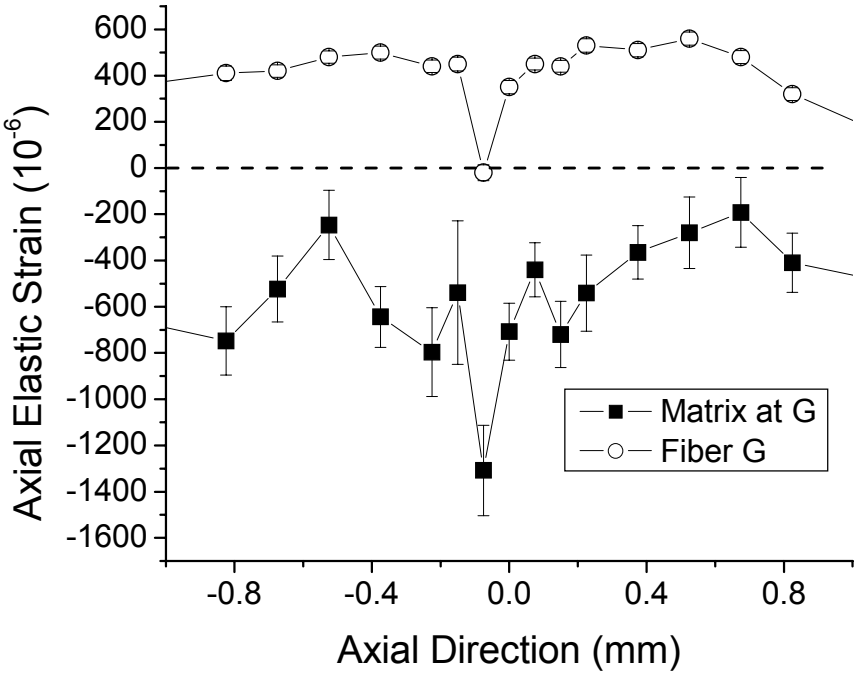

Figure 5-47 Change in axial elastic residual strain for fiber *G*. Though similar to the above fibers far from the break, the position sampled to the immediate negative side of the crack plane showed no change in strain—the sign of a poorly bonded interface. Adding support to the observation, a local increase in plastic deformation was observed at the same location through the change in matrix strain.

The change in residual strain revealed permanent deformation in the second damaged composite. The damage evolution was revealed in two dimensions providing a window into the damage evolution of the composite as a whole. The most significant changes were due directly to the presence of the hole and the resulting break in fiber *E* which naturally occurred during the application of load. Some fluctuations in the change of fiber and matrix strains as a function of the fiber axial direction were observed and may be attributed to plastic anisotropy in the matrix (Section 4-3). Notably, fiber *G*, the

second nearest neighbor to the break, showed a region that did not appreciably change residual strain. Since the matrix at this region deformed, the lack of change points to a weakening in the interface at this point along the fiber.

5-7. *Comparison with Matrix Stiffness Shear Lag Model*

The Ti-SiC composite described in Section 4 was chosen as a model composite for comparison of the strains in each phase predicted by the MSSL model (Section 3-2) with strains predicted at applied stress. Based on the geometry of the Ti-SiC composite the stiffness ratio, ρ, was interpreted and calculated several different ways. For all cases, the elastic constants employed were E_m = 125 GPa, and E_f = 393 GPa [54]. The matrix shear modulus, G_m, was calculated, assuming elastic isotropy in the matrix, using $G_m = E_m / 2(1 + \nu_m)$, with the matrix Poisson's ratio of $\nu_m = 0.31$ [54].

Two initial cases of crack configuration were considered (Figure 3-3). Since the matrix is assumed to sustain longitudinal tensile forces, the MSSL model will differentiate between a transverse matrix crack extending from the fiber break to the next fiber, case (ii), versus no crack extension from the fiber break into the matrix, case (i). For case (i), only the matrix regions between broken fibers are broken. For case (ii), in addition to those broken in case (i), the two "crack-tip" matrix regions between the last broken fiber and first intact fiber are broken. The model assumes the matrix and fiber fractures are infinitely sharp. Since, particularly in the etched composite, the damage region in the matrix is neither wholly intact nor completely broken, both cases were compared to the data.

Figure 5-48 displays MSSL model predictions and normalized experimental strains from fibers obtained at two of the initial applied stresses for the first damaged composite. The fiber strains are normalized with respect to the far-field strain. As ξ approaches +/-3, the far-field strain dominates (see Figure 5-48). Though any fiber or matrix index

location with $|\xi| > 3$ could have been designated the far-field strain, to reduce statistical error, the far-field strain was determined by averaging the strain measured for $|\xi| > 4$ at each fiber and matrix index. Some variations between these far-field strains are expected from the local strain variations due to grain-to-grain interactions (Section 5-5 and 5-2 and [57, 85]). However, the localized strain variations did not prevent validation of the model since the shape of the model was captured in the experimental results.

At the crack plane, $\xi = 0$, the maximum strain divided by the far-field strain, or Strain Concentration Factor (SCF), of the first intact fiber provides an efficient test of the model's assumptions. For a given number of fiber breaks, the shape of the strain profile and the SCF significantly differ between the two cases, (i) and (ii). With an intact matrix, less load transfers to the fiber, but with a broken matrix, the load formerly carried by both the broken fiber and the broken matrix is shed to the surrounding intact fibers. The MSSL model predicts an intact matrix at the crack tips leads to a strain profile where the maximum SCF in the first intact fiber is slightly displaced from the crack plane (Figure 5-48 (c)). The fiber strain profile is governed by the difference between the decay of the shear strain and the axial displacement of the matrix. The axial displacement dominates near the crack plane giving a slight rise in fiber stress from the crack plane (see ref. [34] for more discussion). When more fibers are broken, the MSSL model also predicts an increase in the SCFs and a broadening of the strain profiles. This enlarges the area affected by the damage zone.

Figure 5-49 depicts the axial matrix strains and MSSL model predictions for the matrix. The matrix strain profiles show the matrix carries some load. In addition to the matrix regions at the crack tips, the region between the two broken fibers supported some

load. The break in fiber 0 was artificial. Its finite width appears in the experimental strains delaying its recovery to the far-field strain. However, since fiber +1 broke *in situ*, its natural decay length is preserved (Figure 5-48). The error bars plotted on the graphs were determined by a 95% confidence limit to the center of peak position.

The interpretation of the matrix strains is less certain due to insufficient sampling statistics. While experimental errors of less than 200 με were found in the fibers and some regions of the matrix, strain uncertainties varied in the matrix, some greater than 700 με. The relatively large matrix grain size compared to the sampling volume meant not every location had diffracting matrix grains (the "graininess" problem). At a given location, only a few grains are likely to contribute to the intensity of the (10·2) reflection (Section 5-3). As a result, the (10·2) intensity varies tremendously directly affecting error in its peak position (Figure 5-16, and Figure 5-49). This condition led to the later use of the image plate to resolve the matrix strains.

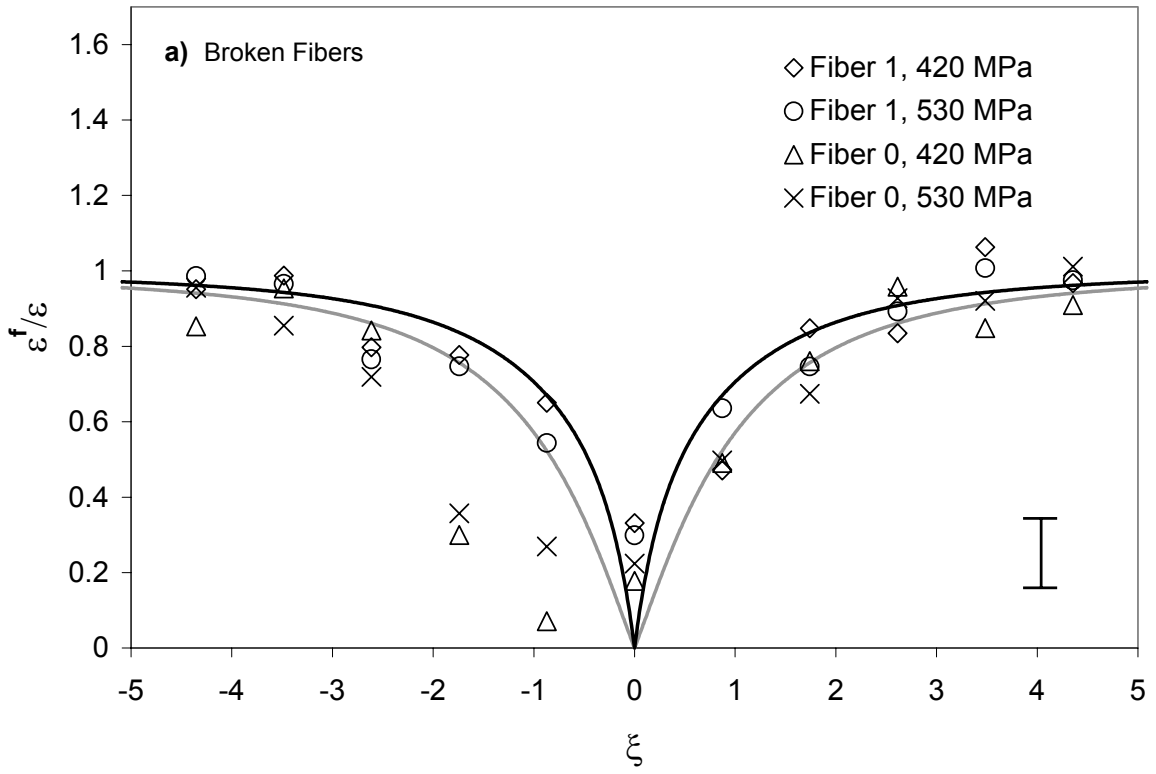
a) Broken Fibers
Fiber 1, 420 MPa
Fiber 1, 530 MPa
Fiber 0, 420 MPa
Fiber 0, 530 MPa
$\varepsilon^f/\varepsilon$
ξ

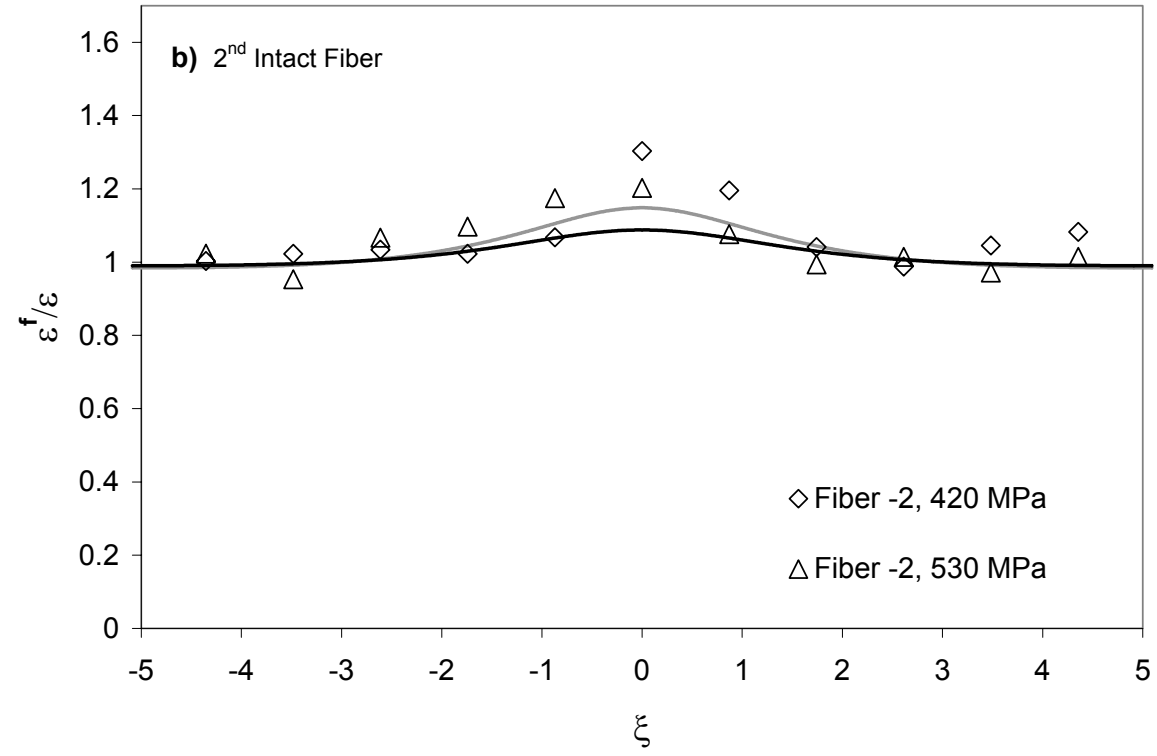
b) 2nd Intact Fiber
Fiber -2, 420 MPa
Fiber -2, 530 MPa
$\varepsilon^f/\varepsilon$
ξ

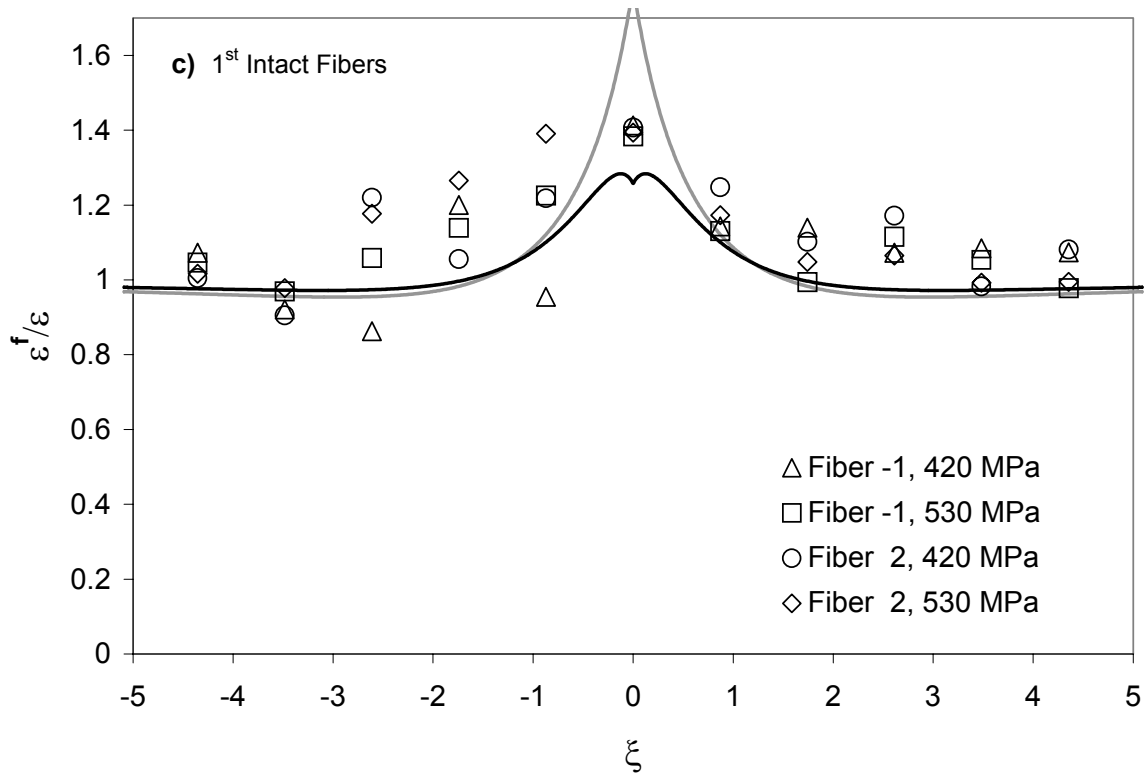

Figure 5-48 Comparison of strains from the MSSL model predictions (case (i) the black line and case (ii) the grey line) and XRD data from fibers (symbols) in the first damaged composite: (a) The two broken fibers; (b) the second intact fiber; (c) first intact fibers. The applied tensile stress decayed from 430 to 410 MPa for one applied stress and 530 to 540 MPa for the other applied stress shown. The model calculations were performed for $\rho = 0.591$. Strains were normalized with respect to the averaged applied far-field value (the average strain for all $|\xi| > 4$). Particularly for (c) the first intact fiber, case (i) with two broken fibers (0 and +1) gives the best agreement with model predictions. The expansion of the profile for fiber 0 is due to the width of initial damage in the fiber.

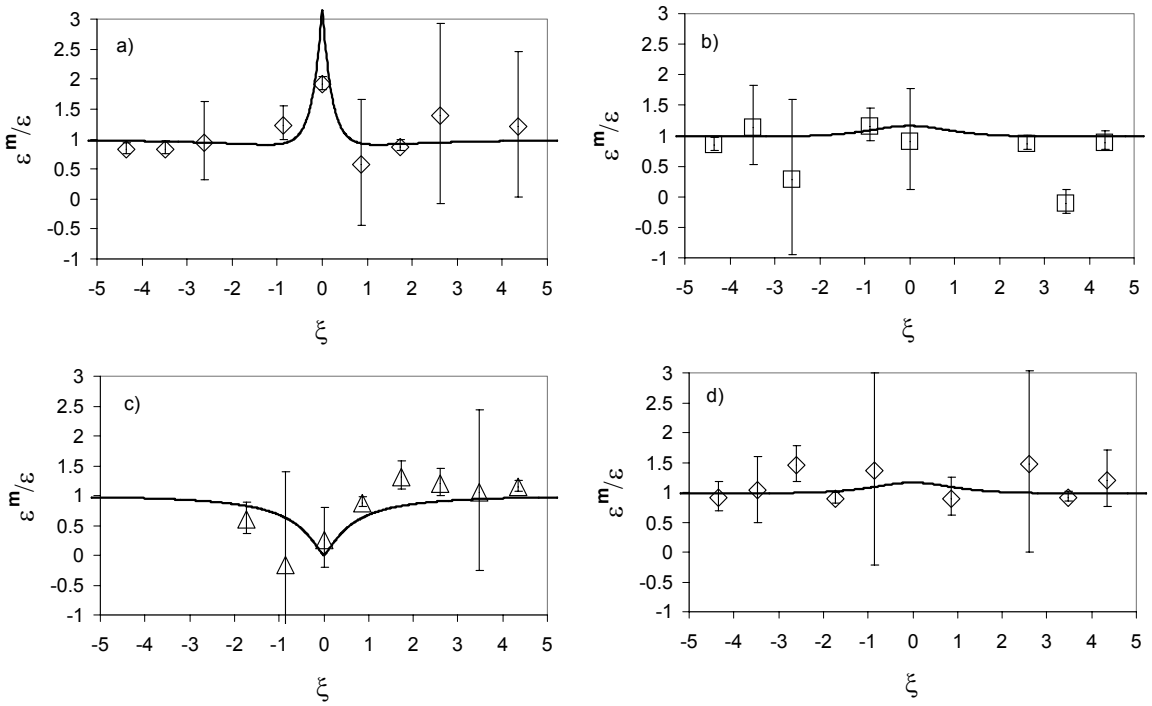

Figure 5-49 Comparison of normalized strains from MSSL model predictions and XRD data from the matrix in the first damaged composite for case (i)—intact matrix at crack tips. (a) Depicts the matrix region between the two broken fibers (0 and 1), (b) the matrix region between an intact and broken fiber (–1 and 0), (c) the matrix region between two intact fibers (–2 and –1), and (d) also a region between an intact and broken fiber (2 and 1). The applied tensile stress under constant displacement drifted from 450 to 430 MPa. The model calculations were performed for $\rho = 0.591$. Strains were normalized with respect to the applied far-field value, $\varepsilon^m = 2340$ to 2240 με. Elastic strains for each region of the matrix examined are plotted against the best-fit model predictions for that region. Grain-to-grain strain variations are significant here as few grains represent each position.

Comparison of the MSSL model predictions to the strains in this first composite, damaged by etching the matrix, showed potential for further application of the MSSL model for other damage configurations. One strength of the model is its ability to predict strains due to a large number of fiber breaks. A reasonable damage configuration to compare to the model could include 10 to 50 broken fibers across a wide laminar

composite. However, the method used to record these strains requires significant blocks of beam time limiting the area of the composite which may be analyzed.

The composite damaged with the hole allowed a second test of the MSSL model for a new damage configuration. The most significant improvement for the second test was the introduction of the image plate as an area detector. The image plate reduces the time required to measure the strains and, as will be shown, by including more grains in the diffraction pattern, the image plate allowed the matrix strains to be resolved. Other improvements included a stiffening of the grips to reduce load drift during the analysis along with allowing greater applied loads to the composite. The maximum applied stress was further increased through more stringent control of the composite cross section using EDM to machine the composite and tabs as described in the previous chapter, Section 4-1. Finally, by using the hole instead of the etched matrix, the geometry of the damage could be more easily incorporated into the model.

To account for the missing matrix and adjacent fiber sections which were cut with EDM in the MSSL model, breaks were stacked along the fiber axial direction (ξ) for the measured length of the hole. Nine equally spaced breaks were placed between the outer dimensions of the hole in fiber *D* and matrix *d* (between *D* and *E*). The natural break in fiber *E* was modeled as a single break.

Section 3-2 compares three significantly different methods of interpreting the composite geometry. As shown above when compared to the model, the first experiment on the etched composite was able to discriminate between these interpretations but left unanswered what range of values was best suited for the resulting interpretation. As was shown in Section 5, the second experiment on the composite with a hole provided more

strain and spatial resolution than the first. This increased resolution facilitated a more detailed analysis within the preferred geometric interpretation described above. Thus, the sensitivity of ρ and δ to the following variables for conversion to several possible two-dimensional projections of the composite geometry were also considered.

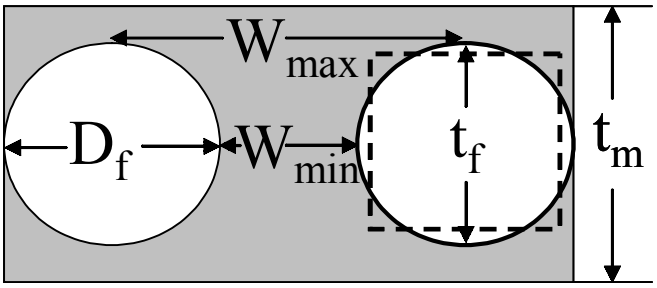

Figure 5-50 Illustration of the interpretations of composite geometry relevant to the MSSL model. Since the model only considers matrix between the fibers and the real composite has matrix all around the fibers, the definition of the width of matrix between the fibers *W* has multiple interpretations. One simplification of the geometry assumes the fiber cross section is square (dashed line). This simplification conveniently results in constant width between the fibers throughout the thickness.

For the possible values of δ and ρ, A_f was left at the measured value (32% area fraction), first simulating a circular cross section for the fiber, and second simulating a square cross section for the fiber (as in Figure 5-50). However, A_m is a function of thickness, *t*, which was allowed to vary in order to determine the relevant thickness which should be input to the model for the composite. Two scenarios from a range of possible predictions are described below and provide reasonable extremes for possible projections of the geometry.

1) First, a range of thicknesses was explored according to the limits described in Figure 5-50. The area of the matrix, A_m, depends on the prescribed matrix thickness. The area of the fiber, A_f, depends only on the diameter of the fiber,

D_f. Therefore, through Eq. (3-1) and Eq. (3-2), both ρ and δ depend on the ultimate thickness chosen to represent the composite thickness in the model, t. Let $t = t_m$. Then, making the appropriate substitution for the fiber and matrix area in Eq. (2):

$$A_f = \pi \cdot \left(\frac{D_f}{2}\right)^2 \qquad A_m(t_m) = t_m \cdot (W + D_f) - A_f$$

and keeping all other variables constant, ρ will decrease with t_m according to:

$$\rho(t_m) = -E_m \cdot \frac{\left(-4 \cdot t_m \cdot W - 4 \cdot t_m \cdot D_f + \pi \cdot D_f^2\right)}{E_f \cdot \pi \cdot D_f^2} \tag{5-2}$$

which is a linear function with respect to matrix thickness. An upper limit for this possible interpretation with t_m = 200 μm results in a load sharing parameter, ρ, of 0.667 and characteristic decay length, δ, of 252 μm (from Eq. (3)). A reasonable lower limit with $t_m = \sqrt{A_f}$ mm gave ρ = 0.290 but slightly increased δ.

Interpretation 1) gave reasonable intensities for the SCF, but, as will be shown, the resulting decay length was too short. While this may be due to other factors, such as deformation in the matrix, an increase in W will also extend the decay length. Additional reasonable interpretations of the geometry which extended the decay length were also considered.

2) The second reasonable interpretation of the geometry involved increasing the average width between fibers, W. Here the area fraction was again left at the measured value, but since the X-ray gage volume is rectangular and integrates through the depth of the composite, an average fiber width was approximated by assuming a square cross section of length $\sqrt{A_f}$ on each side (see dashed box in Figure 5-50). The thickness was again varied, but since the fiber centers were kept a constant distance apart, W increased 32% compared to the minimum value for W used in 1). In this second interpretation, the results for ρ are the same as the values obtained in 1). However, δ increases compared to 1) with its maximum value obtained as thickness, t, decreases. Thus, a lower limit of the model thickness, $t = t_f = \sqrt{A_f}$, was also a reasonable choice for comparison to the strains. The corresponding characteristic decay length, δ (367 μm), was included in the second set of model comparisons.

The effect of adjusting the other parameters, for example: fiber diameter, distance between fibers, etc., was also considered, but improvements in the load sharing parameter and the decay length were not realized within reasonable interpretations of the real laminar geometry. As shown below, the two extreme, yet reasonable, interpretations described above result in similar predictions.

Figure 5-51 displays the MSSL model predictions from 2) above and normalized applied experimental strains from fibers obtained at the applied stress. While the assumptions in 2) prove better than 1), in Figure 5-51, the MSSL model predictions

corresponding to 2) underestimate many of the experimental strains for the intact fibers. The strain in each fiber is normalized with respect to the far-field strain, which is approximated by the strain measured at the point in the same fiber 10 fiber diameters from the break. The larger strains in the intact fibers than predicted show stress was transferred from deformation in the matrix. As observed from the change in residual strains (Section 5-6), here fiber *G* also shows signs of possible debonding near the crack plane.

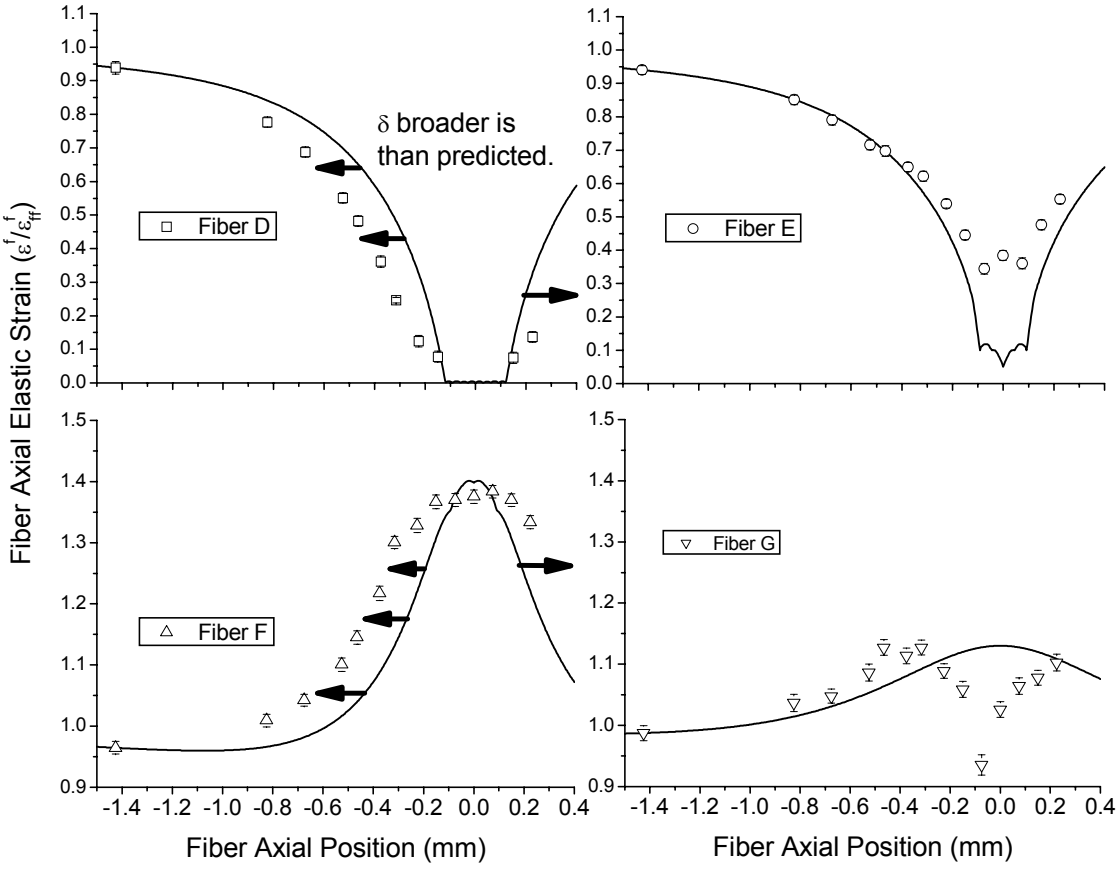

Figure 5-51 Normalized relative strains in the fibers around the hole from the 850 MPa maximum applied stress to the composite (symbols) compared to the MSSL model predictions for the second geometrical version of the model above (lines). More stress is transferred to fibers *F* and *G* than predicted by the MSSL model which is due to plastic deformation in the matrix (see next figure).

Observations of the matrix strains confirm the matrix permanently deformed under stress (Figure 5-52). Along with the FEM predictions (Section 3-1), the macroscopic analysis of the composite (Section 4-5) shows axial plastic strain is expected in the matrix for applied stresses greater than 700 MPa. While other factors such as interface debonding cause stress transfer from matrix to fibers, global yielding is small at this applied stress, so plastic strain in the matrix may be the sole mechanism of the stress transfer. Accounting for this plastic strain would require a new micromechanical model.

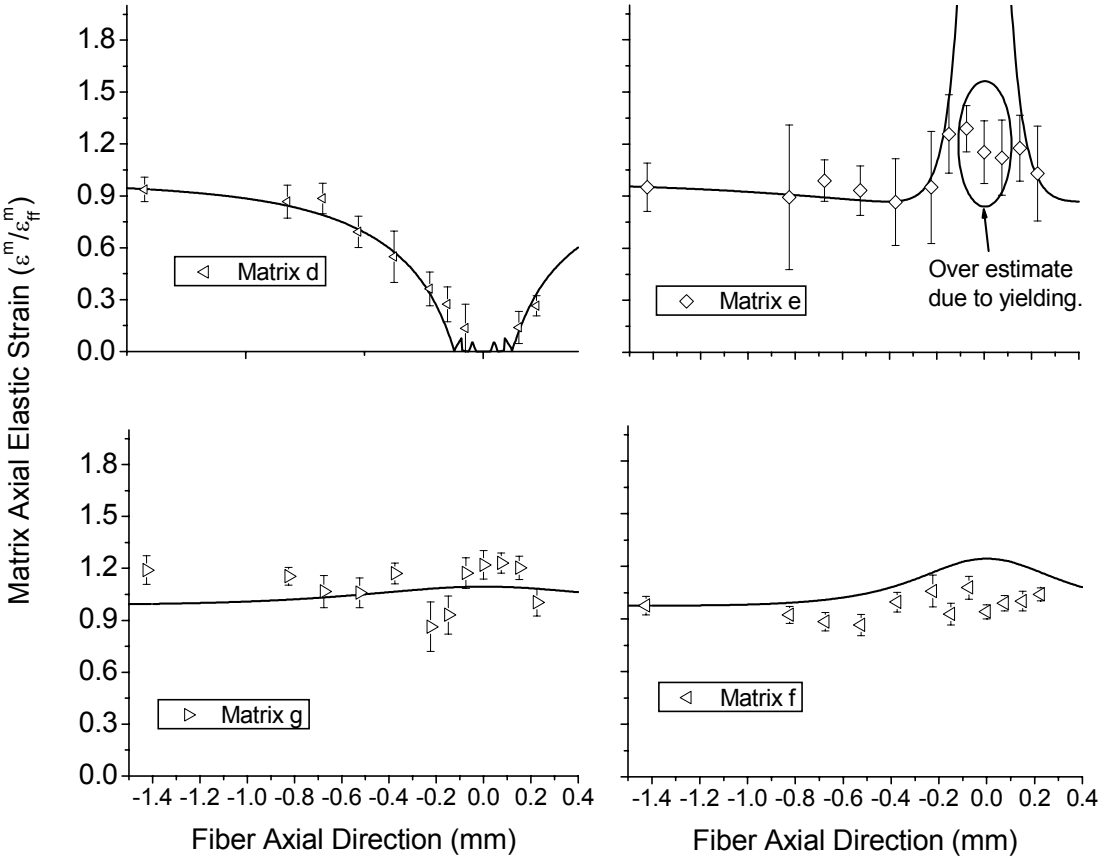

Figure 5-52 Normalized relative axial strains in the matrix from 850 MPa maximum applied stress to the composite around the hole. The MSSL model predictions for the second interpretation ($\rho = 0.290$) are shown (lines) compared to the measured strains (symbols). At this applied stress the matrix has begun to yield, particularly near stress concentrations as would be found by the hole in "*e*". The normalized matrix strain never exceeds 1.3. Yielding begins at the interface and transfers load to the fibers (Figure 5-49).

Results from a single fiber composite analysis have shown that the residual strains evolve due to plastic strain upon loading in a manner similar to the evolution seen here [29]. The same analysis showed that, even over multiple cycles, if the applied stress is not increased over an initial maximum applied stress, the residual strains and maximum strains in each phase do not change appreciably for each cycle. Thus, when the composite was unloaded, the observed change in strain may be assumed entirely due to decreasing elastic strains. For the Ti-SiC composite, much less plastic strain was applied than to the before mentioned MMC, so considering the results from single fiber MMCs, the unload step may be assumed entirely elastic. With this assumption, the unloaded strains in the Ti-SiC composite may be appropriately simulated using the elastic MSSL model.

Subtracting the final residual strains from the strains at applied load provides the change in strain observed in the unload step of the composite. These strains show many features in common with the strains predicted using the MSSL model allowing a test of the possible geometrical assumptions put forth above. Figure 5-53 and Figure 5-54 show the normalized change in fiber strains from the unloading step in the composite compared to the model. Figure 5-55, Figure 5-56, and Figure 5-57 show the normalized change in matrix strains from the unloading step also compared to the model. The fit improves with the choice of geometric parameters which assumes the fiber cross section is the same as the model (choice 2 above), rather than the cylindrical cross section. The improvement is due both to the increased stress transfer due to the smaller, ρ, and the longer decay length, δ. Since the larger W and smaller t favorably affect ρ and δ, the true distance

between fibers is an overestimate of *W* for cylindrical fibers approximated by the model, and the thickness of the composite is less important than the fiber diameter in determining the micromechanical response to damage. As can be seen from the figures, the differences between the two predictions are slight. Even with the reduced errors from the HEμXRD[2] analysis such a selection between initial assumptions is somewhat subjective.

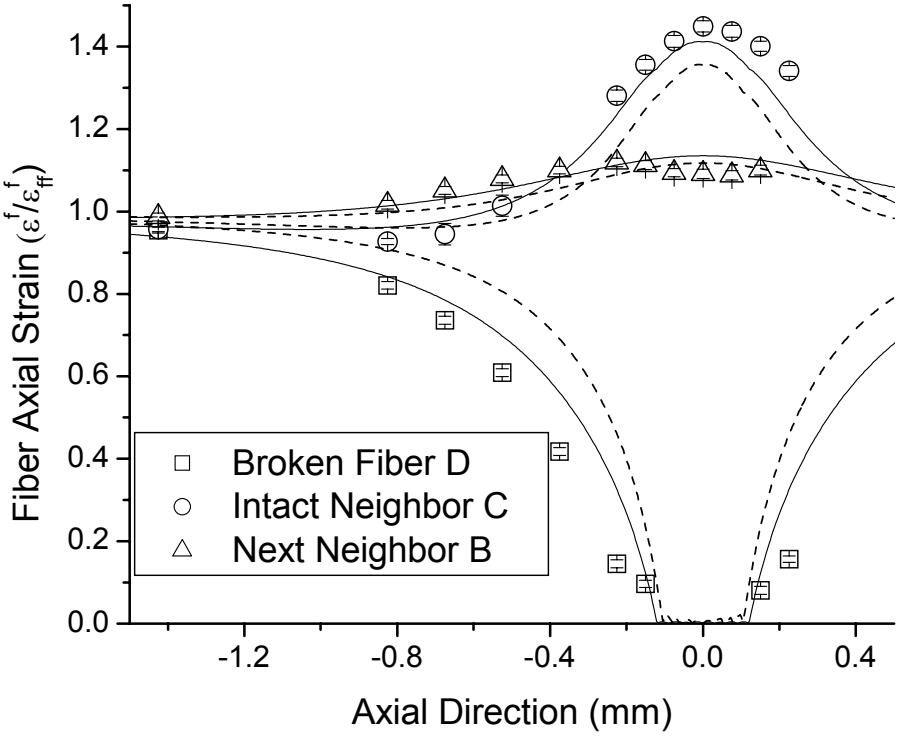

Figure 5-53 A comparison of the MSSL model predictions (lines) for the unloading fiber strains in the second damaged Ti-SiC composite (with a hole) for fibers *B*-*D* (symbols). The hole in fiber *D* was approximated by a series of breaks. The overall fit improves by averaging the distance between the fibers for *W* and reducing the thickness in the model to the average thickness of the fiber (solid line). The dashed lines depict the model predictions if the minimum distance between the fibers is used for *W* and the matrix thickness is used for *t*.

The strains in fiber *C* are slightly larger than the predicted values. This is due to two factors. One, the fiber next to *C* (unlike the fiber next to *F*) is cut (Figure 5-3) such that more strain will be transferred to fiber *C* than *F* (Figure 5-54). Two, the matrix next to *C* is also damaged, but is carrying load as can be seen in Figure 5-55. However, due to the damage, the matrix in column *c* narrows approaching the crack plane, a geometric detail not accounted for in the model, so more load should be transferred to *C* than is predicted. Comparison to case (ii) where the matrix is broken in column *c* (not shown, for example, see Figure 5-48), clearly shows the effect the lack of matrix has by dramatically increasing the load in an intact fiber next to a broken matrix column. Since the matrix is not broken, but is damaged, such a dramatic increase is not seen here, thus, case (i) is a better choice for the particular damage configuration in this composite.

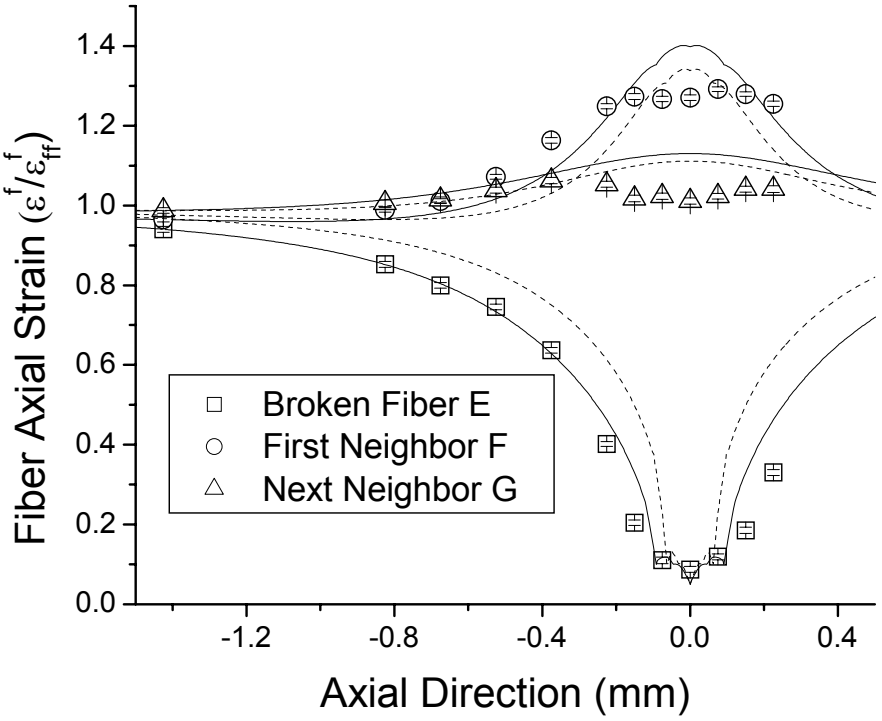

Figure 5-54 A comparison of the MSSL model predictions (lines) for the unloading fiber strains in the second damaged Ti-SiC composite, with a hole, for fibers *E-F* (symbols). Fiber *E* broke naturally but its strains show evidence of the neighboring hole. Two extremes of the geometry provide the two model prediction shown ($\rho = 0.290$ (solid line), $\rho = 0.667$ (dashed line)).

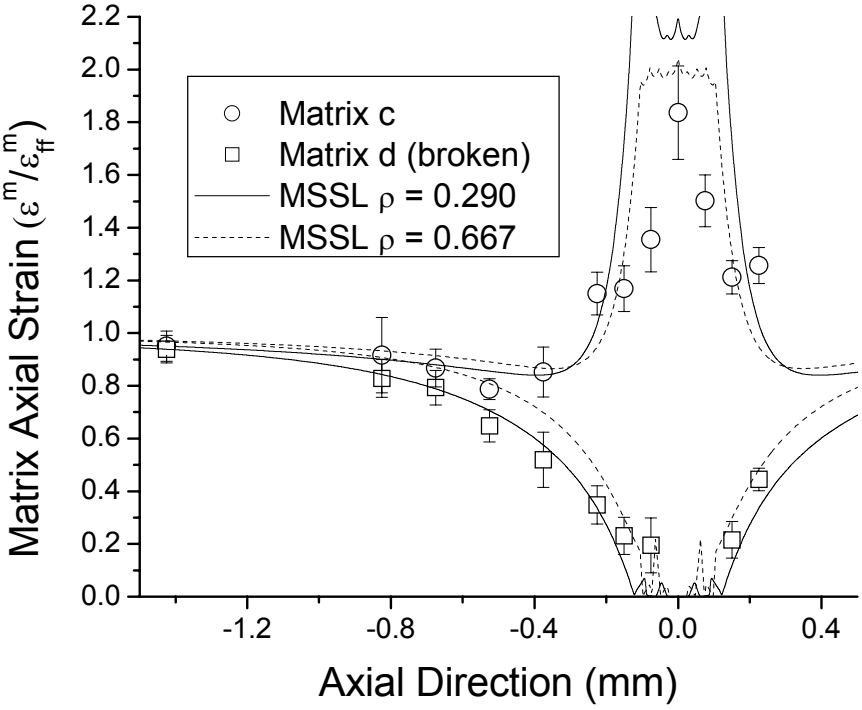

Figure 5-55 A comparison of the MSSL model predictions (lines) for the unloading matrix strains (symbols) in the Ti-SiC composite with a hole. The dashed lines depict the model predictions if the minimum distance between the fibers is used for *W* and the matrix thickness is used for *t* ($\rho = 0.667$). Overall the fit improves by averaging the distance between the fibers for *W* and reducing the thickness in the model to the average thickness of the fiber (solid line, $\rho = 0.290$). Matrix *c* is damaged near the hole contributing to the strain falling short of the model prediction.

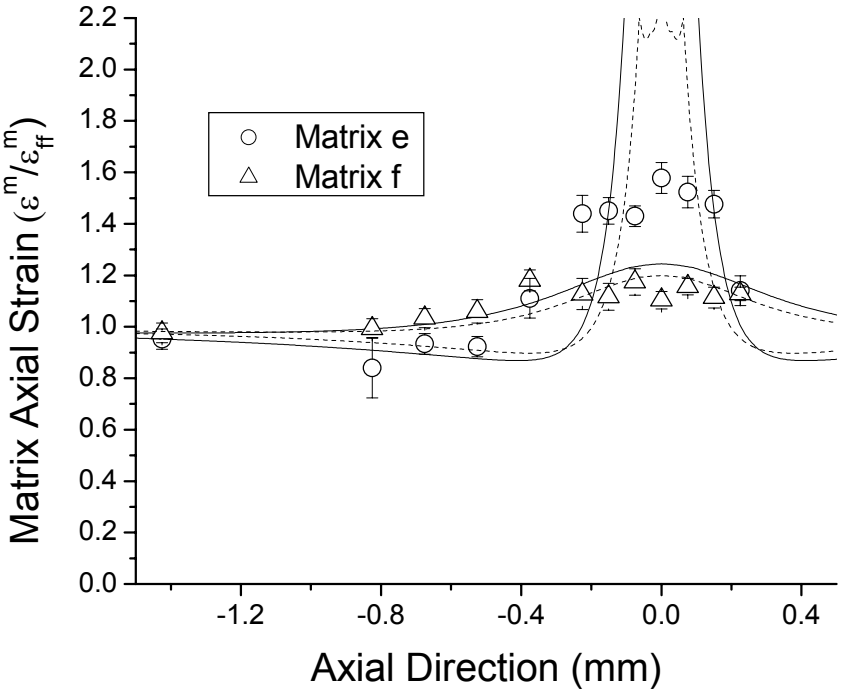

Figure 5-56 A comparison of the MSSL model predictions (lines) for the normalized unloading matrix axial strains (symbols) in the Ti-SiC composite with a hole. As above, the dashed lines depict the model predictions if the minimum distance between the fibers is used for *W* and the matrix thickness is used for *t*. Again, the overall the fit improves by averaging the distance between the fibers for *W* and reducing the thickness in the model to the average thickness of the fiber (solid line). Though possibly influenced by the debond in fiber *G* (Figure 5-54), matrix *e* strains fall short of the model prediction.

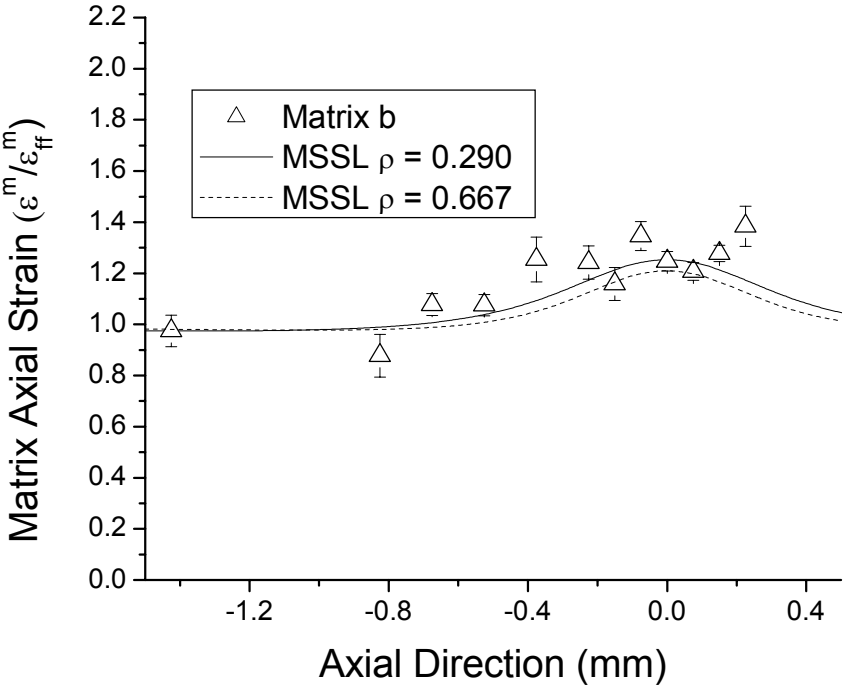

Figure 5-57 For completeness a final comparison of the MSSL model predictions (lines) for the unloading matrix strains (symbols) in the Ti-SiC composite with a hole. As above, the dashed line depicts the model predictions if the minimum distance between the fibers is used for *W* and the matrix thickness is used for *t* and the solid line depicts the fit for averaging the distance between the fibers *W* and reducing the thickness in the model to the average thickness of the fiber. The general trend depicted by the model is observed.

As discussed in Section 2-2, the error estimation assumes Gaussian error distribution as standard in least square fitting. The resulting error bars are shown in each graph. For the fibers, the symbols are generally larger than the numerical error given by the strain analysis. However, non-numerical errors are not shown and would increase the uncertainty to some degree. The difference in error between the phases is primarily due to the number of grains averaged by the beam. For the fiber, with its small grain size, hundreds of millions of grains are irradiated by the beam. For the matrix, with its larger

grain size, far fewer grains are irradiated by the beam. Thus the fluctuation due to discontinuous strains contributed by individual grains becomes much stronger making the average matrix strain at each point less certain.

In summary, considerable agreement is observed between the MSSL model and the measured elastic strains in the broken and neighboring intact fibers generated by two fiber breaks. Comparisons between the model and the data demonstrate the importance of accounting for the matrix stiffness and shear in load transfer and show that the matrix within and around the damage zone sustained axial load. For two different damage configurations and a large range of applied strains, case (i) (which models intact matrix at the crack tips) is clearly the best choice for the composite. The diameter of the fibers was shown a more significant parameter than the matrix thickness for a matrix which was thicker than the fiber diameter. This result affects the calculation of the load sharing parameter ρ, Eq. (2-1) and characteristic decay length δ, Eq. (2-3). The best value for ρ found for this composite was 0.290, which required an averaging of the distance between fibers in the out-of-plane direction and consideration for the fiber diameter in the matrix thickness.

6. Conclusion

High-energy two-dimensional X-ray microdiffraction (HEμXRD^2) and low-energy X-ray microdiffraction were used to observe strains from both constituents of a Ti-matrix/SiC-fiber composite. The strains from HEμXRD^2 provided a revealing picture of damage evolution at the scale of microstructure and enabled *in situ* studies under applied stress. The technique provides spatially resolved *in situ* mechanical information in a MMC not available through any other method and an opportunity to study an entire body of composites for comparison to relevant micromechanical models. These models, when validated, provide a predictive capability for composite performance and lifetime.

6-1. *General Conclusions*

Using the two X-ray microdiffraction methods, first using a point detector and second an area detector, the phase-specific *in situ* residual and applied tensile strains in the MMC were investigated. Of the two methods, HEμXRD^2 proved the most valuable for the identification of global yielding in the matrix since the two-dimensional strain tensor could be observed at each load. Particularly the deviatoric strain measured directly by a fit to the diffraction ring, provided the necessary information to identify deviation from linearity in the ε_{11} (axial) and the ε_{22} (transverse) strains. Both X-ray methods produced results consistent with a continuum three-dimensional finite element model (FEM).

At the microstructural scale, a shear lag model [34], modified to account for the elastic stiffness of the matrix, was fit to the measured elastic strains in the broken and neighboring intact fibers generated by two fiber breaks. Comparisons between the model

and the data demonstrate the importance of accounting for the matrix stiffness and shear in load transfer and show that the matrix within and around the damage zone sustained axial load. The diameter of the fibers was shown a more significant parameter than the matrix thickness for a matrix which was thicker than the fiber diameter. This result affects the calculation of the load sharing parameter ρ, Eq. (2-1) and characteristic decay length δ, Eq. (2-3), critical parameters determining the normalized predictions of the model.

The best value for ρ found for this composite was 0.290, which required an averaging of the distance between fibers and consideration for the fiber diameter in the matrix thickness. The damage induced in the composite, which relaxed thermal residual strains in the fibers, promoted failure of the neighboring fibers. The matrix adjacent to a fiber break was clearly shown to carry load discriminating the choice of case (i)—intact matrix at the crack tip—for the model assumptions. The measured strains also revealed deficiencies in the shear lag model. Specifically, the model lacks a proper treatment of thermal residual stress as well as plastic deformation in the matrix.

The results further show the irradiation of a small number of grains (roughly 60 grains in a matrix region for a 90 x 90 μm^2 beam) provides strain measurements comparable to a continuum mechanical state in the material. A result which is surprising since the number of grains diffracting is a subset of the grains irradiated [86]. It is the collection of the entire Debye-Scherrer ring, with correct accounting for the deviatoric strain, which allows strain measurements from such a small number of grains. As was shown, an analysis using a point detector that does not take advantage of the two-

dimensional nature of the diffracted strain information is limited in its application as the beam sizes approaches the grain size.

Due to the CTE mismatch, average thermal residual stresses of −740 MPa in the fibers and +350 MPa in the matrix were found along the fiber axes. Although, using conventional mechanical testing, the global yielding of the Ti-SiC composite is not detected until at least 700 MPa applied stress; XRD strains reveal that local yielding occurs as early as 500 MPa.

In the residual stresses and under the applied tensile load, plastic anisotropy was observed in the matrix. It provides a source for the observed grain-to-grain strain variation. The intergranular strains in the Ti matrix were observed to vary as much as 50% even far from the damage region. In spite of this dramatic variation, the two-dimensional XRD technique provided reliable information from the matrix. In sum, this investigation establishes HEμXRD^2 as a powerful method to collect multidimensional strain information from all phases of a composite at the scale of the microstructure, and it opens the window for validation of advanced micromechanics models which simulate damage evolution and predict lifetime of composites.

6-2. *Future Work*

As part of an initial investigation to establish methodology and demonstrate feasibility, this work naturally leads to several directions of further study. From a mechanics perspective, a next step involves the prediction of plastic deformation in the composite under load. Extension of the MSSL model to include plasticity is already underway. The data collected by the methods described above is a first step toward validating results obtained from future models.

Using the bulk composite raw diffraction data (60 images vs. 1500 images for the microscale data) from the image plate, several mechanical treatments could be pursued. Not the least of these is an application of the Self Consistent Model (SCM) used for modeling plastic strain in a crystalline aggregate [87, 88]. The advantage here is two-fold. Information is potentially available from the matrix in all η from several reflections. And the grain size of the matrix is not so disparate from the fiber diameter to exclude use of the model. Though feasible, an SCM has not been developed to correctly treat the information available from an image plate; but, when it is available, the already collected images would allow a more precise determination of *in situ* matrix yield behavior, and account for the *hkl*-dependent elastic and plastic anisotropy.

The software to analyze two-dimensional strains is still in its infancy. Deficiencies in the current analysis method were given in Section 2-2. Because so much information is available from the diffraction ring, it will take time to implement and test improved software to analyze the strains. The data collected here can be used as a resource for this effort. In addition, an effort is underway to allow the calculation of strains in real time as the data is collected. This is a valuable exercise as it will allow decisions to be made at

the instrument based on, for example, the extent of load transfer, plastic yielding, and even error. (Percent error decreases with stress, but many studies want to first observe elastic strains before considering plastic deformation. A real-time knowledge of the strains would provide an obvious improvement for such studies.) Even with an advanced strain analysis, there is no replacement for archiving the raw image files. The texture information alone can require several different procedures to unearth a wealth of structural information. This is particularly true for microbeam work as the grain-specific strains are revealed with, for example, a blob analysis [32] versus the average strains which become more apparent with a pseudo-rocking method [50]. Again the data collected here will be useful in simulations to develop a real-time analysis method.

Additional logical extensions of this work include application of this technique for the examination of the Ti-SiC composite and similar composites under even greater applied stress (1-1.2 GPa). This would be particularly useful if combined with an imaging method which identified natural breaks. X-ray microtomography has been shown to reveal natural breaks in SiC [81], so a possible next step would be to adapt an instrument which combines both imaging and strain measurement capabilities at the energies necessary for analysis of this composite system.

The Ti-SiC composite is ultimately intended for applications which require strength at elevated temperatures. High-energy X rays and thermal neutrons are well suited for high temperature work. Since they have good penetration ability and do not require large angular detection windows compared to low-energy X rays, the addition of a furnace to the sample environment is tractable. As this composite is so well suited to analysis at high energy, incorporating a furnace to measure creep, nonlinear CTE behavior, etc. with

the load frame is a further extension of the work presented here. Furthermore, ceramic matrix composites show promise for these applications as well as improved (and cheaper) versions of the monolithic Ti alloy [33]. The methodology for exploration of the mechanical properties could be developed on experiments with Ti-SiC and extended to these materials.

With the continuing advances in the field, the microbeam used here is becoming more common. Beam sizes less than a μm across were recently used to explore an MMC under load [89, 32]. Such dimensions allow never before seen examination of the interface properties as well as intergranular stresses [31, 32, 36]. The amount of information* and time required to make the three-dimensional analysis have slowed the progress in this direction but improvements on many fronts will soon make a three-dimensional full tensor stress analysis at the scale of a μm reasonably achievable. Combined with high-speed X-ray imaging, the tools becoming available are set to conquer the difficulties of measurements on the order of grain size, a worthy task to which this work has partially contributed.

*The study referred to here amassed 70 Gigabytes of data on a region less than $1/10^{th}$ the size in roughly 5 days as apposed to the 38 Gigabytes of information collected in 7 days of beam time with the Ti-SiC image plate study.

7. Appendices

7-1. *Appendix A.* Load Frame and Strain Gage Interface Code

LabView version 6.0.2 was used to program an automated computer interface which logged strain from up to 4 strain gages, the load from a load cell, and temperature. The hardware used was the NI USB-DAQ Pad connected to a SC-2345 signal conditioning block. Strain gage modules are available for the SC-2345 in Quarter, Half, and Full bridge formats. Each may be easily configured in with NI's Measurement and Automation Explorer package (MAX) sold with LabVIEW. The following describes the important subsets of the interface code such that future users could continue use of the program in other experiments. The LabView help documentation is extensive and the reader should refer it for programming assistance.

The front panel (user interface for the program) is as shown:

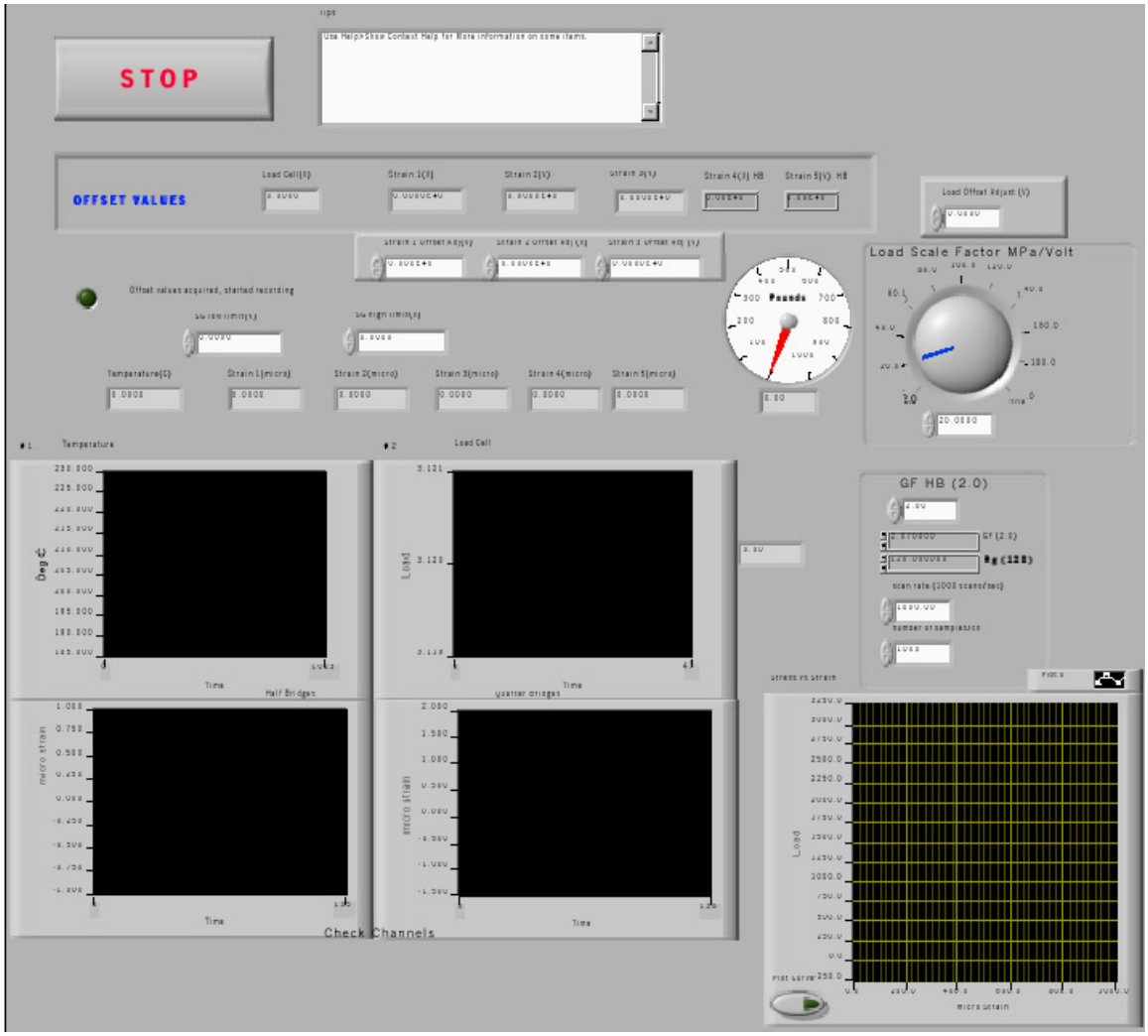

All incoming variables are displayed on the screen as a function of time. A right click on any graph button or dial will display help text for that item.

An overview of the block diagram is shown. The functions generally move from left to right. Initialization of the hardware and zero calibration of the strain gages occur outside of the while loop (large grey rectangle).

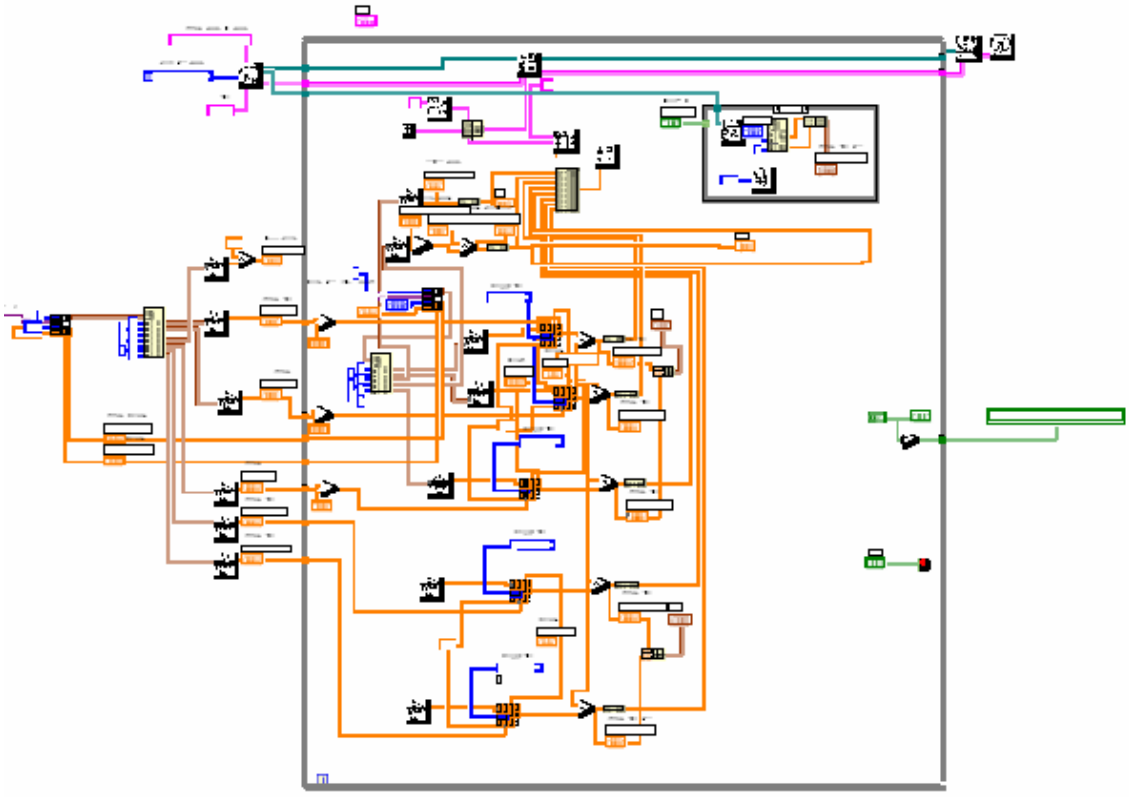

To acquire data from the hardware the following organization was used:

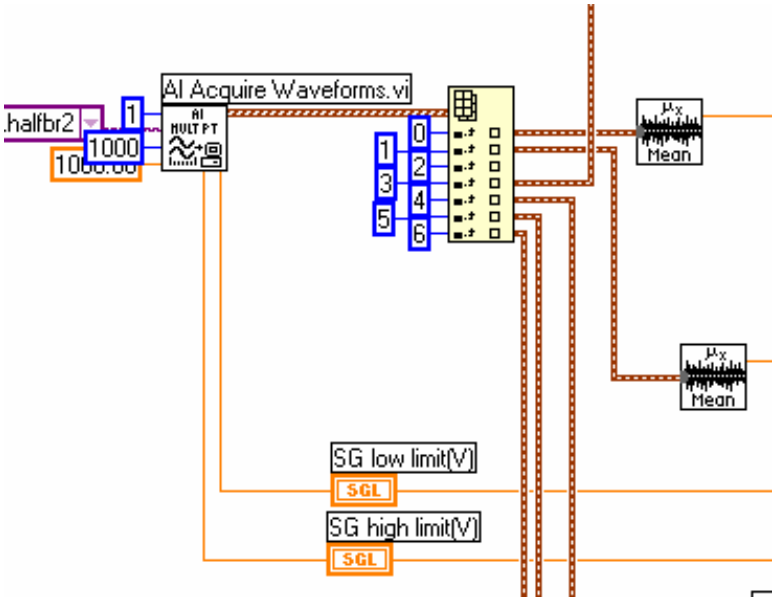

The variables input to “AI Acquire Waveforms.vi” were configured in MAX. Once configured and sensing the acquired data such as strain or temperature is assembled in an

array (brown wire shown). The array is indexed and each value is processed individually. Strains are best sent through an averaging routine such as Mean.vi, shown. Depending on the electrical setup averaging 1000 samples gives accuracy on the order of 10^{-6} strain.

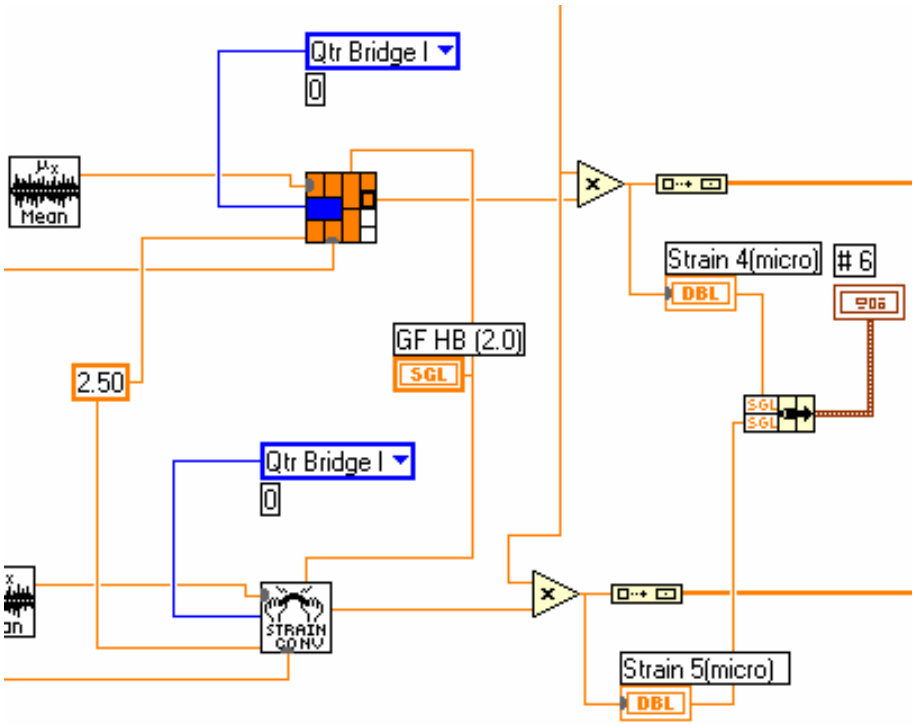

Once the resistance of the gage is collected by the quarter bridge module, it may be converted to strain using a routing as shown above.

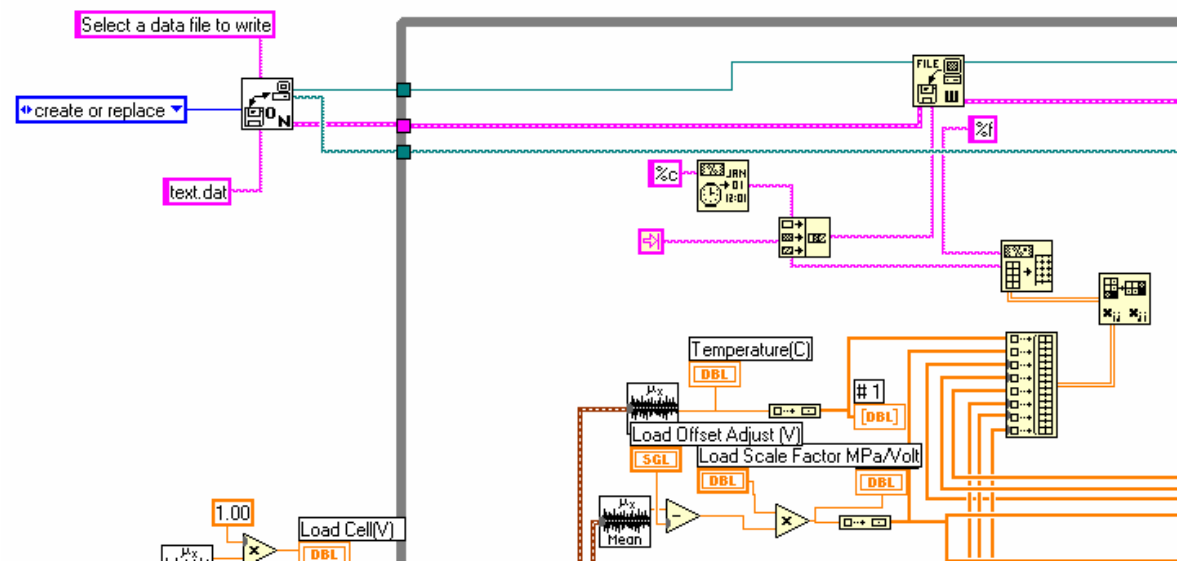

Finally the input variables must be logged to a text file. A standard text file logging routine is shown. The file is created before the while loop is started and kept open until the program is closed. Along with the averaged data, a time stamp is recored with each cycle of the while loop. Typical cycle times may be set on the front panel to 1 sec, 10 sec, etc. Also shown above is the method used to record the load cell voltage. Along with recording the raw voltage value, the load is scaled according to its calibration factor.

7-2. *Appendix B. Image Plate Calibration and Conversion Macro*

As referred to in the text (Section 2-2), the following macro was used to automate the conversion of digital image plate data for use with the MatLab analysis code given in Appendix C. The text of the macro includes the results of the calibration performed on the internal Si standard ensuring a consistent and meaningful conversion from radial to Cartesian coordinates. To conserve space the macro is presented in two-column format.

```
%!*\ BEGINNING OF MACRO FILE
%!*\
%!*\ This is a comment line
%!*\
EXIT
POWDER DIFFRACTION (2-D)
INPUT
#IN
O.K.
CAKE
INTEGRATE
TILT ROTATION
-30.33354
X-PIXEL SIZE
100.0000
Y-PIXEL SIZE
100.0000
DISTANCE
1110.956
WAVELENGTH
0.189725
X-BEAM CENTRE
1720.988
Y-BEAM CENTRE
1713.437
ANGLE OF TILT
-0.304665
O.K.
START AZIMUTH
0.0
```

END AZIMUTH

360.0000

INNER RADIUS

0.0

OUTER RADIUS

1700

SCAN TYPE

RADIAL

AZIMUTH BINS

120

RADIAL BINS

1700

CONSERVE INT.

NO

POLARISATION

YES

FACTOR

0.990000

MAX. D-SPACING

2.000000

GEOMETRY COR.

YES

O.K.

EXIT

OUTPUT

TIFF 16 BIT

NO

#OUT

0.0

65535.00

EXIT

MACROS / LOG FILE

%!\ END OF EXPG_IO MACRO FILE*

7-3. *Appendix C. Image Plate Analysis Code*

The following MatLab code was initially developed at APS. It was modified at Caltech and improved for use with the Ti-SiC data. The analysis requires a series of steps as outlined in the text (Section 2). The details of the MatLab data analysis step is shown below. It assumes the data files are prepared by Fit2D (Appendix B).

Each diffraction pattern provided the longitudinal (or axial), transverse, and shear strain in the plane of the composite according to Equation (2-3) which may be written:

For $\omega = 0^o$

$$a^2 \cdot \varepsilon_{11} + 2 \cdot a \cdot b \cdot \varepsilon_{12} + b^2 \cdot \varepsilon_{22} + 2 \cdot a \cdot c \cdot \varepsilon_{13} + 2 \cdot b \cdot c \cdot \varepsilon_{23} + c^2 \cdot \varepsilon_{33} = \ln\left(\frac{\sin(\theta_0)}{\sin(\theta)}\right)$$

For $\omega = 90^o$ (1)

$$c^2 \cdot \varepsilon_{11} - 2 \cdot b \cdot c \cdot \varepsilon_{12} + b^2 \cdot \varepsilon_{22} - 2 \cdot a \cdot c \cdot \varepsilon_{13} + 2 \cdot b \cdot a \cdot \varepsilon_{23} + a^2 \cdot \varepsilon_{33} = \ln\left(\frac{\sin(\theta_0)}{\sin(\theta)}\right)$$

where $a = \sin\theta$, $b = -\cos\eta \cos\theta$, $c = -\sin\eta \cos\theta$, and $\ln(\sin\theta_0 / \sin\theta)$ represents the diffraction cone distortion for a particular (2θ, η) position. Normally, at least two orientations of the sample, such as $\omega = 0^o$ and $\omega = 90^o$ (Figure 2-3), must be exposed to solve for the three-dimensional strain tensor in a specimen. Here entire rings were collected in one exposure providing sufficient information for examining two dimensions of the strain state in the composite, specifically the strain within the plane of the fibers. Strain out of the composite plane is integrated by the X rays which were aligned perpendicular to that plane. To solve Eqn. (1), a fictitious rotation in ω was used for the second orientation. The solution for ε_{33} under this fictitious 90^o rotation is by definition

identical to the strain for ε_{11} with $\omega = 0^o$. Since both directions are identical, the solution for both strains was averaged and reported as the axial strain. The following MatLab code was written which is capable of performing a least square fit of this strain equation to the diffraction rings. Half of the ring was assigned $\omega = 0^o$, the other half was assigned $\omega = 90^o$. The diffraction rings were fit using a pseudo-voigt peak profile in 2θ over 120 azimuthal divisions of η. MatLab also facilitated automation of the strain analysis for examination of a large array of positions around the damage zone in the composite.

Step 1, Call File 1 (an "azmacro.m" file):

This file automates the fitting process for the tiff files. Data files can be loaded with a root name followed by a number with up to three leading zeros. Once loaded, the files are sent to the fitting routine. Initial peak positions are determined based on the crystal structure and the lattice parameters for the phase(s) of interest. Fits to the peaks are performed with a pseudo-voigt peak profile.

```
%  load a series of tiff files, fit with PV, and output as structures (*.mat files)
%  Modified from original version by J. Almer, APS, January 2002
ff=0; global FILENAME,ff;
for kk=7362:1:7383
  FILENAME=['filename_',num2str(kk),'.tif'];
  ff=ff+1; azfit_Si_Ti_SiC;
end
clear kk ff;
```

File called by above file in Step 1 (an "azfit.m" file):

```
% Fits selected peaks as a function of azimuth.  Input is the tiff file FILENAME (must be
in memory).
% Notes:
% 1. cen0 values are starting guesses for radial peak positions.
% 2. Fits to pseudo-voight functions.
% 3. Fits up to 4 Si, 4 Ti and 4 SiC peaks.


if ~exist('im')
   im = 2^16 - double(imread(FILENAME)); end


distance=1115.5; energy=65.35; pixsize=0.1; a1=5.4308; a2=2.93025; c2=4.67857;
a3=4.365;% respective units of mm,keV,mm,Angstrom,A,A,A
h=[1 1 1 1 2 2 1 3 2 1 4 3];
k=[1 0 1 0 0 2 0 1 2 1 0 1];
l=[1 0 1 1 0 0 2 1 0 0 0 1];
for i=[1 6 8 11];
cen0(i)=round(cen0calc('cubic',h(i),k(i),l(i),a1,a1,a1,distance,energy,pixsize)); end; %Si
peaks
for i=[2 4 7 10];
cen0(i)=round(cen0calc('hexag',h(i),k(i),l(i),a2,a2,c2,distance,energy,pixsize)); end; %a-
Ti peaks
```

```
for i=[3 5 9 12];
cen0(i)=round(cen0calc('cubic',h(i),k(i),l(i),a3,a3,a3,distance,energy,pixsize)); end;
%SiC peaks
nPeak = length(cen0);
nAzi = size(im); nAzi = nAzi(1);


disp([sprintf('FILENAME is %s',FILENAME)])
% fit selected single peaks to PV, and output to fit structure for each azimuth
opt = optimset('disp','off','lev','on','large','on','jacobi','on','tolx',1e-3,'tolf',1e-
3,'maxi',400);
dx = 20; fn = {'backg1' 'psv1'}; npar = [2 4];% dx = width of peak search
low = [-inf 0 0 0 0 0];  up = [inf inf inf inf inf 1];
for azi = nAzi:-1:1
   if rem(azi, 20) == 0; fprintf('%5i',azi); end
    for peak = [1 4 6 7 8 9 10 11]; % Single peaks to fit
      x = cen0(peak) - dx: cen0(peak) + dx;
      y = im(azi, x);
      ymax = max(max(y)); xmax = x(find(y==ymax)); xmax = xmax(1); ymin =
min(min(y));
      fwhmguess = 4; slguess=(y(find(x==cen0(peak)+dx))-y(find(x==cen0(peak)-
dx)))/dx/2;
      p0 = [slguess, ymin, 5*(ymax-ymin), cen0(peak), fwhmguess, .5];
      y0 = sumfun1(p0,[],npar,fn,x);
```

```
    [pfit,rn,rs,ex,out,lam,jac] =
lsqnonlin('sumfun1',p0,low,up,opt,[],npar,fn,x,y,ones(size(y)));
    [dum var] = confint(pfit,rs,jac); % variance of fitted params
    yfit = sumfun1(pfit,[],npar,fn,x);
   %  figure(1); plot(x,y,'+',x,yfit,'-b',x,y0,'-r'); xlabel('Radial position');
%uncomment/alter to plot fit and data
   %   ylabel('Intensity'); text(0.2,0.95,sprintf('Peak  %i and azimuth %i',peak,azi),'sc');
pause;  %uncomment/alter to plot fit and data
    fit(1,peak).peak(azi,1) = pfit(3);fit(1,peak).cen(azi,1) = pfit(4);
fit(1,peak).fwhm(azi,1) = pfit(5);
    fit(1,peak).shape(azi,1) = pfit(6);fit(1,peak).dpeak(azi,1) = sqrt(var(3));
    fit(1,peak).dcen(azi,1) = sqrt(var(4));fit(1,peak).dfwhm(azi,1) = sqrt(var(5));
   end
end

save (FILENAME(1:findstr(FILENAME,'.')-1), 'fit');
clear im;
```

Step 2, Call File 2 (a "strain_macro.m" file):

This file performs the strain analysis step in the procedure. Since it is only dealing with the array of points defined by the previous step, this step completes quickly. The analysis is based on the equations from [50].

```
%  load a series of mat files, which calls strain_Si_Ti_SiC
ff=0; global FILENAME,ff;
for kk=1:1:7383
  FILENAME=['filename_',num2str(kk, '%03.4g'),'.mat'];
  ff=ff+1; strain_Si_Ti_SiC;
end
clear kk ff;
```

File called by above file in Step 2 (a "strain.m" file):

```
% Converts measured radial positions to strain and stress.  Equations from He and Smith.
    distance=1115.5; energy=65.35; pixsize=0.1; a1=5.4308; a2=2.93025;
c2=4.67857; a3=4.362;% respective units of mm,keV,mm,Angstrom,A,A,A
    h=[1 1 1 1 2 2 1 3 2 1 4 3];
    k=[1 0 1 0 0 2 0 1 2 1 0 1];
    l=[1 0 1 1 0 0 2 1 0 0 0 1];
    for i=[1 6 8 11];
cen0(i)=round(cen0calc('cubic',h(i),k(i),l(i),a1,a1,a1,distance,energy,pixsize)); end; %Si peaks
    for i=[2 4 7 10];
cen0(i)=round(cen0calc('hexag',h(i),k(i),l(i),a2,a2,c2,distance,energy,pixsize)); end; %a-Ti peaks
```

for i=[3 5 9 12];

cen0(i)=round(cen0calc('cubic',h(i),k(i),l(i),a3,a3,a3,distance,energy,pixsize)); end;

*%*SiC peaks

nPeaks=length(cen0);% number of peaks measured

PeakInfo={'Si111' 'Ti100' 'SiC111' 'Ti101' 'SiC200' 'Si220' 'Ti102' 'Si311' 'SiC220' 'Ti110' 'Si400' 'SiC311'}; % identity of the peaks fit

%symbol={array(nPeaks)}; % symbols used to identify the peaks

% convert from peak position to strain*;*

*load(FILENAME); %*uncomment if this is done externally (FILENAME must then be global)

N=length(fit(1).cen);azi=(0:360/N:360-360/N)';

disp([sprintf('FILENAME is %s',FILENAME)])

for peak=[1 4 6 7 8 9 10 11];

*chi = (90+(0:360/N:360-360/N))*pi/180; chi = chi';*

*ome = [90*ones(N/2,1);0*ones(N/2,1)]*pi/180; %* here we partition data so that half is from omega0; half from omega90;

% if a single omega used (no rotation), a biaxial strain state is assumed and component11=ave(11,33).

*th = atan(mean(fit(1,peak).cen)*pixsize/distance)/2; th = th*ones(N,1);*

*phi = 0*pi/180*ones(N,1);*

*psi = 0*pi/180*ones(N,1);*

dR = (fit(1,peak).cen - cen0(1,peak))/cen0(1,peak);

sigdR = 5(fit(1,peak).dcen)/cen0(1,peak);*

[a,siga, chisq, gof, cov, A] = hesvd(dR,sigdR,chi,th,phi,psi,ome);

[temp,dR1] = he(a',chi,th,phi,psi,ome);

*figure(2); plot(azi,-dR,'+',azi,dR1,'-r'); xlabel('Azimuth'); %*uncomment/alter to plot fit and data

*ylabel('Strain'); text(0.1,0.95,sprintf('Biaxial strains (x10^-^3) fit to peak #%i which is %s',peak,PeakInfo{peak}),'sc'); %*uncomment/alter to plot fit and data

*text(0.1,0.9,sprintf('e11= %5f, e22= %5f, e33= %5f',1000*a(1),1000*a(3),1000*a(6)),'sc'); %*uncomment/alter to plot fit and data

*text(0.12,0.85,sprintf('e12= %5f, ave(11,33)= %5f, diff(11,33)= %5f',1000*a(2),1000*(a(1)+a(6))/2,1000*(a(1)-a(6))),'sc');%*uncomment/alter to plot fit and data

pause;

fit(1,peak).strain(1,1)=a(1);fit(1,peak).strain(1,2)=a(2);fit(1,peak).strain(1,3)=a(3);

fit(1,peak).strain(1,4)=a(4);fit(1,peak).strain(1,5)=a(5);fit(1,peak).strain(1,6)=a(6);

fit(1,peak).dstrain(1,1)=siga(1);fit(1,peak).dstrain(1,2)=siga(2);fit(1,peak).dstrain(1,3)= siga(3);

fit(1,peak).dstrain(1,4)=siga(4);fit(1,peak).dstrain(1,5)=siga(5);fit(1,peak).dstrain(1,6)= siga(6);

```
 fit(1,peak).gof(1,1)=gof; fit(1,peak).chisq(1,1)=chisq;
 end
```

*save (FILENAME(1:findstr(FILENAME,'.')-1), 'fit'); %*this updates the fit structure, to include strain/stress information

Step 3, Call file 3 ("ascii_macro.m" file):

To prepare the resulting strains for plotting and further analysis this last step extracts the values of interest from the *.mat file into an ascii file. Specifically, it opens a series of mat files (incremented by value kk) and prints out selected data in ascii format, to the outputfilename.txt file.

```
ff=0; global FILENAME,ff;
 fileout=fopen('outputfilename.txt','w');
  fprintf(fileout,'File Peak e11 sig(e11) e12 sig(e12) e22 sig(e22) chisq \n'); %labels are fixed here. e11 is average of e11 and e33 from .mat file.
for kk=1:1:7383
 %if kk==5%|5045|5150|5183  %Uncomment for useful method to skip bad files
  %  disp([sprintf('bad FILENAME')]);
   % elseif kk==3
  % disp([sprintf('bad FILENAME')]);
 %elseif kk==5150
%    disp([sprintf('bad FILENAME')]);
```

```
%elseif kk==5183
%     disp([sprintf('bad FILENAME')]);
%    elseif kk==5197
%     disp([sprintf('bad FILENAME')]);
%else
    FILENAME=['filename_',num2str(kk, '%03.4g'),'.mat'];
    ff=ff+1;
    for peak=[9];

     fprintf(fileout,'%i %i %f %f %f %f %f %f %f
\n',kk,peak,(fit(1,peak).strain(1,1)+fit(1,peak).strain(1,6))/2,...

(fit(1,peak).dstrain(1,1)+fit(1,peak).dstrain(1,6))/2,fit(1,peak).strain(1,2),fit(1,peak).dstra
in(1,2),...
       fit(1,peak).strain(1,3),fit(1,peak).dstrain(1,3),fit(1,peak).chisq);
    end
    disp([sprintf('FILENAME is %s',FILENAME)])
    load(FILENAME);

end
fclose(fileout);
clear kk ff;
```

References

1. Daniel, I. M., Ishai, O., *Engineering Mechanics of Composite Materials*. Oxford University Press, Inc. New York, NY,1994; 4.
2. Suresh, S., Mortensen, A., Needleman, A., *Fundamentals of Metal-Matrix Composites*. Butterworth-Heinemann, Stoneham, MA, 1993; 307, 313.
3. Bader, M. G., Clyne, T. W., Cappleman, G. R., Hubert, P. A., "The Fabrication and Properties of Metal-Matrix Composites Based on Aluminum-Alloy Infiltrated Alumina Fiber Preforms." *Compos. Sci. Tech*., 1985; 23 (4): 287-301.
4. Schueller, R. D., Wawner, F. E., "Effects of Microstructure on Optimum Heat-Treatment Conditions in Metal Matrix Composites." *J. Mat. Sci.,* 1991; 26 (12): 3287-3291.
5. Schueller, R. D., Wawner, F. E., "An Analysis of High-Temperature Behavior of AA2124/SiC Whisker Composites." *Compos. Sci. Tech.*, 1991; 40 (2): 213-223.
6. He, J., Beyerlein, I. J., Clarke, D. R., "Load Transfer From Broken Fibers in Continuous Fiber Al2O3-A1 Composites and Dependence on Local Volume Fraction." *J. Mech. Phys. Solids*, 1999; 47 (3): 465-502.
7. *ASTM Standards and Leterature References for Composite Materials*, 2nd Ed., American Society for Testing and Materials, Philadelphia, PA, 1990.
8. Clyne, T. W., Withers, P. J., *An Introduction to Metal Matrix Composites.* Cambridge University Press, New York, NY, 1993; 234, 241.

9. Ibnabdeljalil, M., Phoenix, S. L. "Creep-Rupture of Brittle-Matrix Composites Reinforced with Time-Dependent Fibers - Scalings and Monte-Carlo Simulations." *J. Mech. Phys. Solids*. 1995; 43(6): 897-931.

10. Beyerlein, I. J., Phoenix, S. L. "Statistics of Fracture for an Elastic Notched Composite Lamina Containing Weibull Fibers .1. Features from Monte-Carlo Simulation." *Eng. Fract. Mech.* 1997; 57(2-3): 241-265.

11. Majumdar, B. S., Matikas, T. E., Miracle, D. B. "Experiments and Analysis of Fiber Fragmentation in Single and Multiple-Fiber Sic/Ti-6al-4v Metal Matrix Composites." *Compos. Pt. B-Eng.* 1998; 29(2): 131-145.

12. Wagner, H. D., Amer, M. S., Schadler, L. S., "Fibre Interactions in Two-Dimensional Composites by Micro-Raman Spectroscopy." *J. Mat. Sci.*, 1996; 31 (5): 1165-1173.

13. Van den Heuvel, P. W. J., Peijs, T., Young, R. J., "Failure phenomena in two-dimensional multi-fibre microcomposites .2. A Raman Spectroscopic Study of the Influence of Inter-Fibre Spacing on Stress Concentrations." *Compos. Sci. Tech.*, 1997; 57 (8): 899-911.

14. Beyerlein, I. J., Amer, M. S., Schadler, L. S., Phoenix, S. L., "New Methodology for Determining In Situ Fiber, Matrix and Interface Stresses in Damaged Multifiber Composites." *Sci. Eng. Compos. Mat.*, 1998; 7 (1-2): 151-204.

15. Schadler, L. S., Amer, M. S., Iskandarani, B., "Experimental Measurement of Fiber/Fiber Interaction Using Micro Raman Spectroscopy." *Mechanics of Materials*, 1996; 23 (3): 205-216.

16. Cullity, B. D., *Elements of X-Ray Diffraction*. 2nd ed. Addison Wesley, Massachusetts, PA, 1978; 130, 464-475.

17. Noyan, I. C., Cohen, J. B., *Residual Stress*. Springer-Verlag, New York, 1987.

18. Moore, M. G.,, Evans, W. P., *Trans. SAE*, **66**, 340 (1958).

19. Rangaswamy, P., Revelos, W. C.,, Jayaraman, N., *Residual Stresses in Composites Measurement, Models and Effects on Thermo-Mechanical Behavior*. Ed. Barrera, E. V., and Dutta, I., The Minerals, Metals & Materials Sciety, 1993; 227.

20. Dragoi, D., Ustundag, E., Clausen, B., Bourke, M. A. M. "Investigation of Thermal Residual Stresses in Tungsten- Fiber/Bulk Metallic Glass Matrix Composites." *Scr. Mater.* 2001; 45(2): 245-252.

21. Choo, H., Rangaswamy, P., Bourke, M. A. M., Larsen, J. M. "Thermal Expansion Anisotropy in a Ti-6al-4v/Sic Composite." *Mater. Sci. Eng. A-Struct. Mater. Prop. Microstruct. Process.* 2002; 325(1-2): 236-241.

22. Carter, D. H., Bourke, M. A. M. "Neutron Diffraction Study of the Deformation Behavior of Beryllium-Aluminum Composites." *Acta Mater.* 2000; 48(11): 2885-2900.

23. Rangaswamy, P., Daymond, M. R., Bourke, M. A. M., Von Dreele, R., Bennett, K., Jayaraman, N. "Texture and Residual Strain in Two Sic/Ti-6-2-4-2 Titanium Composites." *Metall. Mater. Trans. A-Phys. Metall. Mater. Sci.* 2000; 31(3A): 889-898.

24. Choo, H., Rangaswamy, P., Bourke, M. A. M. "Internal Strain Evolution During Heating of Ti-6al-4v/Scs-6 Composite." *Scr. Mater.* 1999; 42(2): 175-181.

25. Warrier, S. G., Rangaswamy, P., Bourke, M. A. M., Krishnamurthy, S. "Assessment of the Fiber/Matrix Interface Bond Strength in Sic/Ti-6al-4v Composites." *Mater. Sci. Eng. A-Struct. Mater. Prop. Microstruct. Process.* 1999; 259(2): 220-227.

26. Rangaswamy, P., Bourke, M. A. M., Wright, P. K., Jayaraman, N., Kartzmark, E., Roberts, J. A. "The Influence of Thermal-Mechanical Processing on Residual Stresses in Titanium Matrix Composites." *Mater. Sci. Eng. A-Struct. Mater. Prop. Microstruct. Process.* 1997; 224(1-2): 200-209.

27. Allen, A. J., Bourke, M. A. M., Dawes, S., Hutchings, M. T., Withers, P. J. "The Analysis of Internal Strains Measured by Neutron- Diffraction in Al-Sic Metal Matrix Composites." *Acta Metall. Mater.* 1992; 40(9): 2361-2373.

28. Hanan, J. C., Ustundag, E., Clausen, B., Sivasambu, M., Beyerlein, I. J., Brown, D. W., Bourke, M. A. M. "Residual Strain Evolution During the Deformation of Single Fiber Metal Matrix Composites." *Materials Science Forum*. 2002; 404-4: 907-911.

29. Hanan, J. C., Üstündag, E., Beyerlein, I. J., Swift, G. A., Clausen, B., Brown, D. W., Bourke, M. A. M., *Adv. X-Ray Anal*. 2002; 45.

30. Hanan, J. C., Mahesh, S., Üstündag, E., Beyerlein, I. J., *et al.* *In progress* 2002.

31. Hanan, J. C., Aydiner, C. C., Ustundag, E., Swift, G. A., Kaldor, S. K., Noyan, I. C. "Characterization of Fiber/Matrix Interfaces Using X-Ray Microtopography." *Materials Science Forum*. 2002; 404-4: 919-923.

32. Hanan, J. C., Tamura, N., Swift, G. A., Üstündag, E., *In progress* 2002.

33. Chawla, K. K., *Composite Materials Science and Engineering*. 2nd ed. Springer-Verlag, New York, NY, 1998; 167.

34. Beyerlein, I. J., Landis, C. M., "Shear-Lag Model For Failure Simulations of Unidirectional Fiber Composites Including Matrix Stiffness." *Mechanics of Materials*, 1999; 31 (5): 331-350.

35. Lester, H. H., Aborn, R. M., *Army Ordnance* **6**, 120 (1925-26).

36. I. C. Noyan, J. Jordan-Sweet, E. G. Liniger, S. K. Kaldor, "Characterization of Substrate/Thin-Film Interfaces with X-ray Microdiffraction," *Appl. Phys. Lett.*, **72** (25), 3338 (1998).

37. Noyan, I. C., Wang, P. C., Kaldor, S. K., Jordan-Sweet, J. L., Liniger, E. G. "Divergence Effects in Monochromatic X-Ray Microdiffraction Using Tapered Capillary Optics." *Rev. Sci. Instrum.* 2000; 71(5): 1991-2000.

38. Noyan, I. C., Kaldor, S. K., Wang, P. C., Jordan-Sweet, J. "A Cost-Effective Method for Minimizing the Sphere-of-Confusion Error of X-Ray Microdiffractometers." *Rev. Sci. Instrum.* 1999; 70(2): 1300-1304.

39. Poulsen, H. F., Lorentzen, T., Feidenhansl, R., Liu, Y. L. "A Synchrotron X-Ray Diffraction Study of the Local Residual Strains around a Single Inclusion in an Al/W Metal-Matrix Composite." *Metall. Mater. Trans. A-Phys. Metall. Mater. Sci.* 1997; 28(1): 237-243.

40. Kuntz, T. A., Wadley, H. N. G., Black, D. R. "Residual Strain Gradient Determination in Metal-Matrix Composites by Synchrotron X-Ray-Energy Dispersive Diffraction." *Metallurgical Transactions a-Physical Metallurgy and Materials Science*. 1993; 24(5): 1117-1124.

41. Poulsen, H. F., Garbe, S., Lorentzen, T., Jensen, D. J., Poulsen, F. W., Andersen, N. H., Frello, T., Feidenhansl, R., Graafsma, H. "Applications of High-Energy Synchrotron Radiation for Structural Studies of Polycrystalline Materials." *J. Synchrot. Radiat.* 1997; 4: 147-154.

42. Korsunsky, A. M., Wells, K. E., Withers, P. J., "Mapping Two-Dimensional State of Strain Using Synchroton X-ray Diffraction." *Scripta Mater*., 1998; 39 (12): 1705-1712.

43. Daymond, M. R., Withers, P. J., "A Synchrotron Radiation Study of Transient Internal Strain Changes During the Early Stages of Thermal Cycling in an Al/SiCW MMC." *Scripta Mater*., 1996; 35 (10): 1229-1234.

44. Noyan, I. C., Schadler, L. S., "Characterization of Inhomogeneous Elastic-Deformation with X-Ray Diffraction." *Metall. Mater. Trans. A*, 1994; 25A: 341-347.

45. Wanner, A., Dunand, D., "Synchrotron X-ray Study of Bulk Lattice Strains in Externally Loaded Cu-Mo Composites." *Metall. Mater. Trans. A*, 2000; 31A: 2949-2962.

46. Warren, B. E., *X-Ray Diffraction*. Addison-Wesley Publishing Company, Inc., Reading, MA, 1969.

47. Almer, J., Lienert, U., *Unpublisted document* for the Neutron / Synchrotron Summer School, Argonne National Laboratory, August 2001.

48. von Seggern, H., Voigt, T., Knüpfer, W., Lange, G. "Physical Model of Photostimulated Luminescence of X-Ray-Irradiated BaFBr-Eu2^{+}." *J., Appl. Phys.*, 1988; 64 (3): 1405–1412.

49. Amemiya, Y., *J. Synchrotron Rad.*, "Imaging Plates for use with Synchrotron-Radiation." 1995; 2: 13–21.

50. He, B. B., Smith, K. L., Preckwinkel, U., Schultz, W., "Micro-Area Residual Stress Measurement Using a Two-Dimensional Detector." *Mat. Sci. Forum*, 2000; 347-349: 101-106.

51. He, B. B., Smith, K. L., *Proceedings of the SEM Spring Conference on Experimental and Applied Mechanics*, Houston, TX, 1998; 217.

52. Hammersley, A. P. *ESRF Internal Report*, **EXP/AH/95-01**, FIT2D V5.18 Reference Manual V1.6, (1995).

53. Vogel, S., *Diplomarbeit*, Christian-Albrechts-Universität zu Kiel, (2001).

54. Rangaswamy, P., Prime, M. B., Daymond, M. R., Bourke, M. A. M., Clausen, B., Choo, H., Jayaraman, N., "Comparison of Residual Strains Measured by X-Ray and Neutron Diffraction in a Titanium (Ti-6Al-4V) Matrix Composite." *Mater. Sci. Eng*., 1999; A259 (2): 209-219.

55. Withers, P. J., Clarke, A. P., "A Neutron Diffraction Study of Load Partitioning in Continuous Ti/SiC Composites." *Acta Mater*., 1998; 46 (18): 6585-6598.

56. Gundel, D. B., Wawner, F. E., "Experimental and Theoretical Assessment of the Longitudinal Tensile Strength of Unidirectional SiC-Fiber/Titanium-Matrix Composites." *Comp. Sci. Tech*., 1997; 57 (4): 471-481.

57. Hanan, J. C., Üstündag, E., Dragoi, D., Noyan, I. C., Haeffner, D. R., Lee, P. L., *Adv. X-Ray Anal*., 2000; 44.

58. Harlow, D. G., Phoenix, S. L., "Chain-of-Bundles Probability Model for Strength of Fibrous Materials .1. Analysis and Conjectures." *J. Comp. Mat.* 1978a; 12: 195-214.

59. Harlow, D. G., Phoenix, S. L., "Chain-of-Bundles Probability Model for Strength of Fibrous Materials .2. Numerical Study of Convergence." *J. Comp. Mat.* 1978b; 12 (Jul): 314-334.

60. Curtin, W. A., "Theory of Mechanical-Properties Of Ceramic-Matrix Composites." *J. Am. Ceram. Soc.*, 1991a; 74 (11): 2837-2845.

61. Curtin, W. A., "Exact Theory of Fiber Fragmentation in a Single-Filament Composite." *J. Mater. Sci.*, 1991b; 26 (19): 5239-5253.

62. Ahn, B. K., Curtin, W. A., "Strain and Hysteresis by Stochastic Matrix Cracking in Ceramic Matrix Composites." *J. Mech. Phys. Solids*, 1997; 45 (2): 177-209.

63. Hui, C-Y., Phoenix, S. L., Ibnabdeljalil, M., "An Exact Closed-Form Solution for Fragmentation of Weibull Fibers in a Single Filament Composite with Applications to Fiber-Reinforced Ceramics." *J. Mech. Phys. Solids,* 1995; 43 (10): 1551-1585.

64. Hedgepeth, J. M., NASA TN D-822 (1961).

65. Fukuda, H., Kawata, K., "On the Stress Concentration Factor in Fiberous Composites." *Fiber Sci. Tech.*, 1976; 9: 189-203.

66. Rossettos, J. N., Shishesaz, M., "Stress-Concentration in Fiber Composite Sheets Including Matrix Extension." *J. Appl. Mech.*, 1987; 54 (3): 723-724.

67. Zeng, Q. D., Wang, Z. L.,, Ling, L., "A Study of the Influence of Interfacial Damage on Stress Concentrations in Unidirectional Composites." *J. Compos. Mater.*, 1997; 57 (1): 129-135.

68. Reedy, E. D., "Analysis of Cheter-Notched Monolayers with Application to Boron-Aluminum Composites." *J. Mech. Phys. Solids*, 1980; 28 (5-6): 265-286.

69. Choo, H., Rangaswamy, P., Bourke, M. A. M., "Internal Strain Evolution During Heating of Ti-6Al-4V/SCS-6 Composite." *Scripta Materialia*, 2000; 42(2): 175-181.

70. Nimmer, R., Bankert, R., Russel, E., Smith, G., Wright, P., "Micromechanical Modeling of Fiber Matrix Interface Effects in Transversely Loaded SiC Ti-6-4 Metal Matrix Composites." *J. Comp. Technol. Res.*, 1991; 13(1): 3-13.

71. Durodola, J., Derby, B., "An Analysis of Thermal Residual-Stresses in Ti-6-4 Alloy Reinforced with SiC and Al2O3 Fibers." *Acta Metall. Mater.*, 1994; 42: 1525-1534.

72. Pickard, S. M., Miracle, D. B., "An Experimental Study of Residual Stresses in SiC-Fiber-Reinforced Ti-Based Composites." *Mater. Sci. Eng.*, 1995; A203: 59-68.

73. Deve, H., Metal-Matrix Composites Division, 3M Corp., St. Paul, MN, personal communication (2000).

74. Dicarlo, J. A., "Creep of Chemically Vapor-Deposited SiC Fibers." *J. Mater. Sci.* 1986; 21: 217-224.

75. Wycoffe, R. W. G., *Crystal Structures*. 3rd ed. New York: Wiley Interscience, Vol. 1 1964, p. 113.

76. Rietveld, H. M., *J.* "A Profile Refinement Method for Nuclear and Magnetic Structures." *Appl. Cryst.*, 1969; 2: 65.

77. Larson, A. C., Von Dreele, R. B., GSAS-General Structure Analysis System, LAUR 86-748, Los Alamos National Laboratory, (1986).

78. Nutt, S. R. and Wawner, F. E., "Silicon-Carbide Filaments - Microstructure." *J. Mater. Sci.*, 1985; 20 (6): 1953-1960.

79. Gisen, F., Glocker, R., and Osswald, E., *Z. Tech. Physik*, 1936; 17: 145.

80. Hanan, J. C., Beyerlein, I. J., Üstündag, E., Swift, G. A., Clausen, B., Brown, D. W. Bourke, M. A. M., *Adv. in Fracture Research ICF* **10***,* Elsevier, UK (2001).

81. Maire, E., Owen, A., Buffiere, J.-Y., Withers, P. J., "A Synchrotron X-Ray Study of a Ti/SiCf Composite During In Situ Straining." *Acta Mater.* 2001; 49(1): 153-163.

82. Callister, W. D. Jr., *Materials Science and Engineering, An Introduction*, 3rd Ed., John Wiley and Sons, Inc.: New York, 1994: 84.

83. ASTM: E112-88, *Standard Test Methods for Determining Grain Sizes*, 297-322.

84. Hubbell, J. H., Int. J. *Appl. Radiat. Isot.*, "Photon Mass Attenuation and Energy-Absorption Coefficients from 1 keV to 20 MeV." 1982; 33 (11): 1269-1290.

85 . Hanan, J. H., Clausen, B., Swift, G. A., Üstündag, E., *et al*., "Microscale Residual Strains in Monolayer Unidirectional Fiber Composites." *Mater. Sci. Forum,* 2002; 404-407: 913-918.

86. Bonda, N. R., Noyan, I. C., "Deformation Inhomogeneity and Representative Volume in Pb/Sn Solder Alloys." *Met. Trans*. *A*, 1992; 23(2): 479-484.

87. Clausen, B., Lorentzen, T., Leffers, T., "Self-Consistent Modelling of the Plastic Deformation of FCC Polycrystals and its Implications for Diffraction Measurements of Internal Stresses." *Acta Mater.*, 1998; 46(9): 3087-3098.

88. Clausen, B., Lorentzen, T., Bourke, M. A. M., Daymond, M. R., "Lattice Strain Evolution During Uniaxial Tensile Loading of Stainless Steel." *Mat. Sci. & Eng. A*, 1999; 259(1): 17-24.

89. Hanan, J. C., Tamura, N., Swift, G. A., Üstündag, E., *ALS Report.* (2002)